UNIVERSITY OF COPENHAGEN
FACULTY OF SCIENCE

NIELS BOHR INSTITUTE

NONLINEAR PHENOMENA IN DISSIPATION-DILUTED NANOMECHANICAL RESONATORS

PHD THESIS

LETIZIA CATALINI

This thesis has been submitted to the
PhD school of Science at the University of Copenhagen

2022

ABSTRACT

Over the last forty years, nanomechanical resonators have gained a central role in widespread fields in science and technology. More recently, the invention of techniques like dissipation dilution and soft clamping led to the fabrication of nanomechanical resonators, in particular strings and membranes, with higher and higher quality factors. The corresponding long coherence time together with the low effective mass and the high resonance frequency place these systems at the forefront in force sensing applications. Moreover, the possibility of interfacing these resonators with disparate systems such as electromagnetic cavities, spin ensembles, atoms and superconducting qubits, makes them promising building blocks for the next generation of quantum technologies.

In this thesis, we focus our attention on several nonlinear phenomena arising in dissipation-diluted nanomechanical resonators. The high quality factor featured by soft-clamped membranes allows us to enter the regime of large displacement amplitude for the out-of-plane modes, in which a linear description of the motion fails. In this regime, we observe both conservative and dissipative nonlinearities, which manifest respectively as Duffing frequency shift and amplitude-dependent damping. We model these nonlinearities as geometric, and we derive formal expressions to predict them starting from a continuum elastic theory. We test our model by comparing the predicted nonlinear parameters with the measured ones on a vast selection of geometries of both single and double defect membranes. By further extending this model, we predict that the in-plane modes of the membrane couple to the out-of-plane ones. This coupling modulates the resonance frequency of the out-of-plane modes, thus realizing a parametric modulation. We perform preliminary experimental investigations of this phenomenon.

The theoretical and experimental results in this thesis add new evidences which can shed light on the geometric origin of nonlinear phenomena in dissipation-diluted membrane resonators. Understanding and controlling these nonlinearities is important for several applications. In force sensing experiments, for instance, one needs to reduce nonlinearities, which may otherwise limit the lowest achievable sensitivity. In contrast, quantum experiments trying to access genuine nonclassical features of motion will benefit from enhancing nonlinearities. Our model, which proved successful to describe nonlinearities in disparate membrane geometries, will be an asset to engineer new nanomechanical resonators with controlled strengths of nonlinearity for the above-mentioned applications.

SAMMENFATNING

I løbet af de sidste fyrre år har nanomekaniske resonatorer opnået en central rolle i vidt forskellige felter indenfor videnskab og teknologi. For nyligt har opfindelsen af teknikker som dissipationsfortyndelse og blød hæftning ledt til fabrikationen af nanomekaniske resonatorer, især strenge og membraner, med højere og højere kvalitetsfaktorer. De tilsvarende lange kohærenstider sammen den lave effektive masse og høje resonansfrekvens placerer disse systemer forrest indenfor kraft-sensor anvendelser. Ydermere gør muligheden for at integrere disse resonatorer med vidt forskellige systemer såsom elektromagnetiske kaviteter, spin ensembler, atomer og superledende qubits, dem til lovende byggeklodser for den næste generation af kvanteteknologier.

I denne afhandling retter vi vores opmærksomhed imod flere ikkelineære fænomener der opstår i dissipationsfortyndede nanomekaniske resonatorer. Den høje kvalitetsfaktor fremvist af blødt hæftede membraner lader os tilgå regimet af stor forskydningsamplitude for ude-af-planet resonanser, hvor en lineær beskrivelse af bevægelsen slår fejl. I dette regime observerer vi både konservative og dissipative ikkelineariteter, der respektivt optræder som Duffing frekvensskift og amplitudeafhængig dæmpning. Vi modellerer disse ikkelineariteter som geometriske og vi udleder formelle udtryk til at forudsige dem fra en kontinuum elastisk teori. Vi tester vores model ved at sammenligne de forudsagte ikkelineære parametre med de målte på et stort udvalg af geometrier af enkelt- og dobbelt-defekt membraner. Ved yderligere at udvide modellen, forudsiger vi at i-planet resonanser af membraner kobler til ud-af-planet resonanser. Denne kobling modulerer resonansfrekvensen af ud-af-planet resonanser, og realiserer således en parametrisk modulation. Vi udfører indledende eksperimentelle undersøgelser af dette fænomen.

De teoretiske og eksperimentelle resultater in denne afhandling tilføjer nye beviser der kan kaste lys over den geometriske oprindelse af ikkelineære fænomener i dissipationsfortyndede membranresonatorer. Forståelse af og kontrol over disse ikkelineariteter er vigtigt for flere anvendelser. I kraft-sensor eksperimenter, for eksempel, skal man reducere ikkelineariteter, der ellers kan begrænse den højest opnåelige sensitivitet. I modsætning, vil kvanteeksperimenter der forsøger at tilgå ægte uklassiske egenskaber ved bevægelse, have gavn af forstærkede ikkelineariteter. Vores model, der har vist sig succesfuld til at beskrive ikkelineariteter i forskellige membrangeometrier, vil være en værdifuld ressource til at designe nye nanomekaniske resonatorer med kontrollerede grader af ikkelinearitet til ovenstående anvendelser.

PUBLICATIONS

[CTS20] Letizia Catalini, Yeghishe Tsaturyan,Albert Schliesser, *Soft-Clamped Phononic Dimers for Mechanical Sensing and Transduction*, Phys. Rev. Appl., **14**, 1 (2020)

[Cat+21] Letizia Catalini, Massimiliano Rossi, Eric C. Langman, Albert Schliesser, *Modeling and Observation of Nonlinear Damping in Dissipation-Diluted Nanomechanical Resonators*, Phys. Rev. Lett., **126**, 17 (2021)

[H¨+21b] David Hälg, Thomas Gisler, Yeghishe Tsaturyan, Letizia Catalini, Urs Grob, Marc-Dominik Krass, Martin Héritier, Hinrich Mattiat, Ann-Katrin Thamm, Romana Schirhagl, Eric C. Langman, Albert Schliesser, Christian L. Degen, Alexander Eichler, *Membrane-Based Scanning Force Microscopy*, Phys. Rev. App., **15**, 2 (2021)

CONTENTS

LIST OF FIGURES

LIST OF TABLES

ACRONYMS

FEM	Finite Element Modeling
PSD	Power Spectral Density
UHV	Ultra High Vacuum
BS	Beam Splitter

PBS Polarizing Beam Splitter

PB Probe Beam

LO Local Oscillator

PM Polarization Maintaining

AOM Acousto-Optic Modulator

HF2LI HF2 Lock-In Amplifier

PID Proportional-Integral-Derivative Controller

FFT Discrete Fourier Transform

FPGA Field Programmable Gate Array

MRFM Magnetic Resonance Force Microscopy

TMV Tobacco Mosaic Virus

INTRODUCTION

The harmonic oscillator is perhaps the simplest and yet the most ubiquitous model in physics. Despite its simplicity, it is able to describe the behavior of a huge variety of systems of all sizes. The equations describing the motion of a mass attached on a spring are the same that describe the wiggle of electrons in nuclear orbits, the electric current some electronic circuits, the swing of a pendulum, the vibration of drums or strings in musical instruments, but also mechanical vibrations of a bridge. A particularly important application of the harmonic oscillator description is modeling systems with one or more dimensions below a micrometer, a lengthscale especially important for the field of nanoscience.

Since the breakthrough of the scanning tunneling microscopy (STM) in 1981 and of the atom force microscopy (AFM) only few years later, nanomechanical objects attracted significant interest in science and technology. Characterized by an effective mass ranging from picogram to nanogram and a quality factor ranging from few thousands to few millions, nanomechanical resonators have been used to sense different physical quantities such as force [Rei+16], mass [Cha+12], radiation [Yi+13; Pil+21] and temperature [Sad+20]. Simultaneously, the recent technological progresses in fabricating these nanomechanical resonators enable to achieve higher and higher quality factor, thus coherence time. This is desirable for quantum technologies, such as microwave-to-optical quantum transducer [MSF18; Bru+21; Sah+21], spin-phonon entanglement [Kar+20] or quantum memories [Wal+20], in which nanomechanical resonators are starting to be employed more frequently.

A milestone for a new generation of resonators was the implementation of the dissipation dilution technique. Originally introduced by the LIGO collaborations [HS98; Gon00], it consists in introducing a lossless potential to increase the energy stored in the oscillator. In nanomechanical systems, such a lossless potential is given by the presence of a tensile energy [Ver+07; UFPK10; Sch+11; Fed+19]. After the introduction of dissipation dilution, a considerable effort has gone into designing mechanical resonators characterized by lower and lower dissipation. Soft clamping, first introduced in [Tsa+17], is an example of such efforts. This approach consists in fabricating nanomechanical resonators patterned with a phononic crystal structure. A properly engineered defect embedded in this structure can support localized vibrational modes, which are shielded from the environment by the phononic crystal. At the same time, these localized vibrations are greatly suppressed at the clamping region, rendering negligible one of the largest sources of dissipation, the bending losses. The isolation from the environment provided by the phononic crystal and the reduction of bending losses

allow these nanomechanical resonators to have quality factors about hundreds of millions at room temperature for MHz-resonance frequencies. The soft-clamped approach is now widely used in different types of nanomechanical resonators [Gha+18; Ree+19; Ber+21], and it has been complemented with the new ideas of strain engineering [Bec+21b] and structural hierarchy [Bec+21a]. All this led to the fabrication of nanomechanical resonators with quality factors exceeding one billion at room temperature with resonance frequencies which can be tuned from about 100 kHz up to few MHz.

Nanomechanical resonators with such a high quality factors allow one to easily access regimes of motion previously precluded, or hard to reach, in standard room temperature operation. A regime particularly interesting is when the displacement amplitude becomes large and comparable with the smallest resonator dimension, usually its thickness. In this case, the simple description of a nanomechanical resonator as a linear damped harmonic oscillator fails. To properly predict the dynamics in the large displacement regime, we need to account for anharmonic forces arising from the material deformation. The simplest model is the so-called Duffing oscillator [Nay93], which represents a harmonic oscillator with an extra force cubic in the position, the main effect of which is to introduce an amplitude-dependent shift of the resonance frequency. Duffing oscillators are widely studied by the community, as witnessed by the vast literature [AC05; FPT12; Def+12; Hoc+14; Dav+17]. Another signature of the large displacement regime is the appearance of nonlinear viscous forces, which gives rise to the phenomenon of nonlinear damping. In contrast to the Duffing nonlinearity, the nonlinear damping is less studied. It has been observed on a variety of structures [Eic+11; Zai+11; Ant+12; IWM13; Vil+13; Pol+16; CTS20; Cat+21] and some models have been put forward, attributing the source of nonlinear damping to geometric effects [Vil+13; SVR16; Ama18; Gus20; Cat+21] or intermodal coupling [Ata+16]. The dispute about the origin of nonlinear damping has not been resolved, and it remains still an open question as of today.

The large displacement regime affects the dynamics not only of a single mechanical mode, i. e. the one which is strongly driven, but also of other undriven modes via nonlinear coupling with the largely displaced mode. Such cross-nonlinear phenomenon has been observed in systems constituted by coupled harmonic oscillators [KCR09] or within modes with opposite symmetry [Wes+10], and are particularly relevant in dimer resonators [MIC14; CTS20; Ber+21]. The latter system can intuitively be described as two nanomechanical resonators coupled by the common substrate. The tunability of the resulting frequency splitting and the large working area ensured by the presence of two defects make them ideal for force sensing applications. In this scenario, dissipative cross-nonlinear contributions can represent a limiting factor for the force sensitivity [Koš+20].

Dissipation-diluted nanomechanical resonators with high quality factor in the nonlinear regime are also especially suited for parametric driving and amplification experiments. An interesting case is when the mechanical resonance frequency is modulated at twice its value: in this case, the mechanical resonator turns into an amplifier with controllable gain [RG91]. When the resonance frequency modulation equals the mechanical damping rate, the gain diverges and the system becomes unstable. For this reason, high-quality resonators require less modulation strength to reach this threshold. In particular, this parametric driving can be arranged to reduce ('squeeze') the thermal fluctuations of a mechanical quadrature, resulting in a thermomechanical squeezed state. [RG91].

Although the parametric driving has been implemented in experimental settings on nanomechanical resonators through both mechanical [Mah+14; Pat+15; Wu+18] and electrostatic [RG91; H¨21a] actuation, a model which is able to derive the parametric driving from a continuum elastic perspective has not been discussed yet. A deeper understanding of the mechanism behind the parametric modulation in soft-clamped resonators would be beneficial for force sensing experiments, such as magnetic resonance force microscopy experiment (MRFM) where an advanced parametric protocol has been recently proposed to satisfy the particularly demanding requirements for the experimental realization [Koš+20]. Moreover, enhancing the parametric driving finds applications also in quantum experiments, especially in the generation of quantum squeezed states of motion [Wol+15; Pir+15].

The study of dissipation-diluted nanomechanical resonators in the large displacement regime and under parametric driving is at the heart of this research work. We developed both experimental and theoretical tools to measure and quantify but also model and predict the geometric nonlinearities in membrane resonators.

STRUCTURE OF THE THESIS

The thesis is divided in two parts. In the first one, we give an overview of the theory used to model the experimental results presented later in this thesis, as well as the experimental methods employed. In the second part, we present our main results, which consist both of the measurements of nonlinear phenomena as well as of a microscopic model used to explain the data. Most of these results have been published in Ref. [CTS20; Cat+21].

In Chapter 1, we provide a full description of the motion of a thin membrane resonator, starting from a continuum elastic model, then recovering a lumped-element description. In this derivation we introduce the building blocks for all the theoretical work developed during the thesis. We give an overview of the most important sources of dissipation generally affecting our system and we describe the common methods

we use to remove, or at least mitigate, them. In Chapter 2, we give an overview of the interferometric techniques and their application in displacement measurements. Then, we describe the most common noise sources affecting the interferometric measurements and the corresponding optimal working conditions. In Chapter 3, we introduce the experimental setup and techniques used throughout the various measurements.

The successive three chapters form the second part of the thesis. In Chapter 4, we report the observation, quantification, and modeling of Duffing nonlinearity and nonlinear damping in dissipation-diluted nanomechanical resonators. In Chapter 5, we introduce and characterize a new membrane design comprising two defects embedded in the same phononic crystal. We investigate the dynamics of such oscillators in the nonlinear regime using the results of the previous chapters, with emphasis on the cross-nonlinear phenomena. Finally in Chapter 6, we report on the preliminary measurements of parametric effects in soft-clamped membranes. Using the theoretical tools developed so far, we propose a model which predicts the coupling between in-plane and out-of-plane modes as the source of parametric excitation.

Part I

OPTOMECHANICAL SYSTEM

1 MECHANICAL SYSTEM

The harmonic oscillator is one of the fundamental model in physics. It is utilized to model various systems of all sizes. In this first chapter we show how the harmonc oscillator model is able to describe the vibrations of the nanomechanical system studied in this thesis. It consists of a membrane resonator, e. g. a thin plate subjected to a high time-independent in-plane stress. Starting from the fundamental elastostatic concepts, we present a continuum elastic model to describe the deformation of a thin membrane, and we reduce it to a damped harmonic oscillation. Such model constitutes the backbone of the theoretical contents of this research work. Then, we introduce the different types of losses relevant for the system under study, and we describe the two techniques we use to remove or mitigate them. Finally, we give an overview of the membrane designs investigated in this thesis.

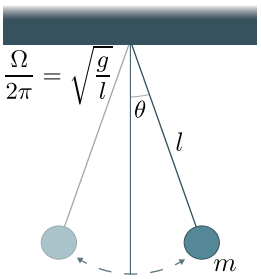

Simple pendulum.

1.1 BASIC ELASTOSTATICS

Every solid body subjected to an external force experiences a transformation. Under particular circumstances this transformation can result in a deformation. Depending on the strength of the force and on the solid body properties, such deformation can be temporary (elastic deformation) or permanent (plastic deformation). Elasticity theory describes the deformation of a solid body and the force applied to (or produced by) the body in the former case. For the purpose of this thesis, we restrain ourselves to the elastic domain. All the contents of this section represent a summary extrapolated from the treatments done in [LL70; Lau11; TK87] and constitute the starting point for the modeling derived in sec. 4.2 and 6.3.

In a continuum object, the position of each point is described by its radius vector $\vec{r}$, which defines its distance from the origin of the coordinate system. By applying an external force, all the points in the medium are displaced. The magnitude of the displacement experienced by each point is described by the *displacement vector*,

$$\vec{d} = \vec{r}\,' - \vec{r}, \tag{1.1}$$

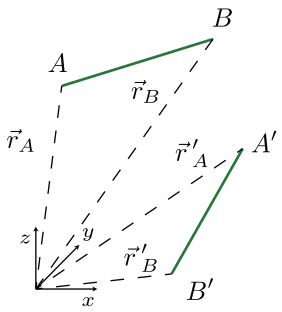

Displaced radius vectors.

where $\vec{r}'$ represents the displaced radius vector. Despite the information contained in the displacement vector, the latter is not the most straightforward quantity to describe a deformation. Although all the points are displaced, not all the displacements result in a deformation. Rotation or translation of a continuum object can displace all the points of body without introducing any type of deformation. We are only interested in the physics describing the reaction of a solid body to a deformation, condition verified every time the distance between two points changes.

To give a complete description of the deformation we need to introduce a tensorial quantity, the so-called *strain tensor* $\overrightarrow{\overrightarrow{\varepsilon}}$, which is expressed in terms of the displacement vector components as [LL70]

$$\varepsilon_{ij} = \frac{1}{2}\left(\partial_j d_i + \partial_i d_j + \partial_i d_k \partial_j d_k\right), \tag{1.2}$$

where the Latin indexes represent the three directions x, y, z and the repeated indexes are summed over. The linear components in Eq. (1.2) represent the deformation associated with the bending of the body ($\varepsilon_{ij}^{\text{bend}}$) while the second order terms represent the stretching or the elongation ($\varepsilon_{ij}^{\text{elong}}$).

An external force deforms the body by changing the distance between the molecules. The molecules react by generating a repulsing/attracting force within the body. We quantify the internal forces through a new tensorial quantity, the *internal stress* $\overrightarrow{\overrightarrow{\sigma}}$ [LL70]. It is expressed as a force per unit area and its magnitude depends on the direction in which the external force acts and on the orientation of the surface upon which the force is acting. Let us called $d\vec{f} = (f_x, f_y, f_z)$ a force per unit volume acting on an arbitrary surface element $d\vec{S} = (dS_x, dS_y, dS_z)$. The external force generates an internal stress which satisfies the so-called Cauchy's stress hypotesis [Lau11]

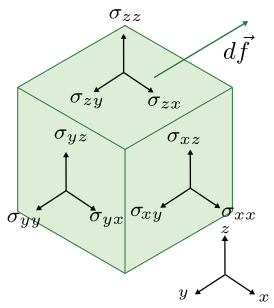

Stress tensor components.

$$df_i = \sigma_{ij} dS_j, \tag{1.3}$$

where the repeated indexes are summed over. In the elastic domain, the relation between the deformation introduced by an external force and the generated internal stress is linear and takes the name of *Hooke's law*. For isotropic material it has the following form [LL70]

$$\sigma_{ij} = \frac{E}{1+\nu}\left(\varepsilon_{ij} + \frac{\nu}{1-2\nu}\varepsilon_{kk}\delta_{ij}\right), \tag{1.4}$$

where E and ν are the Young modulus and the Poisson's ratio, respectively, and δ_{ij} is the Kronecker delta. E and ν are material properties. For Si_3N_4 resonators $E = 270\,\text{GPa}$ and $\nu = 0.27$.

In the majority of the cases, we are interested only in small deformations which can be fully described only by the first order terms in Eq. (1.2), hence we usually consider a strain tensor written as

$$\varepsilon_{ij} = \frac{1}{2}\left(\partial_j d_i + \partial_i d_j\right). \tag{1.5}$$

Eq. (1.5) is also called *Cauchy's strain tensor* [Lau11]. In this thesis we always refer to Eq. (1.5) as *strain tensor* and we use its definition unless specified otherwise.

1.2 LINEAR MEMBRANE RESONATOR

Once defined the basic equations to derive the fundamental tensorial quantities $\overrightarrow{\overrightarrow{\sigma}}$ and $\overrightarrow{\overrightarrow{\varepsilon}}$, we derive the equation of motion of an oscillating object. Let us consider a thin square membrane, i. e. a square plate of side L subjected to a time-independent in-plane stress, called *tensile stress* (σ_0). The reference frame is defined in Fig. 1.1.

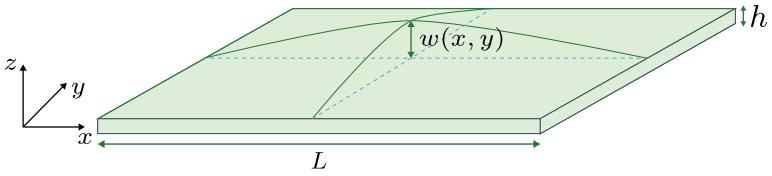

Figure 1.1: Reference frame of membrane's oscillation. $w(x, y)$ represents the out-of-plane deformation, h is the membrane thickness, and L is the side length.

The advantage of introducing a tensile stress will be discussed in sec. 1.3.2. We consider high-aspect ratio membrane of uniform thickness $h \ll L$, with the middle plane, i. e. the plane at a distance $h/2$ from both the surfaces, coinciding with the $xy-$plane. Here and within all the thesis we assume that the cross sections of the plate does not change during the oscillation. This condition leads to imposing all the stress components along the out-of-plane direction equal to zero, e. g. $\sigma_{iz} = 0$ [TK87]. Within these conditions, the displacement vector components take the form:

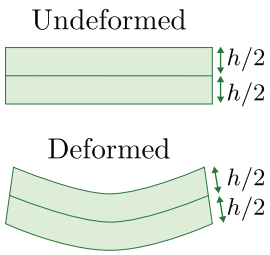

Membrane cross section.

$$d_x = v_x(x, y) - z\partial_x w(x, y) \tag{1.6a}$$
$$d_y = v_y(x, y) - z\partial_y w(x, y) \tag{1.6b}$$
$$d_z = w(x, y), \tag{1.6c}$$

where $w(x, y)$ is the out-of-plane displacement already introduced in Fig. 1.1, while $v_x(x, y)$ and $v_y(x, y)$ describe the two in-plane components of the displacement. In most of this thesis we assume that we are in the regime where v_x and v_y are negligible compared with the in-plane displacement induced by the out-of-plane motion, i. e. $-z\partial_i w$. We confirm such assumption through finite element modeling (FEM) simulationS. Where not specified otherwise, we perform the so-called *out-of-plane* approximation [AIK08] and we neglect the in-plane displacement components v_x and v_y. Within this condition, it can be proven that the in-plane components of the strain and stress tensor can be written in terms of the out-of-plane displacement as [LL70]

$$\varepsilon_{\alpha\beta} = \varepsilon_0 \delta_{\alpha\beta} - z\partial_{\alpha\beta} w, \tag{1.7a}$$

$$\sigma_{\alpha\beta} = \frac{E}{1-\nu^2}\left[(1-\nu)\varepsilon_{\alpha\beta} + \nu\varepsilon_{\gamma\gamma}\delta_{\alpha\beta}\right], \tag{1.7b}$$

where the Greek indexes denote the in-plane directions x and y. ε_0 represents an in-plane static strain giving rise to the tensile stress σ_0. Notice that both the static deformation and the static tensile stress have a spatial dependence in x and y. The Kroneker delta in front of ε_0 ensures that the static deformation does not include any shear component. We confirmed such assumption through FEM simulations.

In the discussion above we only considered a static deformation depending on the x, y position on the membrane surface. More generally, we are interested in the time dependent deformation due to the membrane vibrations induced by an external driving force or the thermal Brownian motion of the membrane itself. In this scenario, we need to include a time dependence in the out-of-plane displacement $w(x, y, t)$. The dynamics of this system can be described through the following equations [TK87]

$$\rho h\ddot{w} - \partial_{\alpha\beta} M_{\alpha\beta} - \nabla \cdot \vec{n} = F^{\text{ext}}, \tag{1.8a}$$

$$\partial_\beta N_{\alpha\beta} = 0, \tag{1.8b}$$

where ρ is the material density, F^{ext} is an external driving force applied only in the out-of-plane direction, and $\vec{n}$ is defined as follow

$$\vec{n} = \begin{pmatrix} N_{xx}\partial_x w + N_{xy}\partial_y w \\ N_{xy}\partial_y w + N_{yy}\partial_y w \end{pmatrix}. \tag{1.9}$$

In Eqs. (1.8) we introduced the so-called stress resultants $N_{\alpha\beta}$ and $M_{\alpha\beta}$ which are defined as

$$N_{\alpha\beta} = \int_{-\frac{h}{2}}^{\frac{h}{2}} \sigma_{\alpha\beta} dz, \tag{1.10a}$$

$$M_{\alpha\beta} = \int_{-\frac{h}{2}}^{\frac{h}{2}} z\sigma_{\alpha\beta} dz. \tag{1.10b}$$

The first ($N_{\alpha\beta}$) describes the shear forces, while the second ($M_{\alpha\beta}$) the bending momenta.

1.2.1 *Introducing losses*

In the model introduced in the previous section, we do not include any type of dissipation. This would lead to an equation of motion without any damping term, which is not able to describe the dynamics of real systems. To build a complete model we need to find a way to include dissipation channels in our system.

The loss channels affecting the dynamics of nanomechanical resonators can be generated by different sources, both internal and external (see sec. 1.3.1). Here we assume that the dominant source of losses are intrinsic to the resonator. To include the contribution of this loss channel in the model presented in the first part of the section, we assume there is a small time lag τ in the stress-strain relation. This delay time introduces a phase difference between the two quantities, which is described by the loss angle $\theta_{\text{lin}} = \tau\Omega_i$. For small time delays we can approximate the stress tensor as [Cat+21]:

$$\overrightarrow{\overrightarrow{\sigma}} = H(\overrightarrow{\overrightarrow{\varepsilon}}\,(t+\tau)) \approx H(\overrightarrow{\overrightarrow{\varepsilon}}\,(t)) + \tau H(\dot{\overrightarrow{\overrightarrow{\varepsilon}}}(t)), \tag{1.11}$$

where $H(\overrightarrow{\overrightarrow{\varepsilon}})$ is a linear function of $\overrightarrow{\overrightarrow{\varepsilon}}$. Writing the stress tensor components substituting Hooke's law to the linear function in Eq. (1.11) we find

$$\begin{aligned}\sigma_{\alpha\beta} &\approx \frac{E}{1-\nu^2}\left[(1-\nu)\varepsilon_{\alpha\beta} + \nu\varepsilon_{\gamma\gamma}\delta_{\alpha\beta}\right] + \frac{E\tau}{1-\nu^2}\left[(1-\nu)\dot{\varepsilon}_{\alpha\beta} + \nu\dot{\varepsilon}_{\gamma\gamma}\delta_{\alpha\beta}\right] \\ &= \sigma_{\alpha\beta}^{\text{cons}} + \sigma_{\alpha\beta}^{\text{diss}},\end{aligned} \tag{1.12}$$

where the first term ($\sigma_{\alpha\beta}^{\text{c}}$) is the conservative stress component contributing to the conservative energy, while the second term ($\sigma_{\alpha\beta}^{\text{d}}$) is the dissipative stress component giving rise to the damping term in the equation of motion. For small time delays, this approach corresponds to introducing an imaginary term in the Young modulus [SVR16].

1.2.2 *Energy contributions*

Before entering into details of the resonator dynamics, let us discuss the different energy components in a body subjected to a deformation. The work performed by the external force is converted into an energy in the deformed body. In the ideal case, where stress and strain are perfectly in phase, all this energy is stored in the body. However, the presence of a dephasing term in the stress-strain relation implies that part of this energy is dissipated within the body.

In the elastic domain, we can define the instantaneous energy density stored (δw) and dissipated ($\delta(\Delta\text{w})$) in the system as [Lau11; SVR16]

$$\delta\text{w} = \frac{1}{2}\sigma_{\alpha\beta}^{\text{cons}}\varepsilon_{\alpha\beta}, \tag{1.13a}$$

$$\delta(\Delta\text{w}) = \frac{1}{2}\sigma_{\alpha\beta}^{\text{diss}}\varepsilon_{\alpha\beta}. \tag{1.13b}$$

The total instantaneous deformation energy stored (w) and dissipated (Δw) are then obtained by integrating the above equations over the whole volume V

$$\mathrm{w} = \int_V \delta \mathrm{w} dV, \tag{1.14a}$$

$$\Delta\mathrm{w} = \int_V \delta(\Delta\mathrm{w}) dV. \tag{1.14b}$$

For periodic deformations, like the ones considered in this thesis, we can estimate the total energy stored in the system (W) and the energy dissipated in a cycle of oscillation (ΔW) through the following time integrals [SVR16]:

$$W = \frac{2\pi}{\Omega} \int_0^{2\pi/\Omega} \mathrm{w} dt, \tag{1.15a}$$

$$\Delta W = \frac{2\pi}{\Omega} \int_0^{2\pi/\Omega} \int_V \Delta\mathrm{w} dt. \tag{1.15b}$$

1.2.3 *Reduction to effective harmonic oscillator*

Equations (1.8) describe the dynamics of the total displacement field $w(x, y, t)$. However, most of the time we are interested in the dynamics of a single membrane mode of oscillations. Thus we want to simplify Eqs. (1.8) to an equation describing the motion of a point-like mass system associated with the motion of a single eigenmode.

We start by writing the stress resultants, defined in Eqs. (1.10), including the dissipative stress component introduced in Eq. (1.11). Then we plug the obtained stress resultants into Eqs. (1.8). After some algebra, we reduce to:

$$\rho h \ddot{w} + D\tau\partial_{\alpha\alpha\beta\beta}\dot{w} + D\partial_{\alpha\alpha\beta\beta}w - \nabla \cdot \vec{n} = F^{\mathrm{ext}}, \tag{1.16}$$

where we introduced the flexural rigidity $D = Eh^2/12(1-\nu^2)$ and

$$\vec{n} = h\sigma_0 \begin{pmatrix} \partial_x w \\ \partial_y w \end{pmatrix}, \tag{1.17}$$

with $\sigma_0 = E\varepsilon_0/(1-\nu^2)$. We can separate the temporal and the spatial contribution in the out-of-plane displacement field $w(x, y, t)$, and we can expand the latter over a basis of normalized modes $\phi_n(x, y)$ and their associated out-of-plane displacement u_n ($w(x, y, t) = \phi_n(x, y)u_n(t)$). We choose as normalization condition $(\phi_n)^{\max} = 1$. Within this condition, the out-of-plane displacement $u_n(t)$ represents the displacement at the mode's maximum displacement point. By performing this expansion the equation of motion becomes

$$\rho h \phi_n \ddot{u}_n + \tau(D\partial_{\alpha\alpha\beta\beta}\phi_n)\dot{u}_n + D\partial_{\alpha\alpha\beta\beta}\phi_n u_n - \nabla \cdot \vec{n} = F^{ext}, \tag{1.18}$$

where the repeated indexes are summed over. Finally, we apply a discretization method, which allows us to describe the dynamics of a

single mode in terms of effective parameters. We choose to apply the so-called *Galerkin method* [You11]. It consists on multiplying by a test function (ϕ_i) each term of Eq. (1.18) and integrating over the surface S. The resulting equation is

$$\rho h\ddot{u}_n \int_S \phi_i\phi_n dS + D(\tau\dot{u}_n + u_n)\int_S \phi_i\partial_{\alpha\alpha\beta\beta}\phi_n dS - \int_S \phi_i \nabla\cdot\vec{n}dS = f_i^{\text{ext}}, \tag{1.19}$$

where $f_i^{ext} = \int_S \phi_i F^{ext} dS$. We use the eigenmode of interest as test function. We can apply the divergence theorem to write the last term on the left hand side of the Eq. (1.19) as

$$\int_S \phi_i \nabla\cdot\vec{n}dS = \oint_{\partial S} \vec{n}\cdot\hat{n}dS - \int_S \vec{n}\cdot\nabla\phi_i dS, \tag{1.20}$$

where $\hat{n}$ is the unit vector normal to the surface, and the first integral on the right hand side vanishes because $w = \dot{w} = 0$ at the boundaries. Then, we apply the property of the normalized modes that $\int_S \phi_n\phi_i dS \propto \delta_{in}$, and we perform a single-mode approximation to neglect intermodal coupling. Within this approximation, Eq. (1.19) reduces to the effective equation

$$\ddot{u}_i + \Gamma_i\dot{u}_i + \Omega_i^2 u_i = \frac{f_i^{ext}}{m_i}, \tag{1.21}$$

with the following effective parameters:

$$m_i = \int_S h\rho\phi_i^2 dS, \tag{1.22}$$

$$\Gamma_i = \frac{D\tau}{m_i}\int_S \phi_i\partial_{\alpha\alpha\beta\beta}\phi_i dS, \tag{1.23}$$

$$\Omega_i^2 = \frac{1}{m_i}\int_S \phi_i\left[D\partial_{\alpha\alpha\beta\beta}\phi_i + h\sigma_0\left(\partial_x\phi_i + \partial_y\phi_i\right)^2\right]dS. \tag{1.24}$$

It is important to notice that the same model can be applied in the simple case of $\sigma_0 = 0$. In this case, we recover the case of a square plate, where Γ_i and Ω_i share the same spatial dependence on the eigenmodes and they only differ for the time delay.

As the reader probably already recognized, Eq. (1.21) is the equation of motion of a damped, driven harmonic oscillator. It means that, if we focus on the motion of a single mechanical mode, we can imagine it as a spring-mass system. For the purpose of this thesis, we are interested in both the free evolution and in its driven response. For completeness, in the following sections, we show the solution of the equation of motion in the two mentioned cases. From these solution we find the laws we use in the experimental section to estimate the damped harmonic oscillator parameters, and to derive the calibration method.

1.2.4 *Free evolution*

We first consider the free evolution of a damped harmonic oscillator. We assume that the membrane is initially displaced to an amplitude $u_i(0) = A_0$, and that no force is applied, e. g. $f_i^{\text{ext}} = 0$. We can classify the damped harmonic oscillator accordingly to the ratio between the linewidth Γ_i and the resonance frequency Ω_i. We can distinguish between three different cases:

- *overdamped*, $\Gamma_i \gg \Omega_i$;
- *critically damped*, $\Gamma_i = 2\Omega_i$;
- *underdamped*, $\Gamma_i \ll \Omega_i$.

All the resonators studied in this thesis fall in the last category. In the underdamped case, the solution takes the following form:

$$u_i(t) = A_0 e^{-\frac{\Gamma_i}{2}t} \sin(\Omega_i t + \phi). \tag{1.25}$$

An underdamped harmonic oscillator initially displaced from its equilibrium point is ringing down to its rest position with a decay rate equal to $\Gamma_i/2$. The displacement amplitude $A_i(t)$ decays exponentially to its

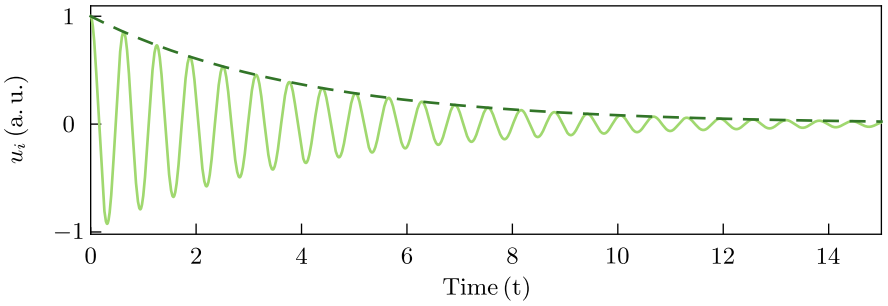

Figure 1.2: Free evolution of an initially displaced underdamped harmonic oscillator. The resonator decays to its rest position oscillating around it. The light, green, solid line represents the decay of the displacement u_i, while the dark, green, dashed line represents only the displacement amplitude decay $A_0 e^{-\frac{\Gamma_i}{2}t}$.

rest position with a rate defined by the damping

$$A_i(t) = A_0 e^{-\frac{\Gamma_i}{2}t}. \tag{1.26}$$

Thus, by monitoring the displacement amplitude $A(t)$ during the ringdown time, and by using Eq. (1.26) as fitting function, we can extract the damping rate Γ_i decay. This is what we define a *ringdown measurement* and it is widely used throughout this thesis.

In the underdamped regime, the larger the number of oscillations the membrane resonator performs before reaching the steady state, the

lower the dissipation. At this point, we can introduce a very significant quantity associated with the nanomechanical resonators, the so-called *quality factor* (Q). It is a dimensionless parameter associated with the amount of damping in the system. Here we give two definitions of the quality factor, which are almost equivalent in the limit of low damping rate. Physically, it represents the ratio between the total energy stored in the system (W, see Eq. (1.15a)), over the dissipated by the system during one cycle of oscillation (ΔW, see Eq. (1.15b), that is [SVR16]

$$Q = \frac{W}{\Delta W}. \tag{1.27}$$

Thus having a high quality factor means having low dissipation. The quality factor can be also defined in terms of measurable parameters as [SVR16]

$$Q = \frac{\Omega_i}{\Gamma_i}. \tag{1.28}$$

1.2.5 *Driven response*

To study the membrane response in the presence of an external driving force, e. g. either an external harmonic force or the thermal Langevin force [Kub66], it is convenient to move to the frequency domain. We define the *Fourier transform*:

$$\mathcal{F}(f(t))(\Omega) = \int_{-\infty}^{\infty} f(t) e^{-it\Omega} dt. \tag{1.29}$$

The frequency domain significantly simplifies Eq. (1.21). Moreover, it allows us to distinguish the contribution of different modes and eventually focus on a single normalized mode at the time.

We move to the frequency domain by applying Eq. (1.29) on both sides of Eq. (1.21), which becomes

$$-\Omega^2 u_i(\Omega) - i\Gamma_i \Omega u_i(\Omega) + \Omega_i^2 u_i(\Omega_i) = \frac{f_i^{ext}(\Omega)}{m_i}, \tag{1.30}$$

where f_i^{ext} is the Fourier transform of the driving force and we applied the property of the Fourier transform $\mathcal{F}(\partial_t^n f(t)) = (-i\Omega)^n \mathcal{F}(f(t))$. The solution of the above equation, and of Eq. (1.21), is

$$u_i(\Omega) = \chi f_i^{ext}(\Omega), \tag{1.31}$$

where we introduced the mechanical susceptibility

$$\chi = \frac{1}{m_i(-\Omega^2 + \Omega_i^2 - i\Gamma_i\Omega)}. \tag{1.32}$$

In the underdamped regime, where the susceptibility can be approximated by a Lorentzian function centered at Ω_i, the solution takes the form

$$u_i(\Omega) = \frac{f_i^{ext}(\Omega)}{2m_i\Omega_i\left(\Omega_i - \Omega - i\frac{\Gamma_i}{2}\right)}. \tag{1.33}$$

Notice that $u_i(\Omega)$ is a complex number describing a harmonic motion $A\sin(\Omega_i t + \varphi)$. From the magnitude and the phase of Eq. (1.33), we find the amplitude and phase response of a harmonic oscillator to an external drive, see Fig. 1.3.

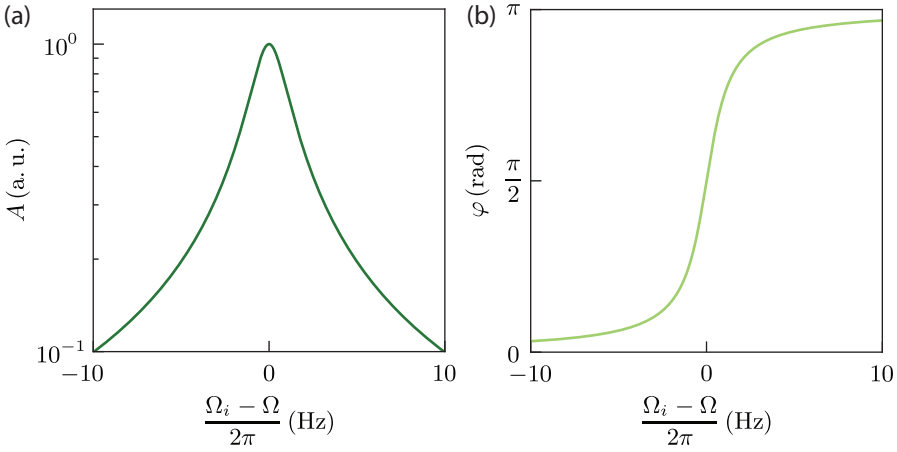

Figure 1.3: Frequency response of a driven, damped harmonic oscillator. (a) Displacement amplitude against the frequency detuning between the external force frequency and the resonance frequency. (b) Displacement phase against the frequency detuning between the external force frequency and the resonance frequency.

In practice, the motion fluctuates, e. g., due to a fluctuating force, thus we cannot extract much information from a single realization $u_i(\Omega)$. Instead, we need to estimate statistical quantities, in particular we measure the quantity $\langle |u_i(\Omega)|^2 \rangle$, where $\langle \cdot \rangle$ denotes the average over several experimental repetitions and it coincides with the Fourier transform of the autocorrelation function, i. e. the power spectral density (PSD)

$$S_{uu}(\Omega) = \langle |u_i(\Omega)|^2 \rangle, \tag{1.34}$$

where we defined the PSD as

$$S_{uu}(\Omega) = \int_{-\infty}^{+\infty} \langle u(t)u(0) \rangle e^{-i\Omega t} dt. \tag{1.35}$$

By using Eq. (1.34) and Eq. (1.33), we find that the PSD of for a driven oscillator displacement is

$$S_{uu}(\Omega) = |\chi|^2 S_{FF}, \tag{1.36}$$

where S_{FF} is the PSD of the driving force. When the driving force is the thermal Langevin force, we can evaluate S_{FF} by using the fluctuations dissipation theorem. In doing so, we find that it takes the form [Kub66]:

$$S_{FF} = 2m_i k_B T \Gamma_i, \tag{1.37}$$

where k_B is the Boltzmann constant. From the definition of PSD and the relation presented in Eq. (1.34), we can derive the following property [AKM14]

$$\int_{-\infty}^{\infty} S_{uu} \frac{d\Omega}{2\pi} = \langle u^2 \rangle, \tag{1.38}$$

meaning that the area under the mechanical noise spectrum coincides with the variance of the mechanical displacement.

Alternatively, we can solve Eq. (1.21) in the time domain through the ansatz

$$u(t) = X_1(t)\cos(\Omega_i t) + X_2(t)\sin(\Omega_i t), \tag{1.39}$$

where $X_1(t)$ and $X_2(t)$ represent the time-dependent amplitudes of the cosine and sine components of the oscillation. They are often called mechanical quadratures and they are related to the amplitude and phase of the signal through the following relations:

$$A(t) = \sqrt{X_1^2(t) + X_2^2(t)}, \tag{1.40a}$$

$$\varphi(t) = \arctan\left(\frac{X_2(t)}{X_1(t)}\right). \tag{1.40b}$$

Substituting Eq. (1.39) in Eq. (1.21), and writing the driving force as $f_{i,\mathrm{c}}(t)^{\mathrm{ext}}\cos(\Omega_i t) + f_{i,\mathrm{s}}^{\mathrm{ext}}(t)\sin(\Omega_i t)$, the equation of motion expressed in terms of the two quadratures coincides with the two following equations [VF13]:

$$\dot{X}_1 + \frac{\Gamma_i}{2} X_1 = \frac{f_{i,\mathrm{s}}^{\mathrm{ext}}}{2\Omega_i}, \tag{1.41a}$$

$$\dot{X}_2 + \frac{\Gamma_i}{2} X_2 = -\frac{f_{i,\mathrm{c}}^{\mathrm{ext}}}{2\Omega_i}, \tag{1.41b}$$

where we neglected all the terms proportional to $X_i \Omega_i^{-1}$. The above equations are two linear differential equations of the first order that we can easily solve finding:

$$X_1 = e^{-\frac{\Gamma_i}{2}t}\left[c_1 + \int_{t_0}^{t} \frac{f_{i,\mathrm{s}}^{\mathrm{ext}}}{2\Omega_i} e^{\frac{\Gamma}{2}s} ds\right], \tag{1.42a}$$

$$X_2 = e^{-\frac{\Gamma_i}{2}t}\left[c_1 - \int_{t_0}^{t} \frac{f_{i,\mathrm{c}}^{\mathrm{ext}}}{2\Omega_i} e^{\frac{\Gamma}{2}s} ds\right]. \tag{1.42b}$$

In Fig. 1.4 (a), (b) we show the two interesting situations of $f_{i,\mathrm{c}}^{\mathrm{ext}} = f_{i,\mathrm{s}}^{\mathrm{ext}} = constant$, and $f_i^{\mathrm{ext}} = 0$, $u_i(0) = A_0$. In the particular case of a thermally-driven oscillator, where $f_{i,\mathrm{s}}^{\mathrm{ext}}$ and $f_{i,\mathrm{c}}^{\mathrm{ext}}$ are two stochastic random processes, we can solve Eqs. (1.41) in the frequency domain.

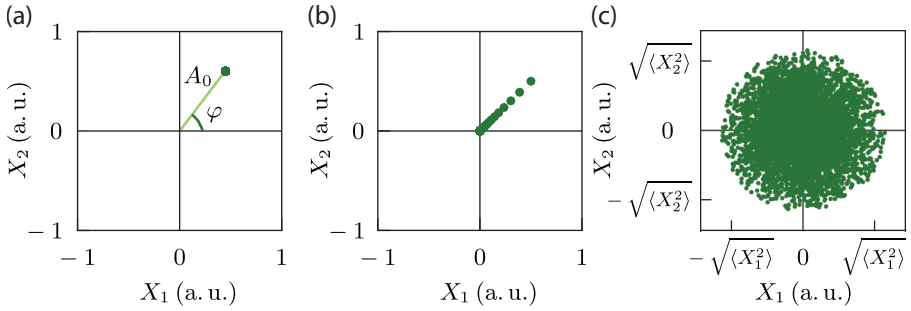

Figure 1.4: Solution of the equation of motion in terms of the two mechanical quadratures. (a) X_1 against X_2 when an external driving force is applied to the oscillator. The angle φ is the phase of the oscillation and it is defined by the phase of the resonant drive, i. e. the relative weight of $f_{i,\mathrm{s}}^{\mathrm{ext}}$ and $f_{i,\mathrm{c}}^{\mathrm{ext}}$. The length of the vector A_0 is the amplitude of the oscillation (b) X_1 against X_2 for a damped harmonic oscillator during its free decay. The two quadratures evolves in time and decay towards the center, i. e. the rest position. Each point represent a different time. (c) X_1 against X_2 for a harmonic oscillator subjected to the thermal Langevin force. Each point represents a different time and it is characterized by a random magnitude and a random phase.

Applying again the properties of the Fourier transform we find the solutions

$$X_1(\Omega) = \frac{\mathcal{F}_{i,\mathrm{s}}^{\mathrm{ext}}}{2\Omega_i\left(\frac{\Gamma_i}{2} - i\Omega\right)}, \tag{1.43a}$$

$$X_2(\Omega) = -\frac{\mathcal{F}_{i,\mathrm{c}}^{\mathrm{ext}}}{2\Omega_i\left(\frac{\Gamma_i}{2} - i\Omega\right)}, \tag{1.43b}$$

where $\mathcal{F}$ represents the Fourier transform of the random force components. Already from Eqs. (1.43), we recognize that the two quadratures are fluctuating randomly with the stochastic force describing the motion of an oscillations with random amplitude and phase as expected, see Fig. 1.4 (c). The amplitude of these oscillations depends on the strength of the thermal force. It is interesting to evaluate the variance of the thermal fluctuations, representing the mean square radius of the random distribution in Fig. 1.4 (c). We first need to evaluate the PSD of the two quadratures. Applying the same properties of the PSD outlined in the first part of the section, from Eqs. (1.43) we estimate

$$S_{X_1X_1}(\Omega) = \frac{m_i k_{\mathrm{B}} T}{2\Omega_i Q\left(\frac{\Gamma_i^2}{4} + \Omega^2\right)}, \tag{1.44a}$$

$$S_{X_2X_2}(\Omega) = \frac{m_i k_{\mathrm{B}} T}{2\Omega_i Q\left(\frac{\Gamma_i^2}{4} + \Omega^2\right)}, \tag{1.44b}$$

where we use Eq. (1.37) to express the PSD of the thermal force. Substituting the above PSDs in Eq. (1.38) we evaluate the variances

$$\langle X_1^2 \rangle = \langle X_2^2 \rangle = \frac{k_B T}{2 m_i \Omega_i^2}. \tag{1.45}$$

1.3 ENHANCING THE RESONATOR'S QUALITY

A resonator at a temperature T is always subjected to a random thermal force. This stochastic force induces random fluctuations of the resonator motion, and generates a noise characterized by the noise spectrum defined in Eq. (1.37). This thermal noise set a lower bound on the forces that can be detected on a nanomechanical resonator. We refer to it as the *force spectral sensitivity*, and to its square root as *force sensitivity*. A large number of nanomechanical resonators have been operated with a very low effective mass and a very high quality factor [Tsa+17; Gha+18; Bec+21a; Bec+21b; Ber+21]. Moreover, the current technologies allow us to operate them at temperatures of only a few mK. These features enabled force sensitivities of the order of $\mathrm{aN}/\sqrt{\mathrm{Hz}}$, or lower, making nanomechanical resonators interesting platforms for force sensing experiments.

To reduce the force sensitivity of a nanomechanical resonator two main paths can be followed. On one hand, we can engineer our resonator to reduce its effective mass. On the other hand, we can search for a method to increase its quality factor. In this section we will focus on the latter by presenting the most common source of losses in suspended nanomechanical resonators and the two main techniques applied to increase the quality factor in the devices studied in this thesis.

1.3.1 *Loss channels*

We can divide the sources of dissipation affecting the nanomechanical resonators studied in this thesis into three groups: external source of dissipation, dissipation due to the clamping and internal friction. The rate at which the resonator dissipate energy is determined by the sum of all the loss channels. Recalling the definition of quality factor in Eq. (1.27), we can write the total losses as

$$Q^{-1} = Q_{\mathrm{ext}}^{-1} + Q_{\mathrm{clamp}}^{-1} + Q_{\mathrm{intr}}^{-1} + \ldots, \tag{1.46}$$

where we wrote explicitly only the contributions constituting the three sources mentioned at the beginning. Understanding the origin of these three loss channels is important to mitigate the amount of energy dissipated through them. Several mechanisms can fall in these three groups. In the following we describe only the loss channels relevant for the treatment performed in this thesis.

Gas damping losses

The gas damping losses constitute one of the most common sources of external dissipation in nanomechanical resonators operated in air or in vacuum environment. When a mechanical resonator is surrounded by gas molecules, the interactions between the gas molecules and the resonator lead to a loss channel. We can define this source of losses as an external effect and we can mitigate it by reducing the amount of gas molecules surrounding the resonator, i. e. placing it in a vacuum environment.

The gas damping losses are determined by the pressure and the nanomechanical oscillator geometry, in particular the ratio between surface and volume. We distinguish two regimes associated with this loss channel, the fluidic regime and the ballistic regime. We can determine if we are in the ballistic or fluidic regime by evaluating the so-called *Knudsen number* [SVR16], K_n, which is defined as the ratio between the mean free path of the gas λ_f (associated with the pressure) and the representative physical length scale L_c. For $K_n < 1$ we are in the fluidic regime, while for $K_n > 1$ we are in the ballistic regime.

We mostly work in a vacuum environment characterized by a pressure of the order of $\approx 10^{-7}$ mbar. Such pressure is associated with the ballistic regime in our membrane resonators. In this pressure regime, the density of gas molecules is so low that we can assume they are not interacting with each other, and that the gas losses are produced by elastic collisions between the gas molecules and the resonator. The law describing the gas damping losses in the ballistic regime is the following [Bia+06]

$$Q_{\text{gas}}^{-1} = \left[\frac{\rho h \Omega}{4}\sqrt{\frac{\pi}{2}}\sqrt{\frac{RT}{M_m}}\frac{1}{P}\right]^{-1}, \tag{1.47}$$

where ρ, h and Ω are the density, the thickness and the resonance frequency of the resonator respectively, R is the gas constant, T is the absolute temperature, M_m is the mass of the gas molecules expressed in g/mol and P is the pressure.

Clamping losses

The clamping losses represent the losses due to the radiation of elastic waves into the substrate through the supports of the resonator, i. e. the clamping points [AKM14]. A resonator suspended on a solid frame, and vibrating at a frequency Ω, produces a shear wave propagating into the solid frame with a wavelength $\lambda_s = c_s/\Omega$ [Jud+07]. c_s is the shear waves propagation speed which depends on the material properties of the substrate. If the substrate thickness is larger than λ_s, we can model the clamping losses considering the frame having a semi-infinite thickness. For the system considered in this thesis, we are always in this limit. In the past years, analytic modelings of anchor loss contri-

butions have been proposed for cantilevers and doubly-clamped beams [Jud+07], square membranes and disk resonators [WR+11]. We reduce the clamping losses contribution by preventing the shear wave propagation, therefore we usually neglect them. For further details see Sec. 1.3.3.

Intrinsic losses

Under this name we summarize all those mechanisms happening inside the material itself. They include friction due to phonon-phonon interaction [KI08], anharmonicity due to thermoelastic damping [Duw+06] and material induced losses such as two-level system losses happening at the surface [RBT09]. Differently from the other two types of dissipation, we cannot act on the source of the intrinsic losses to reduce them. Moreover, we cannot easily distinguish between the different contribution giving rise to them. Nevertheless, a phenomenological description of the magnitude of the intrinsic losses for SiN membrane of different thicknesses has already been provided in [VS14]. In that work, the authors compared the intrinsic quality factors measured on several SiN membranes with different thicknesses h and dimensions L. The first observation they make is that the intrinsic quality factors, and therefore the intrinsic losses, do not depend on the side length L. Then they notice that for small thicknesses the intrinsic losses increase linearly. The authors attribute the thickness-dependent losses with losses happening at the surface. As the thickness increases the intrinsic losses grow linearly until they reach a saturation which coincides with the regime where the volume losses dominate over the surface losses. We can summarize this dependence of the intrinsic losses on the membrane thickness with the following phenomenological formula [VS14]:

$$Q_{\text{intr}}^{-1} = Q_{\text{surf}}^{-1}(h) + Q_{\text{vol}}^{-1}, \tag{1.48}$$

where $Q_{\text{surf}}(h)^{-1} = (\alpha h)^{-1}$. Q_{surf}^{-1} represents the thickness-dependent surface losses, while Q_{vol}^{-1} represents the volume losses. Due to the phenomenological origin of the description, the uncertainty on the intrinsic loss value is large. In particular, in [VS14] the authors estimated the values $\alpha = (6 \pm 4) \times 10^{10}\,\text{m}^{-1}$ and $Q_{\text{vol}} = 28000 \pm 2000$.

From the discussions above, we realize that we can mitigate or remove the contribution of the first two sources of dissipation by acting on the experimental environment, i. e. placing the membrane resonator in ultra high vacuum (UHV) environment, or through designing a resonator such that we prevent the shear waves propagation (see Sec. 1.3.3). On the contrary, we cannot act directly on reducing the intrinsic losses. Thus, the intrinsic losses determine the ultimate limiting factor for the losses in our nanomechanical resonators, and they usually represent the main source of dissipation in our experiments.

1.3.2 *Dissipation dilution*

Despite the lack of information regarding their origin, the intrinsic losses set a lower limit to the dissipation in the system. A number of alternative techniques have been developed to increase the quality factor circumventing this limit. One of the most famous and used is the *dissipation dilution technique*.

The dissipation dilution technique has been introduced in the first place by the LIGO collaborations [Gon00; Cag+00], and later has been applied to nanomechanical resonators [Ver+07; UFPK10; Sch+11; Fed+19]. The basic idea consists in introducing a purely conservative energy term in the system. In clamped resonators, such as strings and membranes, this is achieved introducing an in-plane, time-independent tensile stress during the fabrication process.

To understand how the dissipation dilution works, we start evaluating the different energy terms in a deformed membrane (or string) without a tensile stress involved. We can evaluate the instantaneous deformation energy stored and dissipated by knowing the stress and the strain in our resonator (see Eqs. (1.14)). Generally, an oscillating string or membrane experienced two types of deformations: bending and elongation. The former is described by the first order terms in the strain tensor components which coincide with in Eq. (1.2), the elongation by the second order terms. For a thin membrane satisfying the condition listed at the beginning of Sec. 1.2, the bending strain coincides with Eq. (1.7a) and we can include the elongation as an additional term with the form $\partial_\alpha w \partial_\beta w/2$. More details regarding the contribution of the elongation term will be discussed in Chapter 4. Using the definitions in Eqs. (1.14) we identified two contributions for both the stored and dissipated energy, one due to the bending and the other to the elongation. We analyze them one at the time. We start with the instantaneous bending energy term, which has the following form

$$\begin{aligned} \mathrm{w}_{\mathrm{bend}} = &\frac{E u_i^2}{2(1-\nu^2)} \int_V z^2 (\partial_{xx}\phi_i + \partial_{yy}\phi_i)^2 dV + \\ &- \frac{E u_i^2}{(1+\nu)} \int_V z^2 (\partial_{xx}\phi_i \partial_{yy}\phi_i - (\partial_{xy}\phi_i)^2 dV, \end{aligned} \tag{1.49}$$

where the argument of the first integral is the mean curvature squared and the second one is the Gaussian curvature. It can be proven that for a clamped membrane the latter is zero [YPR12; SVR16]. The dissipated bending energy has a similar expression

$$\Delta \mathrm{w}_{\mathrm{bend}} = \frac{E\tau u_i \dot{u}_i}{2(1-\nu^2)} \int_V z^2 (\partial_{xx}\phi_i + \partial_{yy}\phi_i)^2 dV, \tag{1.50}$$

where we neglected the Gaussian curvature. Similarly, we can write the instantaneous elongation energy stored and dissipated as

$$\mathrm{w}_{\mathrm{elong}} = \frac{E u_i^4}{8(1-\nu^2)} \int_V \left[(\partial_x \phi_i)^2 + (\partial_y \phi_i)^2 \right]^2 dV, \tag{1.51}$$

$$\Delta \mathrm{w}_{\mathrm{elong}} = \frac{E \tau u_i^3 \dot{u}_i}{8(1-\nu^2)} \int_V \left[(\partial_x \phi_i)^2 + (\partial_y \phi_i)^2 \right]^2 dV. \tag{1.52}$$

Any other instantaneous energy terms coming form the product between stress and strain have been neglected since their contribution average to zero when we evaluate the total energy and the energy dissipated per unit cycle.

Substituting the expressions for the instantaneous stored and dissipated energies in Eqs. (1.15), we find all the energy contributions. We can use them to write the quality factor of a membrane in absence of a tensile stress as

$$Q = \frac{W_{\mathrm{bend}} + W_{\mathrm{elong}}}{\Delta W_{\mathrm{bend}} + \Delta W_{\mathrm{elong}}}. \tag{1.53}$$

Let us now include the contribution of the tensile stress σ_0. The main property of this tensile stress is that it does not evolve in time, therefore it does not introduce losses due to the dephasing in the stress-strain relation. We refer to the purely conservative energy associated with σ_0 as *tensile energy*. Including σ_0 in the expression for the stress, we can evaluate the instantaneous tensile energy stored in the system which has the following expression

$$\mathrm{w}_{\mathrm{tensile}} = \frac{\sigma_0 u_i^2}{2} \int_V \left[(\partial_x \phi_i)^2 + (\partial_y \phi_i)^2 \right] dV. \tag{1.54}$$

Substituting the above expression in Eq. (1.15a) we can evaluate the tensile energy (W_{tensile}). With this additional energy term the quality factor defined in Eq. (1.27) becomes

$$Q = \frac{W_{\mathrm{tensile}} + W_{\mathrm{bend}} + W_{\mathrm{elong}}}{\Delta W_{\mathrm{bend}} + \Delta W_{\mathrm{elong}}}. \tag{1.55}$$

In this thesis we assume the condition $W_{\mathrm{tensile}} \gg W_{\mathrm{bend}}, W_{\mathrm{elong}}$ is always satisfied. Within this condition we can write

$$Q = \left(1 + \frac{W_{\mathrm{tensile}}}{W_{\mathrm{bend}} + W_{\mathrm{elong}}} \right) \frac{W_{\mathrm{bend}} + W_{\mathrm{elong}}}{\Delta W_{\mathrm{bend}} + \Delta W_{\mathrm{elong}}} \approx D_Q Q_{\mathrm{intr}}, \tag{1.56}$$

where we introduced the *dissipation dilution factor*

$$D_Q = \left(1 + \frac{W_{\mathrm{tensile}}}{W_{\mathrm{bend}} + W_{\mathrm{elong}}} \right), \tag{1.57}$$

which is always larger than 1. We want to highlight that the quality factor increases because of this extra lossless tensile energy term, but the losses are not reduced. They are *diluted* by the presence of the tensile stress.

1.3.3 *Soft clamping*

Indeed the presence of a tensile stress σ_0 allows us to increase a quality factor adding a purely conservative energy term. However, the increase we can get is limited by the amount of tensile stress we can introduce in the system. In order to have a further improvement on the quality factor we need to understand the limiting factors on the dissipation side.

For simplicity we consider the case of a doubly-clamped beam. The boundary conditions imposed by the two clamping points require that the beam does not move at the edges, and that it is parallel to the frame at the clamping points. Imposing these boundary conditions, the modeshapes follow a sinusoidal function around the maximum displacement point but they show a strong bend at the edges (see Fig. 1.5).

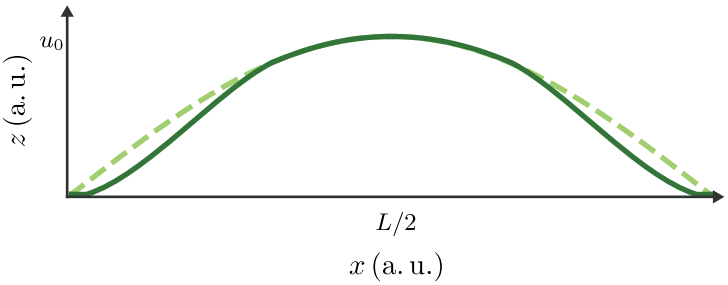

Figure 1.5: First modeshape of a doubly-clamped beam showing a strong bend at the edges. The light green dashed line represents the ideal sinusoidal modeshape for comparison.

The dominant losses in strings and membrane are introduced by the bending. By evaluating ΔW_{bend}, it arises that the main contribution to this loss channel comes from the strong bend that the membrane experiences at the clamping points [SVR16]. The amount of losses at the edges represents the main limitation to the quality factor on a highly-stressed resonator. To beat this limit, the concepts of *soft clamping* has been introduced [Tsa+17]. It consists in engineering the modeshapes such that the displacement gradually reduces from the center to the edges allowing an increment of the quality factor due to bending loss reduction [Tsa+17; Gha+18].

The type of membrane resonators studied in this thesis are realized using both the dissipation dilution and the soft clamping techniques. They consist on highly-stressed Si_3N_4 thin (h ranging from 14 nm to 100 nm, $L \approx 3$ mm) membrane suspended on a Si frame. The tensile stress σ_0 introduced during the fabrication process is approximately 1.3 GPa. The membrane is patterned with a honey comb lattice which open a phononic bandgap in the mechanical spectrum (see Fig. 1.6 (a)). By breaking the periodicity of the phononic crystal we can insert a *defect* in the center of the structure. We can design it such that it

can sustain strongly localized modes with frequencies lying inside the bandgap. The first order localized mode is shown in Fig. 1.6 (b). First of all, the phononic bandgap provides an isolation from the environment and it contributes to reduce the loss channels associated with clamping losses. Moreover, it changes the boundary conditions such that the out-of plane defect motion exponentially decays from the center to the clamping points. Thus the membrane is almost not moving at the frame (see Fig. 1.6 (c)). The membrane resonators fabricated with this process have been measured to have a quality factor of the order of 10^8 at room temperature [Tsa+17] and up to 10^9 at moderate cryogenic temperature [Ros+18].

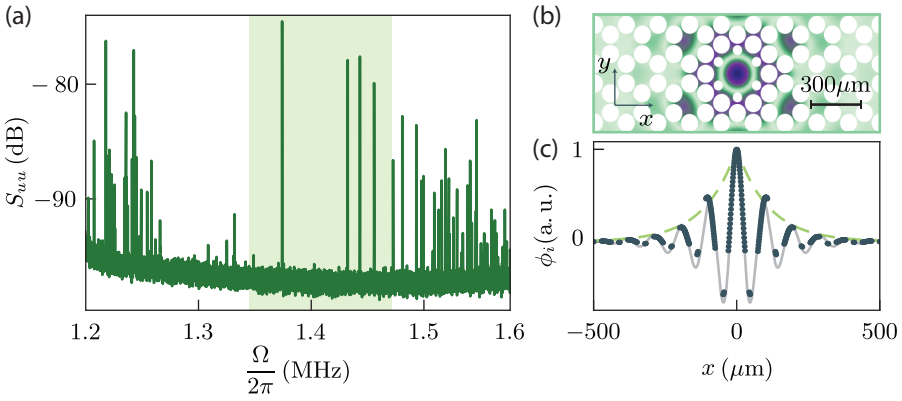

Figure 1.6: Soft-clamped membrane resonator. (a) Measured PSD of a soft-clamped membrane resonator. The light green area highlight the phononic bandgap. (b) Simulation of the first-order bandgap mode. The colors, from light to dark, represents the magnitude of the out-of-plane displacement. (c) Cross section of the simulated mode-shape. The points are the simulation, the grey solid and light green dashed lines are two superimposed models meant to highlight the exponential decay of out-of-plane oscillation from the center to the frame.

1.3.4 *Defect designs*

The concept of soft-clamped membrane resonator has been further developed in recent years. By modifying the defect design or the phononic crystal structure we can obtain membrane resonators with different properties. The experiments conducted in this thesis have been realized on a selection of different soft-clamped membrane designs. To distinguish the different types of geometries we gave specific names to the membrane resonators which are associated with the defect shapes. In the following we introduced the three different soft-clamped membrane resonators used to conduct the experiments in this thesis.

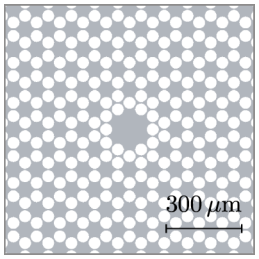

Dahlia - generation 1

Dahlia - generation 1. It is the first generation of soft-clamped membranes realized [Tsa+17]. The phononic crystal consists of circles with a honey comb lattice configuration. Choosing a lattice constant $a \approx 160\mu$m, a holes raddii $r = 0.26\,a$ and a sidelength of approximately 3 mm, this design shows a ≈ 200 kHz wide bandgap centered at 1.4 MHz. It features 5 bandgap modes and a defect dimension corresponding to approximately 2 lattice constants. The central pad, i. e. the defect area useful for optical readout, has a dimension of $\approx 200\,\mu$m. The effective mass of the first bandgap mode for a thickness of 15 nm is $\approx$ 1ng. Building upon this membrane design we realize the phononic dimer geometry which we will discuss in Chapter 5.

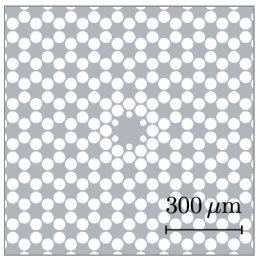

Dahlia - generation 2

Dahlia - generation 2. Second generation soft-clamped resonators. It maintains the same phononic crystal structure of the first generation. The main difference consists in the presence of six smaller holes on the defect. This modification on the defect design shifts the frequency of the 5 bandgap modes, however the bandgap itself is not affected since it is only characterized by the phononic crystal geometry. The 5 bandgap modes have a very similar modeshape with respect to the Dahlia generation 1 design, but the mode order changes, see appendix A for all modeshapes. It has been first utilized in [Ros+18] to circumvent a mirror noise problem and it has been used for several interesting works in quantum science [Ros+18; Ros+19; Mas+19; Che+20; Tho+20].Considering the wide use of this geometry, we decided to perform the characterization of the geometric nonlinearities presented in Chapter 4 on these devices.

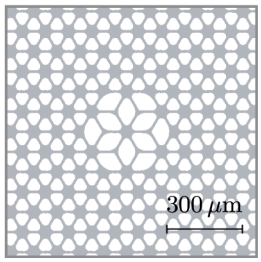

Lotus

Lotus. New generation of soft-clamped membranes where both the defect and the phononic crystal have been modified from the initial generation. The phononic crystal is a honey comb lattice formed by rounded triangles instead of circles. It is characterized by a wider bandgap ($\approx$ 300 kHz) centered around 1.5 MHz. It features a single bandgap mode and the defect design can be tailor in order to shift the localized mode frequency within the bandgap. It is characterized by a higher quality factor than the Dahlia designs (between 4% and 40%). The defect corresponds to approximately 3 unit cells and the central pad is usually fabricated with a dimension varying from 60 μm to 135 μm. The higher frequency together with the higher quality factor and the wider bandgap makes this membrane design robust to added masses at the center. Consequently, it has been first utilized for electromechanics applications [Sei+21]. However, the robustness to mass deposition makes it interesting for sensing application as well. Its potential for force sensing experiments through parametric protocols has been explored with a dimer configuration in [H¨+21a].

2

OPTICAL SYSTEM

The optical interferometers are very versitile instruments which can be used for different applications, such as refractive index sensing [Fen82], spectrometry [Cor+15], vibrometry [PHW86] or astronomical applications [WPM80]. We are interested in their application as displacement sensors. The most famous of this application is the gravitation wave detector [Abb+09]. The simplest optical interferometer we can think of is the Michleson interferometer. In this chapter we introduce the working principle of a Michelson interferometer, and we discuss how we can use it to measure a small displacements. In doing so, we introduce an alternative interferometer geometry which fits best our experimental requirements discussing two possible detection configurations. At the end of the chapter we present the possible noise sources and the best noise condition we can reach in the setup presented.

2.1 MICHELSON INTERFEROMETER

A Michelson interferometer is a common optical setup constituted by one beam splitter (BS) and two mirrors, which uses as measurement tool the interference fringes generated between two light beams. It has been first introduced by A. A. Michelson in 1880 and the basic scheme is sketched in Fig. 2.1. It consists of a light source S characterized

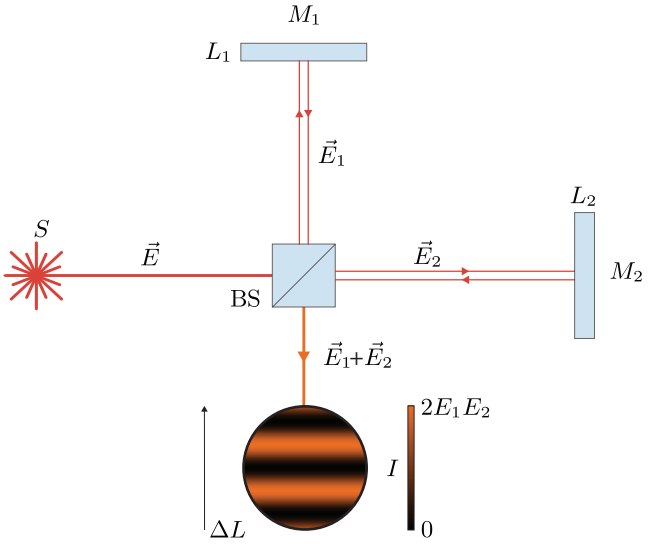

Figure 2.1: Sketch of a Michelson Interferometer. S = light source, M =mirror, BS =beam splitter, $\vec{E}_i$ = electric field, L_i = distance of M_i from the BS, I = light intensity, $\Delta L = L_2 - L_1$.

by a wavelength λ, which generates an electric field $\vec{E}(t) = \vec{E}_0 e^{i\Omega_L t}$. The latter travels towards a 50 : 50 BS placed at a distance L from the source. After the BS the initial electric field is divided into two fields with same intensities $\vec{E}_1(t) = -\vec{E}_0 e^{i(\Omega_L t)}/\sqrt{2}$ and $\vec{E}_2(t) = \vec{E}_0 e^{i(\Omega_L t)}/\sqrt{2}$. Here Ω_L is the frequency of the light source and $k = 2\pi/\lambda$ is its wave number. The two fields travel through the two interferometer arms and are reflected back. They recombine on the BS and they are detected on a photodetector placed after it. The two beams travel through two different path lengths $2L_1$ and $2L_2$, respectively, hence they are phase shifted. The resulting field at the detector is the sum of the two electric fields and the light intensity is

$$\begin{aligned} I &= \left| -\frac{\vec{E}_0}{\sqrt{2}} e^{i(\Omega_L t + 2kL_1)} + \frac{\vec{E}_0}{\sqrt{2}} e^{i(\Omega_L t + 2kL_2)} \right|^2 \\ &= \frac{I_0}{2} - \frac{I_0}{2}\cos(2k\Delta L), \end{aligned} \tag{2.1}$$

where $I_0 = |E_0|^2$ and $2k\Delta L$ represents the phase shift due to the path difference. The last term represents the interference term between the two beams. We can move from purely constructive interference (white fringes) to purely destructive interference (dark fringes) by varying the path difference between the two interferometer arms. The interference fringes are shown in the contour plot in Fig. 2.1.

In the treatment above we assumed a perfectly coherent, monochromatic light source with a constant amplitude. In a real experiment these three conditions are not always perfectly satisfied. Imperfections in the light source quality and in the beam alignment result in a worse quality of the fringes. The intensity oscillates between a maximum ($I_{\max}$) and a minimum ($I_{\min}$) and the difference between this two values defines the *fringe visibility* $\mathcal{V}$ [Fow89]

$$\mathcal{V} = \frac{I_{\max} - I_{\min}}{I_{\max} + I_{\min}}, \tag{2.2}$$

where the case of a perfect interferometer coincides with the case of $\mathcal{V} = 1$.

2.2 HOMODYNE DETECTION SCHEME

The homodyne detection scheme is a method to extract information on a phase modulated signal by mixing it with a reference signal characterized by the same carrier frequency.[1] In an optics framework, we talk about homodyne detection every time we have an interference signal between a reference signal and a phase modulated signal, both characterized by the same frequency. Usually the reference beam has an intensity larger than the phase modulated one. On one hand the reference beam allows us to extract the information embedded as a phase modulation in the

1 From greek '*homòs*'=same.

signal, on the other hand it amplifies it. A Michelson interferometer where we replace one of the two mirrors with a moving object can always be seen as an homodyne scheme.

One could use the setup described in Fig. 2.1 to measure small displacements, in particular the motion of a thin membrane oscillating in time $\delta u(t)$. To do so, it is enough to replace one of the interferometer mirrors with the moving membrane. Usually the membrane is characterized by a low reflectivity ($\mathcal{R} \sim 1 - 10\%$). The membrane motion modulates the arm length, while $\mathcal{R} < 1$ reduces the electric field amplitude. We write the electric field in the membrane arm as $\vec{E}_2 = \sqrt{\mathcal{R}}\vec{E}_0 e^{i(\Omega_L t + 2kL_2 + 2k\delta u(t))}/\sqrt{2}$. We refer to the beam on the membrane arm as the probe beam (PB) and to the one on the mirror arm as the local oscillator (LO). The interference beam is described by Eq. (2.1), but in this case the path difference is modulated by the membrane motion $\Delta L + \delta u(t)$.

The membrane motion is transduced into a phase modulation of the PB. On the detected field, the phase modulation information is contained only in the interference term. Since the only information we are interested in is the membrane displacement which is mapped in the phase modulation, we can get rid of the constant contribution of the intensity field in Eq. (2.1). To remove it we can use the so-called balanced homodyne detection scheme. An easy way to realize it is through a different interferometer geometry, the so-called Mach-Zehnder interferometer. A conceptual sketch with one of the mirror replaced with a membrane is reported in Fig. 2.2 (a). In this configuration, the intensities in front of the two detectors are:

$$I_+ = \frac{I_0}{4}(\mathcal{R}+1) + \sqrt{\mathcal{R}}\frac{I_0}{2}\cos(k\Delta L + 2k\delta u(t)), \tag{2.3a}$$

$$I_- = \frac{I_0}{4}(\mathcal{R}+1) - \sqrt{\mathcal{R}}\frac{I_0}{2}\cos(k\Delta L + 2k\delta u(t)). \tag{2.3b}$$

The two light intensities are then converted into two photocurrents, $\mathcal{I}_+$ and $\mathcal{I}_-$, and they are subtracted. Assuming to have two photodetectors with identical responsivity R_λ, the resulting photocurrent after the subtraction is

$$\mathcal{I} = R_\lambda(I_+ - I_-) = R_\lambda\sqrt{\mathcal{R}}I_0\cos(k\Delta L + 2k\delta u(t)). \tag{2.4}$$

From the discussion presented in 1.2.3, we know the membrane displacement can be described by a set of mechanical modes vibrating with harmonic motion $A\sin(\Omega_i t)$, where A is the displacement amplitude and defines the strength of the phase modulation generated by given mode. We only focus on one mode at the time. Varying the arm length difference ΔL we can modify how the phase modulation affects the photocurrent.

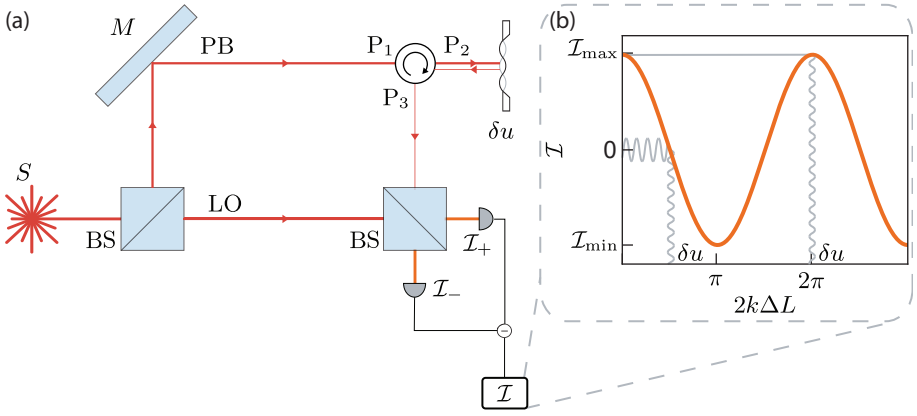

Figure 2.2: Balanced homodyne detection. (a) Scheme of a Mach-Zehnder interferometer with a balanced homodyne detection where one of the mirror has been replaced with a membrane. S =laser source, BS $= 50:50$ beam splitter, M = mirror, LO =local oscillator, PB = probe beam, δu = membrane displacement, P_i = i-th port of a circulator. $\mathcal{I}$ = photocurrent.(b) Photocurrent after the subtraction (orange line). The grey lines represent the transduction of a small modulation around the two positions $k\Delta L = (2n+1)\pi/2$ and $k\Delta L = n\pi$, with ΔL the path difference between the LO and the PB arm. In the former case the small phase modulation is linearly transduced into a modulation of the intensity, in the latter the small modulation does not affect the value of the intensity.

We now describe the two limiting cases where the effect of the phase modulation on the photocurrent is zero and maximum. Before moving forward we recall the properties of the Bessel functions [Arf85]

$$\cos(x\sin\phi) = J_0(\xi) + 2\sum_{m=1}^{\infty} J_{2m}(\xi)\cos(2m\phi)) \tag{2.5a}$$

$$\sin(x\sin\phi) = 2\sum_{m=1}^{\infty} J_{2m-1}(\xi)\sin((2m-1)\phi) \tag{2.5b}$$

We first consider the case $k\Delta L = 0$ and $2kA \ll 1$. We can express the phase modulation $\cos(2k\delta u(t))$ in terms of Bessel functions J_m using Eq. (2.5a), with $x = 2kA$ and $\phi = \Omega_i t$. In the limit of small modulations the zeroth order Bessel function is the dominant contribution of the expansion, therefore we can write

$$\begin{aligned}\mathcal{I} &= R_\lambda\sqrt{\mathcal{R}}I_0\cos(2kA\sin(\Omega_i t)) = R_\lambda\sqrt{\mathcal{R}}I_0 J_0(2kA)\\ &\underset{2kA\ll 1}{\approx} R_\lambda\sqrt{\mathcal{R}}I_0,\end{aligned} \tag{2.6}$$

where in the last step we performed the approximation $J_0(2kA) \approx 1$. From the equation above we immediately understand that the phase modulation does not affect the photocurrent. A visual example is represented by the grey modulation centered around the maximum point in

Fig. 2.2 (b), which is transduced in a constant intensity signal. We get the same result for all the maxima and minima, i. e. $k\Delta L = n\pi$ with n an integer number.

Let us now consider the case $k\Delta L = \pi/2$ and $2kA \ll 1$. In this case we can apply the property of the Bessel functions in Eq. (2.5b). For small modulations the dominant term coincides with the first term in the expansion, hence we write

$$\begin{aligned}\mathcal{I} &= R_\lambda\sqrt{\mathcal{R}}I_0\sin(2kA\sin(\Omega_i t)) = 2R_\lambda\sqrt{\mathcal{R}}I_0 J_1(2kA)\sin(\Omega_i t)\\ &\underset{2kA\ll 1}{\approx} 2R_\lambda\sqrt{\mathcal{R}}I_0 kA\sin(\Omega_i t),\end{aligned} \tag{2.7}$$

where in the last step we performed the approximation $J_1(2kA) \approx kA$. Within these conditions, the photocurrent is proportional to the membrane displacement amplitude and is amplified by the light intensity, a visual representation of the amplified transduction is showed in Fig. 2.2 (b) in the modulation around $k\Delta L = \pi/2$. We obtain the same result for all the odd multiples of $\pi/2$. If we analyze the signal in the frequency domain, the mechanical displacement appears as a peak centered at Ω_i in the PSD. In the measured signal we have an additional contribution to the height of the peak due to the interference term $R_\lambda\sqrt{\mathcal{R}}I_0$.

In the above discussion we assumed the path difference to be constant in time. Mechanical vibrations, thermal drifts or other noise sources might induce a variation in the arm length difference ΔL, modifying our position in the interference fringes. These drifts are normally produced by slow sources ($< 2\,\mathrm{kHz}$) while the phase modulations generated by the bandgap modes is happening at MHz frequencies. In an interferometer with a homodyne detection scheme, the path difference can be actively stabilized at the desired value by varying the length of the LO arm. We refer to such active stabilization as homodyne lock.

2.3 HETERODYNE DETECTION SCHEME

The heterodyne detection scheme differs from the homodyne detection scheme because the LO and the PB are characterized by two different frequencies.[2] It is usually realized by introducing a frequency shift in the LO arm. The resulting electric fields before recombining them on the last BS of a Mach-Zehnder interferometer are

$$\vec{E}_{\mathrm{LO}} = \vec{E}_0/\sqrt{2}e^{i((\Omega_\mathrm{L}+\Omega_\mathrm{C})t+kL_1)}, \tag{2.8a}$$

$$\vec{E}_{\mathrm{PB}} = -\sqrt{\mathcal{R}}\vec{E}_0/\sqrt{2}e^{i(\Omega_\mathrm{L}t+kL_2+2k\delta u(t))}, \tag{2.8b}$$

where Ω_C is the frequency offset of the LO. We refer to Ω_C as the carrier or the carrier beat note frequency interchangeably. The resulting photocurrent can be written as

$$\mathcal{I} = R_\lambda\sqrt{\mathcal{R}}I_0\cos(\Omega_\mathrm{C}t + k\Delta L + 2k\delta u(t)). \tag{2.9}$$

2 Again from greek '*héteros*'=different

As in the homodyne case, the membrane motion is transduced into a phase modulation of the signal. In contrast with the homodyne, the heterodyne signal has an oscillating component at the frequency of the carrier modulation. The presence of the frequency offset does not allow us to measure the phase modulation and the photocurrent intensity separately by simply fixing ΔL. For now we consider $k\Delta L$ as a constant term, while we write again $\delta u(t)$ as an oscillating term. The resulting signal in the time domain is a curve oscillating at the carrier frequency Ω_C which expands and compresses at a rate defined by the phase modulation frequency Ω_i, see Fig. 2.3 (a). To understand the contribution of the carrier frequency shift and of the phase modulation, it is instructive applying the properties of the trigonometric functions to separate the different terms in the cosine

$$\begin{aligned}\mathcal{I} =& R_\lambda \sqrt{\mathcal{R}} I_0 [\cos(\Omega_C t + k\Delta L)\cos(2kA\sin(\Omega_i t)) + \\ & - \sin(\Omega_C t + k\Delta L)\sin(2kA\sin(\Omega_i t))],\end{aligned} \tag{2.10}$$

where we wrote explicitly $\delta u(t)$ as a sinusoidal function. We can use again the properties in Eq. (2.5a) and (2.5b). Keeping only the first term of the expansions and after some mathematical manipulation, Eq. (2.10) reduces to

$$\begin{aligned}\mathcal{I} =& R_\lambda \sqrt{\mathcal{R}} I_0 [J_0(kA)\cos(\Omega_C t + k\Delta L) + \\ & + 2J_1(2kA)\cos((\Omega_C + \Omega_i)t + k\Delta L) + \\ & - 2J_1(2kA)\cos((\Omega_C - \Omega_i)t + k\Delta L)].\end{aligned} \tag{2.11}$$

If we analye it in the frequency domain, the mechanical modulation will appear as two sideband peaks with frequencies $\Omega_C \pm \Omega_i$ around a carrier peak centered at Ω_C, see Fig. 2.3 (b).

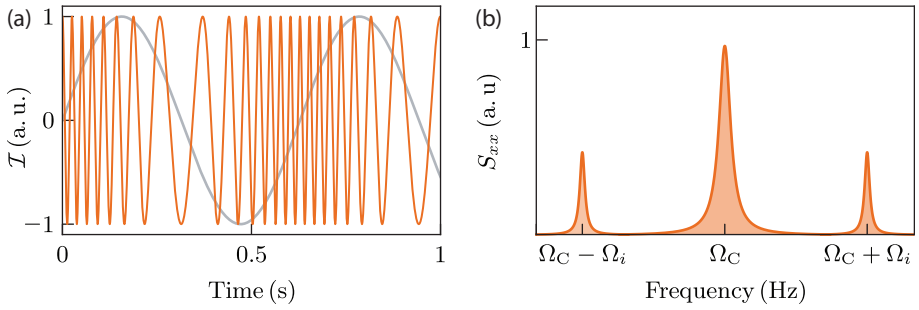

Figure 2.3: Heterodyne signal. (a) Example of a heterodyne signal in the time domain. The orange line is the phase modulated signal, the grey line is the phase modulation introducing an expansion and compression of the oscillation on the orange line. (b) Heterodyne signal in the frequency domain. The spectrum of the phase modulated signal is formed by a central peak at the carrier frequency and two sideband peaks generated by the mechanical phase modulation.

Notably the interferometer arm difference ΔL constitutes a common phase term in all the frequency components. By measuring the phase

the carrier frequency component and of the mechanical sidebands simultaneously, we can use the phase information of the former to cancel the phase drifts on the mechanical sidebands. This approach is the equivalent of stabilizing the interferometer phase. The absence of an active stabilization, replaced by a noise cancellation performed in post processing, is one of the main advantages of the heterodyne with respect the homodyne detection scheme. Moreover, the three frequencies carry the information related to both the situation $k\Delta L = 0$ and $k\Delta L = \pi/2$ which we can access simultaneously.

2.4 NOISE SOURCES

In the above, we only talked about the signal produced by the membrane motion without considering any type of noise beside the interferometer phase drifts. In a real experiment, we always have additional noise sources introducing noise terms $\delta\mathcal{I}$ in the photocurrent. We distinguish between three noise sources: *electronic noise*, *classical noise* and *shot noise*. In the following we give a description of these three sources. Notice that this three source of noise are uncorrelated with each other.

2.4.1 *Electronic noise*

The electronic noise is a source of noise added to the signal by all the electronic components of the setup, such as photodetectors, oscilloscopes, power supplies, lock-in amplifiers etc. We can have many types of electronic noise; thermal noise of resistive elements [KK80] and the flicker noise [Bah08] are two examples of those. Accordingly with the specific source, it can show a frequency dependence but it is not affected by the laser power. Therefore, the PSD of the electronic noise (S_{el}) at a given frequency is constant as a function of laser power. This independence from the laser power makes it detectable also when there is no light impinging the photodetectors. In our system we are not applying any technique to reduce or optimize the electronic noise, although we ensure to use electronic components introducing a sufficiently small amount of noise. However, once all the instruments are connected and turned on, we consider the electronic noise as a constant background. We can include the electronic noise in the photocurrent as an extra term $\delta\mathcal{I}_{\mathrm{el}}$ completely independent from the optical power.

2.4.2 *Classical noise*

We classify the noise sources associated with imperfections of the laser as classical noise. We can distinguish between *Intensity noise* and *Phase noise* of the laser.

The intensity noise is introduced by fluctuations in the optical power emitted by the laser. There are several mechanisms associated with this noise such as relaxation oscillations, vibrations of the laser cavity mirrors or imperfections in the pump medium, to mention only a few examples [ME10]. We can include the intensity noise contribution as a random fluctuation δP around an average emitted power $\bar{P}$. Therefore, the laser intensity presents random fluctuations around an average value, that we can write as $\bar{I}_0 + \delta I_0$. Such random fluctuations are frequency-dependent and they are usually more pronounced around the relaxation oscillation frequency [ME10]. Additionally, the intensity noise is proportional to the average laser power emitted [Fox06]. To measure the amount of intensity noise in our laser source, we can detect directly the laser light on a photodiode and analyze the signal in the frequency domain by varying the emitted power. The expected PSD for the intensity noise is characterized by a dependence which goes with P^2 [Fox06].

To understand the intensity noise contribution on the interference signal, we substitute I_0 with $\bar{I}_0 + \delta I_0$ in Eqs. (2.3). We simplify the discussion by substituting the membrane with a perfectly reflective and static mirror. The two photocurrents before the subtraction become

$$\mathcal{I}_+ = R_\lambda \frac{(\bar{I}_0 + \delta I_0)}{2} + R_\lambda \frac{(\bar{I}_0 + \delta I_0)}{2} \cos(k\Delta L), \tag{2.12a}$$

$$\mathcal{I}_- = R_\lambda \frac{(\bar{I}_0 + \delta I_0)}{2} - R_\lambda \frac{(\bar{I}_0 + \delta I_0)}{2} \cos(k\Delta L). \tag{2.12b}$$

The intensity fluctuations generated in the the by the intensity noise fluctuations are common in the two equations above. Thus, by implementing a balanced detection we can cancel out the contribution of the intensity noise to the first components of the above photocurrents. Moreover, actively stabilizing the interferometer arm lengths at $k\Delta L = \pi/2$ removes the noise contribution in the interference term. By including the phase modulation of the membrane and locking the interferometer arm difference at $k\Delta L = \pi/2$, we get the photocurrent

$$\mathcal{I} = 2R_\lambda \mathcal{R} \bar{I}_0 \delta u + 2R_\lambda \mathcal{R} \delta I_0 \delta u. \tag{2.13}$$

As long as the condition $\bar{I}_0 \gg \delta I_0$ is satisfied, the second term on the right hand side is negligible.

The second type of classical noise we discuss is the laser phase noise. It is generated by phase fluctuations of the laser beam due to, for instance, spontaneous emission [ME10]. We can describe the fluctuations as $\bar{\varphi}_\mathrm{L} + \delta\varphi_\mathrm{L}(t)$, where $\delta\varphi_\mathrm{L}(t)$ is the random phase fluctuations we get at the emission time t. In contrast with the intensity noise, we can measure phase noise only by interfering photons generated at different times. To understand the phase noise contribution it is instructive to write the electric field emitted by the laser by adding the fluctuating phase. We include this extra term in Eqs. (2.3) assuming $\mathcal{R} = 1$ and $\delta(u) = 0$.

Within these conditions, the two photocurrents before the subtraction are

$$\mathcal{I}_+ = R_\lambda \frac{I_0}{2} + R_\lambda \frac{I_0}{2} \cos(k\Delta L + \delta\varphi(t_2) - \delta\varphi(t_1)), \tag{2.14a}$$

$$\mathcal{I}_- = R_\lambda \frac{I_0}{2} - R_\lambda \frac{I_0}{2} \cos(k\Delta L + \delta\varphi(t_2) - \delta\varphi(t_2)). \tag{2.14b}$$

The delay time t_i coincides with $t_i = L_i/c$, with c the speed of light, and it represents the time the electric field E_i needs to travel the distance L_i. The balance detection cannot cancel the phase noise contribution. However, if the arm lengths are balanced the phase noise is negligible.

2.4.3 *Shot noise*

The last type of noise we discuss is the shot noise, sometimes called quantum noise because it originates from the discrete nature of the measured quantity, in particular photons and photoelectrons. In the limit of high intensity beam, the photons' arrival time at the photodetector can be described as a random process following a Poissonian distribution [ME10]. Such randomness results in a time-dependent number of photons arriving at the detector

$$N_{\mathrm{ph}}(t) = \bar{N}_{\mathrm{ph}} + \delta N_{\mathrm{ph}}, \tag{2.15}$$

where $\bar{N}_{\mathrm{ph}}$ is the average number of photons and δN_{ph} represents the fluctuations around that value. Therefore, the intensity of the light can be written as an average value $\bar{I}_0$ plus a fluctuating term δI_{sn}. The generated photocurrent is then equal to

$$\mathcal{I} = R_\lambda(\bar{I}_0 + \delta I_{\mathrm{sn}}). \tag{2.16}$$

To evaluate the PSD of the shot noise component of the photocurrent we need to evaluate the following integral

$$S_{\mathrm{sn}} = R_\lambda^2 \int_{-\infty}^{+\infty} \langle \delta I_{\mathrm{sn}}(t) \delta I_{\mathrm{sn}}(t+\tau) \rangle e^{-i\Omega t} dt \tag{2.17}$$

The shot noise is a white noise source characterized by a Poissonian distribution, hence the variance of the number of photon is $\langle \delta N_{\mathrm{ph}}^2 \rangle = \bar{N}_{\mathrm{ph}}$ [ME10]. Thus the fluctuations of the photocurrent also follow the same statistic [Fox06]. The resulting PSD is then equal to:

$$S_{\mathrm{sn}} = R_\lambda^2 \bar{I}_0. \tag{2.18}$$

As expected by definition of white noise, the PSD of the shot noise is frequency independent. In contrast with the classical noises, neither the balance detection nor balancing the arm length can remove the shot noise from the signal due to its uncorrelated nature.

2.4.4 *Optimal signal-to-noise ratio*

We now discuss the optimal noise condition to perform our experiments. As already highlighted, we can remove the classical noises through a balance homodyne detection scheme and balancing the length of the interferometer arms. To understand the contribution of the two remaining noise sources, it is instructive to understand how the laser power affect the total PSD. Neglecting the classical noise, the total PSD has three contributions [Fox06]

$$S_{\text{tot}} = S_{\mathcal{I}} + S_{\text{sn}} + S_{\text{el}}, \tag{2.19}$$

where $S_{\mathcal{I}}$ is the PSD generated by the interference signal, S_{sn} is the PSD of the shot noise and S_{el} is the PSD of the electronic noise. S_{el} does not depend on the optical power. The shot noise is characterized by a linear dependence on the optical power, $S_{\text{sn}} \propto \mathcal{I} \propto I_0 \propto P$. Finally, the interference signal depends quadratically on the optical power $S_{\mathcal{I}} \propto I_0^2 \propto P^2$. The first (trivial) requirement is to choose an optical power such that the signal is larger than both the noise contributions. This condition can coincide with both the following situations: $S_{\text{sn}} < S_{\text{el}} < S_{\mathcal{I}}$ and $S_{\text{el}} < S_{\text{sn}} < S_{\mathcal{I}}$. At a first look we could think that the first condition is optimal, since it is the one characterized by the smaller amount of noise. However, such situation does not coincide with the best signal-to-noise ratio. In Fig. 2.4 we show the three PSDs as a function of laser power. Comparing the noise PSDs with the signal PSD,

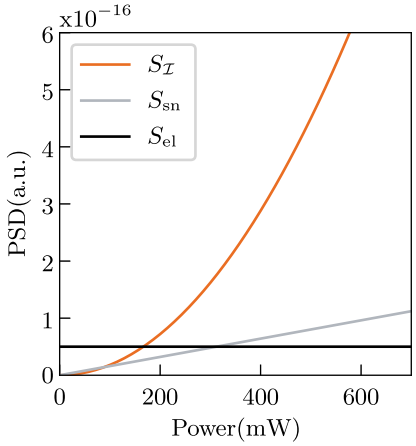

Figure 2.4: PSDs of the noise contributions compared with the PSD of the interference signal. The orange line is the interference signal, the grey line is the shot noise, the black line is the electronic noise.

we recognize that the best signal-to-noise-ratio corresponds to the shot noise as a dominant noise source in the system. One could be tempted to use as much power as possible. That could lead to saturation of the photodetectors and a contribution of the classical noises too large to be corrected.

3

EXPERIMENTAL TECHNIQUES

In this chapter we discuss all the experimental techniques and procedures we apply within this thesis work. We start describing the experimental setup we use to detect the membrane displacement and illustrating the different configurations we can choose. We give an introduction to the working principle of the lock-in amplifier, the main instrument we employ in all the measurement protocols, and we describe the two main calibration techniques we adopt to map from measured voltages to membrane displacement. In the second half of the chapter we present how the largest displacement can introduce a nonlinear optical transduction and how we can remove such effect from our data when needed. Moreover, we show how we can extract the instantaneous frequency shift from the phase information. Finally, we show the presence of unwanted thermal frequency drifts and three different techniques we use to mitigate them.

3.1 EXPERIMENTAL SETUP

The optical setup used to measure the membrane displacement is shown in Fig. 3.1 (a). It consists of a fiber-based Mach-Zehnder interferometer. The membrane motion is mapped into a phase modulation of one the PB by varying the arm-length. A good visibility is guaranteed by the use of single mode polarization maintaining (PM) fibers. The only two non-PM fiber components are the fiber polarization controller and the input of the first polarizing beam splitter (PBS). The laser source is a fiber-based Koheras Basik E15 laser, from NKT photonics, with a wavelength of 1545 nm. The use of fibers reduces the alignment time, and it gives us the possibility of changing or adding optical components in the interferometer arms without loosing the alignment. In particular, we can switch between two different LO configurations. In the first configuration (Fig. 3.1 (b)) the light travels through an acousto-optic modulator (AOM) introducing a 40 MHz frequency shift in the LO arm. In the second configuration (Fig. 3.1 (c)) the light travels through a fiber stretcher that we can use to adjust the path length. Therefore, we can choose between a heterodyne and a homodyne detection depending on the experimental requirements.

The only free space optics part of the setup is in the PB arm. Here the output light from the port 2 of the fiber circulator is collimated and focused on the membrane with an expected waist of $\approx 20\,\mu$m. The fiber collimator is mounted on a movable stage outside the vacuum chamber. We refer to the movable free space optical components as the probe head. In everyday operation, we load multiple membranes into the

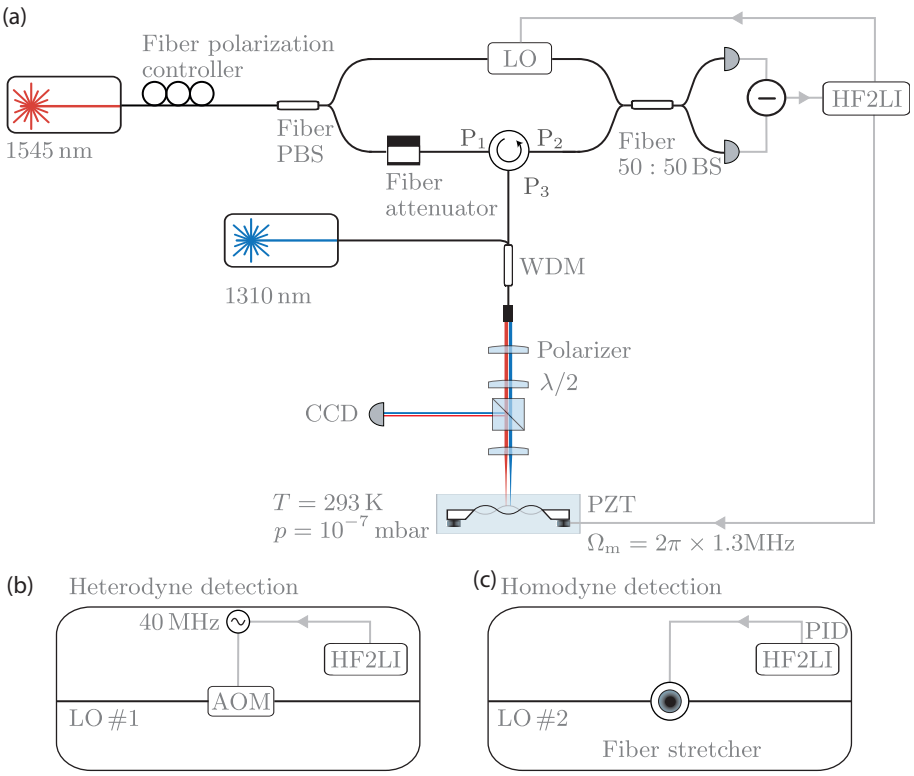

Figure 3.1: Experimental setup. (a) Scheme of the experimental setup. PBS = polarizing beam splitter, AOM = acoustooptic modulator, BS = beam splitter, WDM = wavelegnth division multiplexer, $\lambda/2$= half wave plate, PZT = piezoelectric actuator, P_i = circulator port number, LO = local oscillator. The membrane is placed in a vacuum chamber at room temperature. Black lines represent fiber connections, grey lines the electrical connections, red and blue lines the optical paths. By switching two fiber connections, we can change the optical components on the LO path in order to move from a heterodyne (b) to a homodyne (c) detection scheme.

vacuum chamber, which we can then probe and characterize by moving the probe head on different positions without breaking the vacuum. The probe head is equipped with a polarizer and a half-wave plate to optimize the coupling of the reflected light into the fiber collimator. The membrane vibrations modify the length of one interferometer arm and are translated into a phase modulation of the interference field as described in Chapter 2. In contrast with the simplified treatment performed in the previous chapter, the membrane vibrations features several vibrational modes with different spatial profiles, which can be distinguished analyzing the interference signal in the frequency domain.

The SiN membrane is characterized by a side length of few mm but the mode of interest is strongly confined in a central region with a diameter of $60 - 200\,\mu$m, see sec. 1.3.3 and 1.3.4 for more details on the membrane designs. Therefore we need to align our beam spot in the

region of interest. We use a torch light and a CCD camera to image the membrane. A second laser beam at 1310 nm is introduced in the system to monitor the beam spot position, given that the 1545 nm laser light is not visible on the CCD camera. We ensure a good spatial overlap between the two lasers by sending them through the same optical path. The mechanical actuation is realized through a piezo actuator clamped below the membrane. Alternatively, the membrane can be actuated through radiation pressure force by modulating the intensity of the 1310 nm beam. For the experiments presented in this thesis we need a driving strength too large to be provided by the optical excitation. In the experiments discussed in the next chapters we always use the piezo actuation.

The DC and the RF components of the photocurrent are separated by a bias tee circuit. The DC part is only relevant in the homodyne case. We send both the DC and the RF part to a HF2 lock-in amplifier (HF2LI) from Zürich Instruments. Using the HF2LI output we can extract the amplitude and the phase information of a mechanical mode from the RF signal. The DC component is fed into a proportional–integral–derivative controller (PID) integrated to the HF2LI. The output of the PID is used to lock the LO arm length. The HF2LI is used to read and generate all the signals within the setup, e. g. the 40 MHz AOM driving voltage and the piezo driving tones. The only additional instrument used is an oscilloscope to monitor the intensities of the LO arm and of the PB after the membrane reflection.

3.2 PRINCIPLE OF LOCK-IN DETECTION

A lock-in amplifier is a device capable of extracting the amplitude (A) and the phase (φ) information of a periodic signal of known frequency in a noisy environment [Hf2]. A scheme of the working principle is represented in Fig. 3.2. Let us analyze the working principle by considering

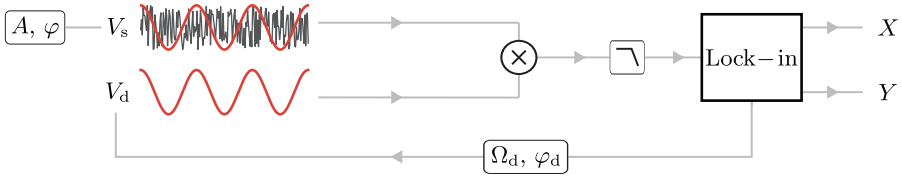

Figure 3.2: Scheme of the working principle of a lock-in amplifier. V_s = measurement signal, V_d = demodulation signal, A = measurement signal amplitude, φ = measurement signal phase, Ω_d =demodulation signal frequency, φ_d = demodulation signal phase, X = amplitude electronic quadrature, Y = phase electronic quadrature.

a measurement signal (V_s) with a given amplitude A, oscillating at frequency Ω_s, and characterized by a phase φ:

$$V_\mathrm{s} = A\cos(\Omega_\mathrm{s} t + \varphi). \tag{3.1}$$

We generate a reference signal (V_d), that we call demodulation signal, with fixed amplitude $1/\sqrt{2}$, a controllable phase and oscillating at a frequency Ω_d:

$$V_\mathrm{d} = \sqrt{2}e^{-i\Omega_\mathrm{d}t}. \tag{3.2}$$

We usually set the demodulation phase to zero. In our setup the demodulation signal is generated within the lock-in amplifier itself. Then we mix the measurement with the demodulation signal. The resulting mixed signal takes the form

$$\begin{aligned} z(t) &= V_\mathrm{s} \times V_\mathrm{d} \\ &= \frac{A}{\sqrt{2}}\left[e^{-i((\Omega_\mathrm{s}+\Omega_\mathrm{d})t+\varphi)} + e^{i((\Omega_\mathrm{s}-\Omega_\mathrm{d})t+\varphi)}\right]. \end{aligned} \tag{3.3}$$

After the mixing, we apply a low pass filter $H(t)$ to remove the fast oscillating components

$$\begin{aligned} H(t) * z(t) &= \frac{A}{\sqrt{2}}e^{i((\Omega_\mathrm{s}-\Omega_\mathrm{d})t+\varphi)} \\ &= \frac{A}{\sqrt{2}}\cos((\Omega_\mathrm{s}-\Omega_\mathrm{d})t+\varphi) + i\frac{A}{\sqrt{2}}\sin((\Omega_\mathrm{s}-\Omega_\mathrm{d})t+\varphi), \end{aligned} \tag{3.4}$$

where $*$ represents the convolution operator. To extract the information relative to the signal of interest, we choose a demodulation frequency $\Omega_\mathrm{d} = \Omega_\mathrm{s}$. Within this condition the demodulated signal represented by Eq. (3.4) becomes

$$H(t) * z(t) = \frac{A}{\sqrt{2}}e^{i\varphi} = X + iY, \tag{3.5}$$

where X and Y are the electronic quadratures, also called amplitude and the phase electronic quadrature respectively. A lock-in amplifier outputs the two electronic quadratures from the final filtered signal. We can convert those into amplitude and phase information through the relations

$$\frac{A}{\sqrt{2}} = \sqrt{X^2+Y^2}, \tag{3.6a}$$

$$\varphi = \arctan\frac{Y}{X}. \tag{3.6b}$$

Notice that the extracted displacement amplitude at the output is in units of $\mathrm{V_{rms}}$.

3.3 CALIBRATION

In Chapter 1 we discuss how we model the motion of a thin membrane linking its motion to the dynamics of a damped harmonic oscillator. In

Chapter 2 we describe how the membrane motion generates a phase modulation in an interference signal and how we can convert it into a measurable signal. Finally in Sec. 3.2 we show how we can extract the amplitude and the phase information from the generated signal at the frequency of interest. The last piece of information we need is how we can convert the measured displacement amplitude, expressed in V (or V_{rms} in our case), in real displacement amplitude expressed in m. Therefore, we need to define a calibration procedure to realize such conversion.

In this thesis we use two types of calibration. Accordingly with the type of information we want to extract, we apply one or the other. We call them *absolute displacement calibration* and *relative displacement calibration*. In the following subsections we describe the derivation and the limits of both methods.

3.3.1 *Absolute displacement calibration*

We named this calibration absolute displacement calibration because it always returns the displacement amplitude at the maximum displacement point, no matter where we place our beam spot on the modeshape profile. To derive the calibration constant through this procedure, we start from the PSD of a membrane resonator in its thermal equilibrium. From Eq. (1.38) we know that the area under the signal PSD coincides with its variance. Substituting Eq. (1.36) in Eq. (1.38) and using the Langevin force PSD, defined in Eq. (1.37) as S_{FF}, we find that [Sch09] the variance of a normalized mode in its thermal equilibrium is

$$\langle u^2 \rangle = \frac{k_B T}{m_i \Omega_i^2}. \tag{3.7}$$

Notice that to evaluate the variance we need to integrate the mechanical susceptibility over all the frequencies, therefore we cannot perform the approximation in Eq. (1.32). We refer to Eq. (3.7) as thermal area (A_{th}) and is expressed in unit of m^2. On the other hand, we can estimate the variance evaluating the area under the measured PSD. We refer to the latter as the measured area A_{meas} and is expressed in units of V_{rms}^2. The two areas are related through the following

$$A_{meas} = g^2 A_{th}, \tag{3.8}$$

where g is a conversion factor expressed in unit of V_{rms}^2/m^2. From Eq. (3.8) we recognize that the conversion factor can be written as the ratio between the measured and the thermal area and could be used as a calibration constant. By writing it explicitly the conversion factor squared

$$g^2 = \frac{A_{meas} m_i \Omega_i^2}{k_B T} \tag{3.9}$$

we observe that all the terms on the right hand side can be determined either experimentally or with simulations. k_B is the Boltzmann constant, T is the ambient temperature, A_{meas} can be numerically evaluated from the measured PSD, Ω_i can be evaluated from the peak position of the measured PSD, while m_i can be simulated through FEM simulations using Eq. (1.22). Since the effective mass is simulated using the normalized mode with the convention $\phi_i^{max} = 1$, the calibration constant evaluated through this procedure returns the displacement we expect to measure at the point of maximum displacement and not the one at the laser spot, unless the laser spot is align with the maximum displacement point.

We now describe the calibration protocol. To extract $\langle u_i^2 \rangle$, we choose a demodulator frequency $\Omega_d \approx \Omega_i$ and we save the two electronic quadratures X and Y for ≈ 2 min. Then, we perform the discrete Fourier transform (FFT) [PM06]. From the computed spectrum we extract the resonance frequency of the mode of interest and compute the numerical area under the thermal peak after subtracting the background noise. Finally, we evaluate the calibration constant through Eq. (3.9). A new calibration constant is measured before each set of measurements. The amount of light reflected from the membrane can change because of polarization drifts or other fluctuations in the beam spot position due to mechanical instabilities. In the heterodyne detection scheme, we use the carrier beat note information to correct for such fluctuations . The height of both the sideband peaks and of the carrier beat note increases and decreases in the same way with the intensity of the reflected light. By measuring the amplitude of the carrier beat node demodulating the signal at $\Omega_d = \Omega_c$, we can use the ratio between the height of the carrier beat note saved during the calibration process and the one saved during the measurement as a correction factor for light intensity fluctuations. In the homodyne detection scheme the same procedure could be applied by introducing a modulation on the fiber stretcher. Unfortunately in the current homodyne setup we are not able to include such modulation because of electronics limitation.

This calibration procedure relies on an accurate simulation of the effective mass. From the modeshape measurement realized in [Bar+16] we are confident that the simulated effective mass is accurate. This calibration procedure cannot be used on the measurements where the effective mass is an unknown which needs to be estimated from the calibrated spectrum, or when the simulated effective mass is uncertain.

3.3.2 *Relative displacement calibration*

We now describe a second calibration procedure which does not require prior knowledge of the effective mass. We implement this type of calibration only with the heterodyne detection scheme, hence we give a description of the protocol only in this experimental configuration. A

similar calibration procedure for the homodyne detection scheme is described in [Bar14].

In the heterodyne detection scheme, the brownian motion of the membrane displacement is transduced in two mechanical sidebands at the frequencies $\Omega_C \pm \Omega_i$ in the heterodyne signal (see Sec. 2.3), with Ω_C the frequency of the carrier beat note. As we can see in Eq. (2.11), the displacement amplitude relative to the sideband peaks is proportional to the Bessel function of the first order $J_1(\xi)$, where ξ is the modulation depth and it is proportional to the membrane displacement. To perform the calibration we need to relate the measured sideband spectrum (S_{VV}) with the phase modulation realized by the membrane motion. First we extract the modulation depth by comparing the area under the sideband peak and the carrier beat note which satisfy the relation [Hf2]

$$\left|\frac{J_0(\xi)}{J_1(\xi)}\right|^2 = \frac{\int S_{\mathrm{VV}_{\mathrm{car}}} \frac{\mathrm{d}\Omega}{2\pi}}{\int S_{\mathrm{VV}_{\mathrm{mech}}} \frac{\mathrm{d}\Omega}{2\pi}}. \tag{3.10}$$

Knowing the modulation depth, we can express the area under the peak calibrated in radians ($A_{\varphi\varphi}$) using the first order Bessel function

$$A_{\varphi\varphi} = \frac{|J_1(\xi)|^2}{2} \approx \frac{\xi^2}{2}. \tag{3.11}$$

The last approximation is true in the limit of small phase modulation and we included a factor 2 to account for rms ampliudes. Similarly to the absolute calibration procedure, we say that $A_{\varphi\varphi}$ is related with the measured area through by the equality

$$A_{\varphi\varphi} = cA_{\mathrm{meas}}, \tag{3.12}$$

where c is a conversion factor expressed in $\mathrm{rad}^2/\mathrm{V}^2$. A_{meas} is the numerical area of one measured sideband peak. The conversion factor c is the ratio between the two evaluated areas, hence we can map V^2 to rad^2 through the following transformation:

$$S_{\varphi\varphi} = cS_{\mathrm{VV}} = \frac{\xi^2}{2A_{\mathrm{meas}}} S_{\mathrm{VV}}. \tag{3.13}$$

The last step is to convertrad^2 into m^2. From the discussion in Sec. 2.2 we know that the membrane displacement δu produces a phase modulation

$$\delta\varphi = 2k\delta u = \frac{4\pi}{\lambda}\delta u, \tag{3.14}$$

where λ is the laser wavelength. We can use the above relation to perform the last calibration step by writing

$$S_{uu} = \left(\frac{4\pi}{\lambda}\right)^2 S_{\varphi\varphi}. \tag{3.15}$$

We correct for fluctuations in light intensity following the same procedure described at the end of Sec. 3.3.1.

This calibration procedure is based on the extraction of the modulation depth at the measurement point. If our probe beam is not perfectly aligned with the maximum displacement point, or the optical beam profile is not perfectly gaussian or perfectly perpendicular with the mechanical modeshape, the measured displacement is smaller than the displacement at the maximum. In other words, this calibration procedure gives the maximum displacement point only if the overlap integral between the optical and the mechanical mode, i. e. the optomechanical coupling, is equal to one or if we can correct for it. In our experimental setup we do not have a way of measuring the overlap integral and the alignment procedure does not allow us to reach the required precision, hence we rarely perform this type of calibration.

3.4 CARRIER CORRECTION

In the above, we have always considered that the membrane displacement is linearly transduced into a phase modulation, i. e. the demodulated displacement signal is proportional to the amplitude. However, when we enter into the large displacement amplitude regime (Chapter 4) the phase modulation induced by the membrane motion is so large that a nonlinear transduction mechanism needs to be included. We discuss this situation in the heterodyne detection scheme, where we use the information contained in the carrier beat note to recognize the presence of such an effect and correct for it.

We start noticing that when $J_1(\xi)$ enters in the nonlinear region (mechanical modulation depth $\xi \approx 1$), $J_0(\xi)$ is not comparable to the unity anymore, solid lines in Fig. 3.3 (c). Therefore, in a ringdown measurement, where ξ varies in time because of the amplitude decay, a feature of the nonlinear transduction is the reduction of the carrier beat note amplitude at the beginning of the ringdown. After some time the modulation depth decays back to the linear regime and the carrier amplitude goes back to its constant value, Fig. 3.3 (a). There are two methods to apply a correction to the data and remove the effect of the nonlinear transduction.

In the first we start normalizing the carrier's amplitude to the value obtained in the linear regime ($|\bar{z}_{\mathrm{carr}}|$), i. e. at the end of the ringdown. This provides us with a measurement of the Bessel function of the zeroth order $|\bar{z}_{\mathrm{carr}}| = J_0(\xi)$, where $z_{\mathrm{carr}}(t)$ is the filtered time trace we obtain from the HF2LI with demodulation frequency $\Omega_{\mathrm{d}} = \Omega_{\mathrm{c}}$. We fit the time evolution of the carrier signal with the function $1 - be^{-t/\tau}$ (dashed line in Fig. 3.3 (a)). From that, we can invert the Bessel function to obtain the modulation depth $\xi = J_0^{-1}(|\bar{z}_{\mathrm{carr}}|)$. We use the modulation depth to find a correction factor

$$g_{\mathrm{corr}} = \frac{\xi/2}{J_1(\xi)}, \tag{3.16}$$

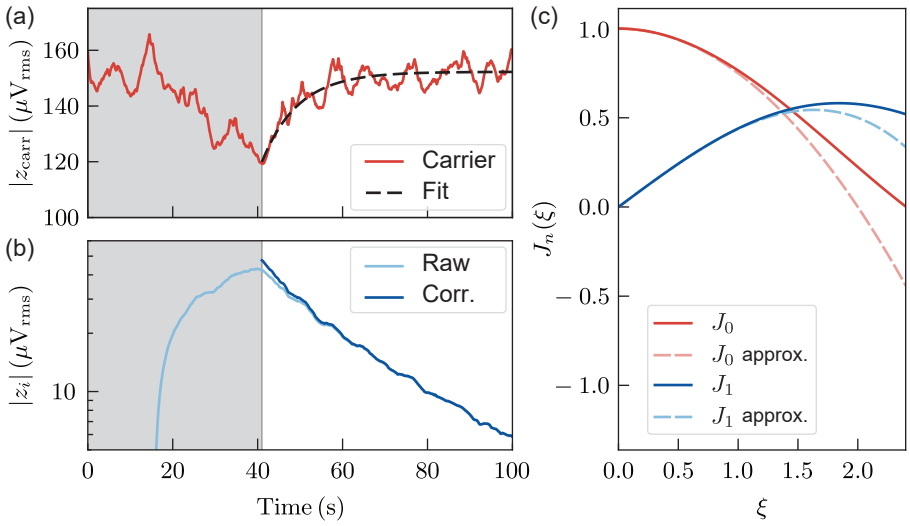

Figure 3.3: Correction for interferometer nonlinear transduction. (a) Reduction of the carrier amplitude due to the large modulation depth. The red line is the amplitude of the demodulated carrier signal. During the driving time (grey area) the modulation depth increases and the carrier amplitude reduces revealing the presence of a nonlinear transduction. During the ringdown time (white area) the carrier rings-up to the constant value characteristic of the linear transduction. The black dashed line is the exponential fit. (b) Amplitude of the demodulated mechanical sideband signal. The light blue line represents the raw data. The dark blue line represents the ringdown data when we add a correction factor to remove the nonlinear optical transduction effect. After the correction, we notice the presence of an excess nonlinear damping at the beginning of the ringdown. (c) Bessel functions against the modulation depth. The solid red (blue) line is the zeroth (first) order Bessel function. The dashed red (blue) line is the approximation to the third order of the zeroth (first) order Bessel function. In the regime we apply the correction ($\xi \leq 1$) the Bessel functions and the approximations are superimposed.

where $\xi/2$ corresponds to the linear approximation of the first order Bessel function. We remove the nonlinear transduction effect by multiplying the mechanical mode displacement amplitude by the correction factor g_{corr}. An example of ringdown with this correction is shown in Fig. 3.3 (b).

To derive the second method to perform the carrier correction, we start noticing that our experiments are always in the regime where $\xi \leq 1$. Within this condition the first two Bessel functions are always

positive and invertible. Moreover, they can be approximated by the expansion to the third order (dashed lines in Fig. 3.3 (c)),

$$J_0(\xi) = 1 - \left(\frac{\xi}{2}\right)^2 + o(\xi^4), \tag{3.17a}$$

$$J_1(\xi) = \frac{\xi}{2} - \frac{1}{2}\left(\frac{\xi}{2}\right)^3 + o(\xi^5) = \frac{\xi}{2}\sqrt{J_0(\xi)} + o(\xi^4), \tag{3.17b}$$

where in Eq. (3.17b) we performed the approximation

$$\sqrt{J_0(\xi)} \approx \sqrt{1-(\xi/2)^2} \approx 1 - (\xi/2)^2/2. \tag{3.18}$$

By using the relation between the first two Bessel functions in Eq. (3.17b) we can remove the nonlinear transduction effect using the following relation

$$|z_{i,\mathrm{corr}}| = \frac{|z_i|}{\sqrt{|\bar{z}_{\mathrm{carr}}|}}, \tag{3.19}$$

with z_i the filtered time trace we obtain from the HF2LI with demodulation frequency $\Omega_\mathrm{d} = \Omega_i$.

We find that the two methods produce data in excellent agreement with each other. In the data presented in this thesis we mostly use the first method. However, we recognize the advantages of the approximated one since it does not require any additional processing of the carrier data.

3.5 INSTANTANEOUS RESONANCE FREQUENCY SHIFT

We now describe another experimental technique we often use: the measurement of the instantaneous resonance frequency shift. It is relevant every time the resonance frequency of our membrane resonator can be described by a time-dependent shift $\Omega_i + \Delta\Omega_i(t)$. We can include the time-dependent frequency component in the photocurrent generated by the locked homodyne balanced detection by writing

$$\mathcal{I} = R_\lambda \sqrt{R}\frac{I_0}{2} J_1(A(t)) \sin((\Omega_i t + \Delta\varphi(t) + \varphi_0) \tag{3.20}$$

where $\partial_t \Delta\varphi(t) = \Delta\Omega_i(t)$. Feeding the photocurrent to the HF2LI and choosing $\Omega_\mathrm{d} = \Omega_i$, we can extract the phase information $\varphi(t) = \Delta\varphi(t) + \varphi_0$ through Eq. (3.6b). In the heterodyne detection case we obtain the same information choosing $\Omega_\mathrm{d} = \Omega_\mathrm{C} \pm \Omega_i$. Notice that the latter requires the additional step of measuring the interferometer phase drifts information performing a second demodulation at the frequency $\Omega_\mathrm{d} = \Omega_\mathrm{C}$ to remove phase fluctuations due to drifts in the interferometer arms-length. The measured carrier phase is then subtracted to the measured sideband phase. Finally we extract the instantaneous frequency shift $\Delta\Omega_i(t)$ by performing the numerical derivative of the measured phase $\Delta\varphi(t)$.

3.6 MITIGATING THERMAL FREQUENCY DRIFTS

The frequency stability of our system is limited. This is due to thermal drifts happening in the room, heating due to the piezo or other source of frequency noise. The rate at which the frequency drifts can vary with the sample, the time of the day, the voltage sent to the piezo, the mounting procedure, etc. An example of frequency drifts is shown in Fig. 3.4 (a) in the particular case of a 50 nm-thick Lotus membrane. In this particular measurement the membrane frame has been glued on a ring piezo. The radial expansion of the piezo applies an in-plane force stretching membrane mediated by the gluing process (see Chapter 6). The piezo introduces extra heating increasing the magnitude and the velocity of the thermal frequency drifts. The magnitude of the thermal drifts becomes relevant for all those measurements requiring to apply a perfectly resonant driving force for a time long enough that $\delta\Omega \approx \Gamma_i$. To

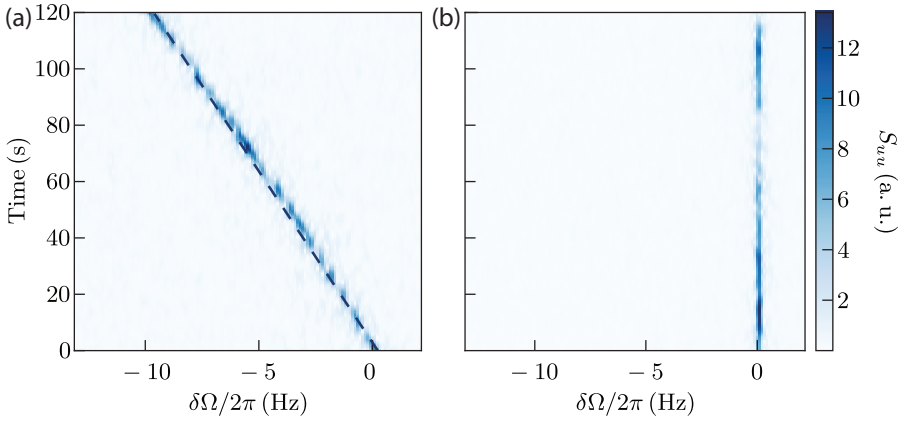

Figure 3.4: Thermal frequency drifts. (a) Thermal frequency drifts during 2 minutes measurement time. Each line is a spectrum performed with two averages. We perform a linear fit extracting the peak central frequencies from the maximum point of each spectrum. From the best fit (dashed line) we find that the thermal drift in this case is 5 Hz/min. (b) Frequency stability mitigating the thermal drifts.

reduce the impact of such drifts on our measurement we can either try to mitigate them, or we can reduce the sensitivity of our measurement protocol to frequency shifts increasing the mechanical linewidth. Often both the methods need to be applied simultaneously. In the rest of the section we describe both the approaches.

3.6.1 *Frequency stabilization*

The first method we describe is the frequency stabilization. It is based on the dependence of the resonance frequency from the in-plane stress. From Eq. (1.24) we observe that the resonance frequency squared depends on the pre-stress σ_0. By increasing or reducing the in-plane

stress we can increase or reduce the resonance frequency. To act on the in-plane stress we glue the membrane frame on a ring piezo in four points. Every time we apply a DC voltage to the piezo, the axial expansion generates a radial contraction and vice versa. Thanks to the gluing process, the radial expansion (contraction) of the piezo induces a stretching (relaxation) of the SiN membrane resulting in a variation of the resonance frequency. Although the maximum shift we get from the piezo is highly dependent on the gluing process, we always have a range large enough to counteract the amount of frequency drifts that the mode of interest experiences during the measurement time. Further details about the frequency shift induced by the gluing process are discussed in Chapter 6.

The stabilization procedure is realized in the following way. We drive resonantly a mode and by monitoring the measured phase on the HF2LI we identify the phase which corresponds to its resonant frequency. From Fig. 1.3 we know that the phase of a damped harmonic oscillator at resonance is $\pi/2$-shifted with respect to the driving force phase. Nevertheless, the measured resonant phase is often at a different angle due to phase delays introduced by cables or instruments response. The difference between the measured phase and the resonant phase defines an error signal which is fed into a PID controller. The voltage output of the PID controller is applied to the piezoelectric actuator. The resulting contraction (expansion) decreases (increases) the resonance frequency to counteract the thermal drifts. We generate the error signal with the PID option of the HF2LI. We perform this stabilization procedure on a mode, hereby defined as *thermometer mode*, which does not coincide with the mode of interest. This is based on the assumption that all the out-of-plane modes share the same dependence on thermal drifts and on the tensile stress. An example of the frequency stability reached by bandgap mode with the frequency stabilization applied on an out-of-bandgap thermometer mode is shown in Fig. 3.4 (b). Notice that this method can only be applied when the interferometer drifts are actively canceled. In our setup this condition is satisfied only in the homodyne configuration.

3.6.2 *Broadening the mechanical linewidth*

The frequency stabilization method described in the previous section is effective but often it does not provide sufficient protection against drifts during sensitive measurements, especially for localized bandgap modes. These modes are characterized by a linewidth of only few tens of mHz and the frequency stabilization would require a precision we are not able to reach. In these situations, we act on the linewidth of the mode of interest by broadening it to reduce the effects of the frequency drifts. We implement two methods to broaden the linewidth. The first one is based on the introduction of an additional gas damping source;

the second one is based on active feedback cooling of the mechanical mode.

In standard operating conditions, the membrane resonators are placed in a vacuum environment at a pressure of 10^{-7}mbar. At such a pressure, the contribution of gas damping is either negligible or very small (for thinner membranes). One method we can apply to broaden the mechanical linewidth consists in introducing additional damping, thereby increasing the gas damping contribution. This is something we can achieve by reducing the rotational speed of the turbo pump. We can estimate the amount of gas damping losses (Q_{gas}^{-1}) as as a function of pressure from Eq. (1.47). We characterize the quality factor of our membrane at different pressures to verify the quality factor reduction we can achieve with this approach. We start the measurement from the lower possible pressure after few days of pumping. Then we reduce the rotational speed gradually. For each point we wait 20 minutes for the pressure to stabilize. The pressure is read through a pressure gauge placed at a distance of $\approx 20\,\mathrm{cm}$ from the membrane. An example of the reduction of the quality factor due to increased pressure is shown in Fig. 3.5. We use as a fit function

$$Q_{\mathrm{meas}}^{-1} = Q_{p=0}^{-1} + Q_{\mathrm{gas}}^{-1}(p), \tag{3.21}$$

where the first term is the dissipation diluted Q in absence of any gas damping contribution, while the second term represents the gas damping losses in the ballistic regime defined in Eq. (1.47). This particular set of data has been realized on a 17 nm-thick Lotus membrane. To take into account pressure differences between the membrane and the gauge location we introduce a correction factor α_{p} [Tsa19].

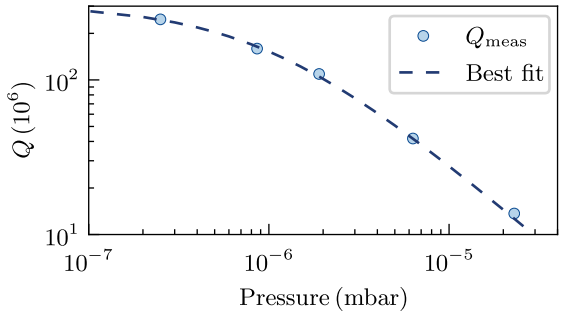

Figure 3.5: Quality factor as a function of pressure. We extract the quality factor from a ringdown measurement. Each point is the result over three repetitions averaged within each other. The dashed line is the best fit. The extracted correction factor for this particular measurement is $\alpha_{\mathrm{p}} = 1.57$.

This method does not require any additional tool and it is fast to realize. However, the reduction we can get is limited by the minimum rotational speed allowed by the pump (20% of the maximum rotational speed). Furthermore, operating the turbo pump below 50% of its rotational speed increases the mechanical noise in the system.

The last method we introduce to broaden the mechanical linewidth consists in introducing an external damping force through the piezo. To damp the motion, we need to exert a force on the membrane proportional and opposite to the velocity [AKM14], i. e. we want to realize a negative feedback loop on our membrane resonator. This method has been successfully implemented in cavity optomechanics experiments to cool a soft-clamped membrane motion down to the quantum regime using an optical feedback force [Ros+18]. We implement a similar electronic system to realize a feedback loop. However, we apply the feedback force through our piezo actuator with a configuration similar to the one implemented in [Pog+07].

A scheme of the feedback configuration is shown in Fig. 3.6 (a). We

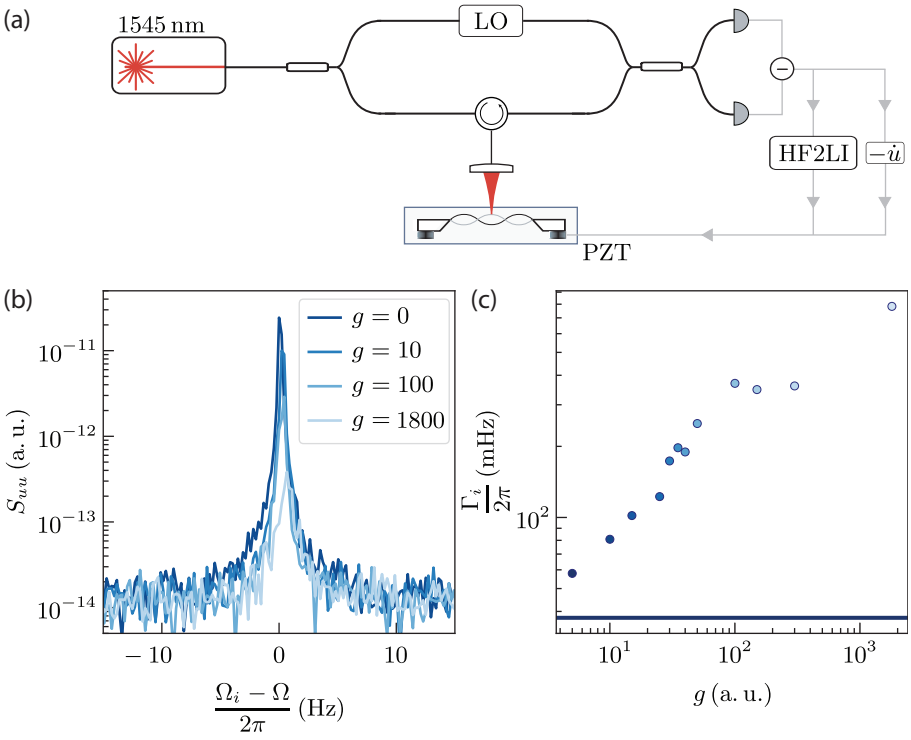

Figure 3.6: Feedback cooling. (a) Scheme of the feedback loop. The feedback signal is applied to the same piezo used to resonantly drive the membrane. (a) Thermal spectra at different gains of the feedback loop (increasing from dark to light blue). (b) Measured damping rates at different feedback loop gains. The damping rate is extracted from a single ringdown measurement. The blue horizontal line is the natural damping rate, that is in absence of feedback cooling.

measure the membrane motion through a Mach-Zehnder interferometer. The generated photocurrent is then sent to a digital processing unit which performs the time derivative of the signal (this estimates the velocity from the measured position), applies an electronic gain and generates the signal that we drive the piezo with. The generated signal is proportional to $-\dot{u}$, therefore it acts as an additional damping force. The

digital processing is implemented with a RedPitaya, a system-on-a-chip equipped with a field programmable gate array (FPGA). The firmware to implement the digital filter has been developed and interfaced with Python in the PyRpl module [Neu+17]. We want to generate a damping force only to the mode of interest. For this purpose, we apply a bandpass filter to the measured signal. We choose a filter which is approximately 600 Hz-wide and placed about 1.5 kHz above resonance. On the one hand, this filter removes all the contributions but from the mechanical mode of interest. On the other hand, it acts as a derivator for frequency below its central frequency. As a consequence of the derivative operation it applies a $-\pi/2$ phase shift to the input signal. We compensate for additional phase shifts due to phase delays by adding a phase offset to the generated signal. In Fig. 3.6 (b), we show a set of spectra acquired with different gains of the feedback loop. For the lowest gain, we cannot resolve the mechanical linewidth within a short measurement time. Therefore we perform a series of ringdowns (see Sec. 1.2.4) to estimate the damping rate as a function of the gain. An example is shown in Fig. 3.6 (c). The data shown in Fig. 3.6 (b), (c) are acquired on a 50 nm-thick Lotus membrane. The maximum amount of broadening we can obtain with the feedback is currently limited by the output voltage provided by the RedPitaya.

Part II

RESULTS

4

GEOMETRIC NONLINEARITIES

In this chapter we discuss the dynamics of a nanomechanical resonator under large deflections, that is when the amplitude of the oscillation becomes comparable with the smallest dimension of the resonator. In our case the smallest dimension coincide with the membrane thickness. In this regime, the model describing the resonator as damped harmonic oscillator fails to predict the resonator dynamics. We start with an overview of the observed nonlinear phenomena in micro- and nanomechanical resonators in the large displacement amplitude regime, consisting of a Duffing shift of the resonance frequency and an amplitude-dependent damping term. We attribute these nonlinear phenomena to a geometric origin, and we extend the model presented in Chapter 1 to include them. We derive analytic expressions capable of predicting such nonlinearities on resonators with arbitrary geometry. Then we describe the measurement protocol that we developed starting from the solution of the equation of motion of a nonlinear oscillator initially displaced from its rest position. We measure the nonlinear parameters on a significant number of geometries and we compare them with FEM simulations. Finally, we derive a non-trivial relation between the nonlinear parameters and the intrinsic losses which gives us the possibility to measure otherwise inaccessible information in highly-stressed nanomechanical resonators.

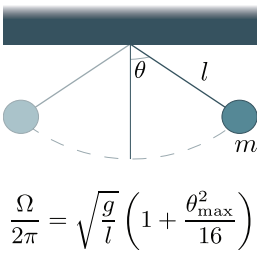

Nonlinear simple pendulum.

4.1 DUFFING OSCILLATOR

The damped harmonic oscillator model is a good approximation to describe the dynamics of a single eigenmode of a micro- or nanomechanical oscillator in most of the cases (see Sec. 1.2). However, when the displacement amplitude becomes comparable with the resonator thickness, nonlinear phenomena starts to appear and the damped harmonic oscillator description is not enough anymore.

The first nonlinear phenomenon we expect to observe is a dependence of the resonance frequency on the displacement amplitude. We can include this source of nonlinearity through simple energy considerations. In the small oscillation regime the potential energy associated with a single mode of oscillation can be simply written as a harmonic potential $W = m_i\Omega_i^2 u_i^2/2$, which can also be seen as the bending energy (for

unstressed resonator) or the tensile energy (for pre-stressed resonators) both introduced in Sec. 1.3.2 (see Eq. (1.49) and Eq. (1.54)). When the displacement becomes large, we need to expand the potential energy including higher order terms in the displacement [Hoc+14; CTS20]. By symmetry considerations, the odd terms do not give any energy contribution, hence the next term in the potential energy is $\propto u^4$ [Hoc+14; CTS20], consistent with the energy contribution associated with the elongation energy (see Eq. (1.51)). A fourth order term in the potential energy introduces a contribution $\propto u^3$ in the equation of motion, which takes the form

$$\ddot{u}_i + \Gamma_i \dot{u}_i + \Omega_i^2 u + \frac{\alpha_i}{m_i} u^3 = \frac{f_i^{\text{ext}}}{m_i}, \tag{4.1}$$

referred to as Duffing equation [LL70; NM95; SVR16]. The parameter α_i is called the Duffing parameter and has unit of N/m^3. Eq. (4.1) is a third order equation and presents three solutions, two stable and one unstable. The frequency response is depicted in Fig. 4.1 (a). It

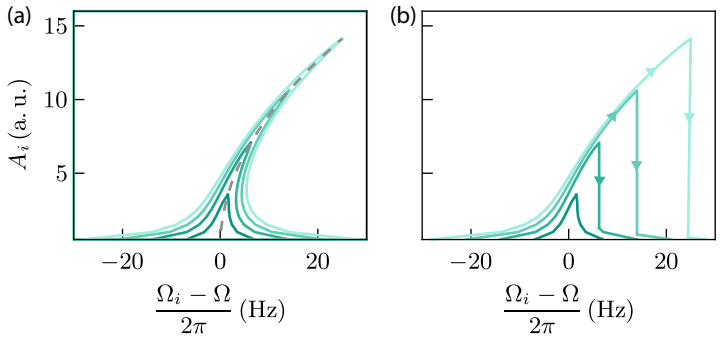

Figure 4.1: Expected driven response of the Duffing resonator. (a) Analytical solution of the Duffing equation in the driven case. Each solid line represents a realization with a fixed driving strength. The lighter the color the stronger the force applied. The dashed line represents the backbone equation (Eq. (4.2)). (b) Expected driven response for a real measurement. Sweeping the driving frequency from left to right the amplitude jumps from one stable solution to the other.

consists of a deformed Lorentzian curve where the peak tilts to the right (hardening) or to the left (softening), depending on the source of nonlinearity and the consequent sign of α_i. For geometric Duffing nonlinearity in membrane resonators the sign of α is always positive (therefore we are only interested in the hardening). Notice that in Fig. 4.1 (a) the amplitude goes through all the three solutions. In a real experiment when we perform a driven measurement we observe a jump from one stable solution to the other [FPT12; Def+12; Hoc+14; SVR16] without going through the unstable solution, see Fig. 4.1 (b). If we invert the sweep direction the jump happens at different frequency. In both the directions the jump point coincides with the transition between the stable and unstable solutions [SVR16]. In Fig. 4.1 (b) we only show

the up direction. To be able to reconstruct the full solution an active control of the oscillator phase is required [Cua+21]. The positions of the maxima in Fig. 4.1 (a) follow the so called *backbone curve* [NM95]:

$$\Omega_i^{\max} = \Omega_i + \frac{3}{8}\frac{\alpha}{\Omega_i} A_i^{\max}. \tag{4.2}$$

The above equation coincides with the time derivative of the phase we get from the solution of the Duffing equation in the time domain [NM95].

A second effect that has been observed often in presence of Duffing nonlinearity is the so-called *nonlinear damping*. Unlike the former, it is a dissipative type of nonlinearity and introduces an amplitude dependence in the damping component. It has been observed in S_iN membrane [CTS20; Cat+21], diamod nanoresonators [IWM13], carbon nanotubes and graphene sheets [Eic+11]. Despite the large number of observations of this nonlinear phenomenon, a clear explanation of its origin is still missing. On one hand, a theoretical modeling of nonlinear damping as an anharmonic coupling between different vibrational modes has been proposed in [Ata+16], on the other hand analytic expressions of nonlinear damping starting from purely geometrical considerations has been derived for string resonator [SVR16], rectangular plate [Ama18] and highly-stressed membrane [Cat+21]. In particular in [Cat+21] we compared the theoretical expectation with the experimental results on a wide number of membrane resonators with different geometries. The details of such theoretical modeling and the experimental results are discussed in the next sections.

4.2 CONTINUUM ELASTIC MODELING

In Chapter 1 we use the fundamental concepts of elasticity theory to derive the equation of motion of a thin membrane starting from the stress-strain relations. Using a discretization method we find that the dynamics of a single normal mode can be described by a damped harmonic oscillator model. However, the experimental evidence discussed in, for instance, [FPT12; Def+12; Hoc+14; Cua+21] suggests that this description fails when we enter in the large displacement regime. We now extend the derivation presented for a linear membrane resonator to include the nonlinear parameters. Notice that the same derivation can be applied for resonators of different shapes as long as the condition $L \gg h$ is satisfied.

We start again with a thin square membrane in the reference frame shown in Fig. 1.1. Here we want to investigate the large displacement amplitude regime, defined by the condition $w \approx h$. When this condition is fulfilled, the elongation that the membrane experiences during the oscillation becomes relevant. We can understand this by comparing the bending (ΔW_{bend}) and the elongation (ΔW_{elong}) dissipated energies. The latter becomes relevant when the ratio between the two approaches

one. We estimate the energy dissipated per unit cycle in the simple case of a string with the modeshape approximated by the expression $\sin(\frac{n\pi}{L}x)$, with L the length of the string and n the mode number. We assume a time-dependent out-of-plane displacement associated with the mode n can be described by a harmonic oscillation $u_n(t) = u_n \cos(\Omega_n t)$. To evaluate the bending and the elongation dissipated energy we insert Eq. (1.52) and Eq. (1.50) in Eq. (1.15b). Using the string modeshape the resulting dissipated energies per unit cycle are

$$\Delta W_{\text{bend}} = \frac{E\tau u_0^2 h^3 L}{48(1-\nu^4)} \left(\frac{n\pi}{L}\right)^4, \tag{4.3a}$$

$$\Delta W_{\text{elong}} = \frac{3E\tau L h u_0^2}{128(1-\nu^4)} \left(\frac{n\pi}{L}\right)^4. \tag{4.3b}$$

We are interested in the ratio between the two above expressions. After some algebra the ratio between the two energies reduces to

$$\frac{\Delta W_{\text{elong}}}{\Delta W_{\text{bend}}} = \frac{9}{8}\frac{u_0^2}{h^2}, \tag{4.4}$$

meaning that we expect to see nonlinear effects when $u_0 \approx h$, consistent with the assumption $w \approx h$.

To include the contribution of the elongation due to a large oscillation in the out-of-plane direction we include a second order term in the strain components which takes the form [LL70]:

$$\varepsilon_{ij} = \frac{1}{2}(\partial_j d_i + \partial_i d_j + \partial_i d_z \partial_j d_z). \tag{4.5}$$

Furthermore, we assume that the membrane thickness is constant during the oscillation, e. g. $\sigma_{iz} = 0$, and that the material satisfies Hooke's law. Within these conditions, the displacement vector components have the same expression derived for the linear case and reported in Eqs. (1.6). If we insert the displacement vector components in Eq. (4.5) we find the nonlinear strain tensor components can be expressed as following:

$$\varepsilon_{\alpha\beta}(x,y) = \varepsilon_0 \delta_{\alpha\beta} - z\partial_{\alpha\beta} w + \frac{1}{2}\partial_\alpha w \partial_\beta w. \tag{4.6}$$

Notice that the Greek indexes stand for the x and y directions, ε_0 is a static in-plane deformation and we performed the out-of-plane approximation. The relation between the strain and the stress tensor components is not affected by the large displacement amplitude regime and is still described by Eq. (1.12). However the nonlinear contributions enter in the stress tensor through the nonlinear term in Eq. (4.6).

We want to derive the equation of motion for $w(x,y,t)$. First we need to derive the stress components substituting Eq. (4.6) into Hooke's Eq. (1.12). From the stress components we can derive the shear forces ($N_{\alpha\beta}$) and the bending momenta ($M_{\alpha\beta}$) substituting the stress expressed as a function of w in Eq. (1.10a) and Eq. (1.10b), respectively. In the

bending momenta, the only non-zero terms are the one associated with the bending stress

$$M_{\alpha\beta} = D\left[(1-\nu)(\partial_{\alpha\beta}w + \partial_{\alpha\beta}\dot{w} + \nu(\partial_{\gamma\gamma}w + \partial_{\gamma\gamma}\dot{w})\delta_{\alpha\beta}\right], \tag{4.7}$$

with D the flexural rigidity. The above expression coincides with the one we obtain in the linear case. Let us now evaluate the shear forces. In the linear case, the only stress components contributing to the shear forces are the ones related to the tensile stress. In the large displacement amplitude regime, also the elongation stress contributes to the shear forces which has the following form

$$N_{\alpha\beta} = k_1\left[\varepsilon_0\delta_{\alpha\beta} + \frac{\partial_\alpha w\partial_\beta w}{2} + \partial_\alpha w\partial_\beta\dot{w} + \nu\left(\frac{(\partial_\gamma w)^2}{2} + \partial_\gamma w\partial_\gamma\dot{w}\right)\delta_{\alpha\beta}\right], \tag{4.8}$$

with $k_1 = Eh/(1-\nu^2)$. To estimate the equation of motion we need to substitute $N_{\alpha\beta}$ and $M_{\alpha\beta}$ in Eqs. (1.8a). By using the above expressions, we notice that we can write $-\partial_{\alpha\beta}M_{\alpha\beta} = D\partial_{\alpha\alpha\beta\beta}M_{\alpha\beta}$. Then we use Eq. (1.8b) to write $\partial_\beta(N_{\alpha\beta}\partial_\alpha w) = N_{\alpha\beta}\partial_{\alpha\beta}w$, where the first term on the left hand side of the latter coincides with $\nabla\cdot\vec{n}$. By substituting the above equalities in Eq. (4.8), we find the following equation of motion

$$\rho h\ddot{w} + \tau(D\partial_{\alpha\alpha\beta\beta}\dot{w} - \mathcal{G}(w)) + D\partial_{\alpha\alpha\beta\beta}w - h\sigma_0\partial_{\alpha\alpha}w - \mathcal{O}(w) = F^{\text{ext}}, \tag{4.9}$$

where $\mathcal{G}(w)$ and $\mathcal{O}(w)$ are two functions of the out-of-plane displacement and they represent the contribution of the elongation to the damping and the harmonic part of the equation of motion, respectively. They can be written explicitly as follows:

$$\mathcal{G}(w) = k_1\left(\partial_{\alpha\beta}w\partial_\alpha\dot{w}\partial_\beta w + k_2\partial_{\alpha\alpha}w\partial_\beta\dot{w}\partial_\beta w\right), \tag{4.10a}$$

$$\mathcal{O}(w) = \frac{k_1}{2}\left(\partial_{\alpha\beta}w\partial_\alpha w\partial_\beta w + k_2\partial_{\alpha\alpha}w\partial_\beta w\partial_\beta w\right) \tag{4.10b}$$

with $k_2 = \nu/(1-\nu)$.

Now we want to move from an equation of motion for the overall displacement field, e. g. Eq. (4.9), to an equation of motion describing the dynamics of a single mode. In the linear case, we expand the out-of-plane displacement over a set of normalized modes $\phi_n(x,y)$ by writing $w(x,y,t) = u_n(t)\phi_n(x,y)$, where u_n is the out-of-plane displacement associated with the nth normalized mode. We perform the same expansion assuming that the normalized mode $\phi_n(x,y)$ evaluated in the linear case form a basis for the out-of-plane displacement also in the nonlinear regime. For nonlinearities as small as the ones considered in this work such approximation is always valid. After performing this expansion the equation of motion becomes

$$\rho h\phi_n\ddot{u}_n + \tau(D\partial_{\alpha\alpha\beta\beta}\phi_n - \tau\mathcal{G}'u_n^2)\dot{u}_n + (D\partial_{\alpha\alpha\beta\beta}\phi_n - h\sigma_0\partial_{\alpha\alpha}\phi_n)u_n + \\ - \mathcal{O}'u_n^3 = F^{\text{ext}},$$

(4.11)

where the repeated index are summed over and we introduced the two functions $\mathcal{G}'$ and $\mathcal{O}'$ expressed by

$$\mathcal{G}' = k_1 \left(\partial_{\alpha\beta}\phi_n \partial_\alpha \phi_n \partial_\beta \phi_n + k_2 \partial_{\alpha\alpha}\phi_n \partial_\beta \phi_n \partial_\beta \phi_n\right), \tag{4.12a}$$

$$\mathcal{O}' = \frac{k_1}{2} \left(\partial_{\alpha\beta}\phi_n \partial_\alpha \phi_n \partial_\beta \phi_n + k_2 \partial_{\alpha\alpha}\phi_n \partial_\beta \phi_n \partial_\beta \phi_n\right). \tag{4.12b}$$

We then apply the Galerkin method and perform the single-mode approximation to move from Eq. (4.11) to the equation of motion for a single mode

$$\ddot{u}_i + \Gamma_i \dot{u}_i + \gamma_i^{\mathrm{nl}} u_i^2 \dot{u}_i + \Omega_i^2 u_i + \beta_i u_i^3 = \frac{f_i^{\mathrm{ext}}}{m_i}, \tag{4.13}$$

where $f_i^{\mathrm{ext}} = \int_S \phi_i F^{ext} dS$ and we find the following effective parameters

$$m_i = \int_S h\rho\phi_i^2 dS, \tag{4.14a}$$

$$\Omega_i^2 = \frac{1}{m_i} \int_S \phi_i \left(D\partial_{\alpha\alpha\beta\beta}\phi_i - h\sigma_0 \partial_{\alpha\alpha}\phi_i\right) dS, \tag{4.14b}$$

$$\Gamma_i = \frac{D\tau}{m_i} \int_S \phi_i \partial_{\alpha\alpha\beta\beta}\phi_i dS, \tag{4.14c}$$

$$\beta_i = -\frac{k_1}{2m_i} \int_S \phi_i [\partial_{\alpha\beta}\phi_i \partial_\alpha \phi_i \partial_\beta \phi_i + k_2 \partial_{\alpha\alpha}\phi_i \partial_\beta \phi_i \partial_\beta \phi_i] dS, \tag{4.14d}$$

$$\gamma_i^{\mathrm{nl}} = -\frac{k_1}{m_i}\tau \int_S \phi_i [\partial_{\alpha\beta}\phi_i \partial_\alpha \phi_i \partial_\beta \phi_i + k_2 \partial_{\alpha\alpha}\phi_i \partial_\beta \phi_i \partial_\beta \phi_i] dS. \tag{4.14e}$$

The linear effective parameters m_i and Γ_i coincide with the one obtained in Sec. 1.2.3. If we follow the steps in Sec. 1.2.3 applying the divergence theorem, the nonlinear effective parameters and the resonance frequency squared simplify to

$$\Omega_i^2 = \frac{1}{m_i} \int_S \phi_i \left[D\partial_{\alpha\alpha\beta\beta}\phi_i + h\sigma_0 \left(\partial_x \phi_i + \partial_y \phi_i\right)^2\right] dS, \tag{4.15a}$$

$$\beta_i = \frac{Eh}{2m_i(1-\nu^2)} \int_S \left[(\partial_x \phi_i)^2 + (\partial_y \phi_i^2)\right]^2 dS, \tag{4.15b}$$

$$\gamma_i^{\mathrm{nl}} = \frac{Eh\tau}{m_i(1-\nu^2)} \int_S \left[(\partial_x \phi_i)^2 + (\partial_y \phi_i^2)\right]^2 dS, \tag{4.15c}$$

where Ω_i^2 has now the same form as for the linear case.

Eq. (4.13) represents the equation of motion of a damped harmonic oscillator including now two nonlinear terms, one of the two giving rise to a dissipative contribution. β_i is the Duffing nonlinearity normalized by the effective mass and γ_i^{nl} is the so-called nonlinear damping. We want to highlight here that the two nonlinear parameters come from the same source, which is purely geometric and coincides with the elongation

that the membrane experiences during the oscillation. For this reason, we generally refer to them as *geometric nonlinearities*. Moreover, we notice that the two nonlinear terms share the same spatial dependence from the modeshape, consistent with their common geometric source.

4.3 NONLINEAR DYNAMICS

In the previous section we derive a model for the Duffing and the damping nonlinearities starting from geometric considerations. The effective parameters we get at the end of the derivation allow us to predict the value of those parameters as long as we can evaluate the eigenmodes of the resonator. In our case we can always obtain this information through FEM simulations. To evaluate the validity of the model, we want to measure the values of the nonlinear parameters and compare them with the simulated ones. The standard way of measuring the Duffing nonlinearity [Hoc+14; FPT12; Dav+17] and the nonlinear damping [Ant+12; Zai+11] is through a driven approach. We need to apply an external excitation force and sweep the driving frequency across the resonance. Then the same procedure has to be repeated at different driving forces. The very small linewidth (few tens of mHz) featured by our membrane resonators imposes an extremely long measurement time to perform this type of measurement with a resolution small enough to resolve the mechanical peak. On the time scale needed to perform such measurement, unwanted frequency drifts due to thermal fluctuations or other source of frequency noise will affect the measurement results. In the linear case we avoid this problem by performing ringdown measurement where we initially displaced the membrane from its rest position and we monitor the amplitude decay (see Sec. 1.2.4 for further details). The ringdown measurement allows us to extract the information in a considerably shorter time, usually few minutes for the higher quality factors at room temperature. To implement a similar measurement procedure we need to find how the nonlinear parameters affect both the amplitude and the frequency during the ringdown time, an approach already implemented in [Pol+16].

We now solve the equation of motion for the nonlinear Duffing oscillator in the presence of a nonlinear damping term during the free decay [CTS20]. We solve Eq. (4.13) assuming $f_i^{\mathrm{ext}} = 0$ and that the oscillator is initially displaced from its equilibrium position to a given amplitude

$$u_i(0) = A_{i,0}. \tag{4.16}$$

We already mention that we are in the low dissipation regime and our system is characterized by small nonlinearities. It is useful to highlight the small terms with an ϵ

$$\ddot{u}_i + \epsilon\tilde{\Gamma}_i\dot{u}_i + \epsilon\tilde{\gamma}_i^{\mathrm{nl}}u_i^2\dot{u}_i + \Omega_i^2 u_i + \epsilon\tilde{\beta}_i u_i^3 = 0, \tag{4.17}$$

where we performed the substitutions $\epsilon\tilde{\Gamma}_i = \Gamma_i$, $\epsilon\tilde{\gamma}_i^{\mathrm{nl}} = \gamma_i^{\mathrm{nl}}$ and $\epsilon\tilde{\beta}_i = \beta_i$. We solve the above equation performing the same derivation reported

in [Nay93] for a Duffing oscillator. We extend the solution including the presence of the nonlinear damping term.

We apply the so-called multiple-scales method. It consists in introducing a new time variable $t_1 = \epsilon t$, defining a slow time scale. The natural time variable defines a fast time scale $t_0 = t$. The harmonic oscillation is associated with t_0, the two damping terms and the Duffing nonlinearity with t_1. We write the general solution as a function of the two new time scales as

$$u_i(t) = u_i(t, \epsilon t) = u_i(t_0, t_1). \tag{4.18}$$

We can express the time derivatives in terms of the new time variables. Using the chain rules, the first and second order time derivatives becomes

$$\frac{d}{dt} = \partial_{t_0} + \epsilon \partial_{t_1}, \tag{4.19a}$$

$$\frac{d^2}{dt^2} = \partial_{t_0 t_0} + 2\epsilon \partial_{t_0 t_1}. \tag{4.19b}$$

Substituting Eq. (4.19) in Eq. (4.17) we find the equation of motion as a function of the new time scales

$$\left(\partial_{t_0 t_0} + \epsilon \partial_{t_0 t_1}\right) u_i + \epsilon \left(\tilde{\Gamma}_i + \epsilon \tilde{\gamma}_i^{\mathrm{nl}} u_i^2\right) \partial_{t_0} u_i + \Omega_i^2 u_i + \epsilon \tilde{\beta}_i u_i^3 = 0, \tag{4.20}$$

where we neglected all the higher order terms in ϵ. To solve the above equation we need to introduce an uniform approximate solution writing $u_i(t_0, t_1)$ as

$$u_i(t_0, t_1) = u_{i,0}(t_0, t_1) + \epsilon u_{i,1} u(t_0, t_1). \tag{4.21}$$

Using the above approximate solution, the equation of motion in Eq. (4.20) takes the following form

$$\begin{aligned} &\partial_{t_0 t_0} u_{i,0} + \Omega_i^2 u_{i,0} + \epsilon \Big[\partial_{t_0 t_0} u_{i,1} + 2\partial_{t_0 t_1} u_{i,0} + \tilde{\Gamma}_i \partial_{t_0} u_{i,0} + \\ &+ \tilde{\gamma}_i^{\mathrm{nl}} u_{i,0}^2 \partial_{t_0} u_{i,0} + \Omega_i^2 u_{i,1} + \tilde{\beta}_i u_{i,0}^3 \Big] = 0, \end{aligned} \tag{4.22}$$

where again we kept only the terms up to the first order in ϵ and neglected the higher order terms. To find the solution of Eq. (4.22) we can divide the problem in solving two separate equations, one for the slow terms (the one proportional to ϵ) and one for the fast terms. This corresponds to solve the following two equations:

$$\partial_{t_0 t_0} u_{i,0} + \Omega_i^2 u_{i,0} = 0, \tag{4.23a}$$

$$\begin{aligned} \partial_{t_0 t_0} u_{i,1} + \Omega_i^2 u_{i,1} = &- 2\partial_{t_0 t_1} u_{i,0} - \tilde{\Gamma}_i \partial_{t_0} u_{i,0} + \\ &- \tilde{\gamma}_i^{\mathrm{nl}} u_{i,0}^2 \partial_{t_0} u_{i,0} - \Omega_i \tilde{\beta}_i u_{i,0}^3. \end{aligned} \tag{4.23b}$$

The first equation is the equation of a simple harmonic oscillator in t_0. We can write its solution as

$$u_{i,0} = A_i(t_1) \cos\Big(\Omega_i t_0 + \varphi_i(t_1)\Big), \tag{4.24}$$

where the unknown constants $A_i(t_1)$ and $\varphi_i(t_1)$ depend on the boundary conditions and on the solution of the second equation.

Then we move to find the solution for the slow terms equation. By inserting Eq. (4.24) in Eq. (4.23b), and after applying the trigonometric identity $\cos(3t) = 4\cos^3(t) - 3\cos(t)$, Eq. (4.23b) becomes

$$\begin{aligned}\partial_{t_0 t_0} u_{i,1} + \Omega_i^2 u_{i,1} = {} & \Omega_i F_1 \sin\Big(\Omega_i t_0 + \beta_i(t_1)\Big) + \\ & + \Omega_i F_2 \cos\Big(\Omega_i t_0 + \varphi_i(t_1)\Big) + \\ & + \Omega_i F_3 \sin\Big(3\Omega_i t_0 + 3\varphi_i(t_1)\Big) + \\ & + \Omega_i F_4 \cos\Big(3\Omega_i t_0 + 3\varphi_i(t_1)\Big),\end{aligned} \tag{4.25}$$

where we introduced

$$F_1 = 2\partial_{t_1} A_i(t_1) + \tilde{\Gamma}_i A_i(t_1) + \frac{1}{4}\tilde{\gamma}_i^{\mathrm{nl}} A_i^3(t_1), \tag{4.26a}$$

$$F_2 = 2A_i(t_1)\partial_{t_1}\varphi_i(t_1) - \frac{3}{4}\frac{\tilde{\beta}_i}{\Omega_i} A_i^3(t_1), \tag{4.26b}$$

$$F_3 = \frac{1}{4}\tilde{\gamma}_i^{\mathrm{nl}} A_i^3(t_1), \tag{4.26c}$$

$$F_4 = -\frac{1}{4}\frac{\tilde{\beta}_i}{\Omega_i} A_i^3(t_1). \tag{4.26d}$$

Limiting ourselves to solve the above equation would introduce the so-called secular terms in the solution, e. g. terms proportional to $t_0\cos(\Omega_i t_0)$ or $t_0\sin(\Omega_i t_0)$ which would lead to a solution growing without any bound. The presence of these terms does not have any physical meaning, it is just an artifact introduced by the perturbation [IOS18]. To avoid the secular terms, we need to impose the condition that the coefficients in front of $\sin(\Omega_i T_0 + \varphi_i(T_1))$ and $\cos(\Omega_i T_0 + \varphi_i(T_1))$ are equal to zero, e. g. $F_1 = F_2 = 0$. By imposing these conditions we obtain the two following equations for A_i and φ_i:

$$2\partial_{t_1} A_i(t_1) + \tilde{\Gamma}_i A_i(t_1) + \frac{1}{4}\tilde{\gamma}_i^{\mathrm{nl}} A_i^3(t_1) = 0 \tag{4.27a}$$

$$2A_i(t_1)\partial_{t_1}\varphi_i(t_1) - \frac{3}{4}\frac{\tilde{\beta}_i}{\Omega_i} A_i^3(t_1) = 0. \tag{4.27b}$$

We solve Eq. (4.27a) and Eq. (4.27b)separately. We start with Eq. (4.27a). It is a differential equation in A_i of the first order that we can easily solve. The solution describes the evolution of the displacement amplitude in terms of the slow varying time scale t_1:

$$A_i^2(t_1) = \frac{c e^{-\tilde{\Gamma}_i t_1}}{1 - c\frac{\tilde{\gamma}_i^{\mathrm{nl}}}{4\tilde{\Gamma}_i} e^{-\tilde{\Gamma}_i t_1}}. \tag{4.28}$$

To determine the value of the parameter c we need to impose the initial condition defined in Eq. (4.16). Next, we need to find the time evolution

of $\varphi_i(t_1)$. We substitute the expression we found for the amplitude, Eq. (4.28), in Eq. (4.27b) which becomes:

$$\varphi_i(t_1) = \frac{3}{8}\frac{\tilde{\beta}_i}{\Omega_i}\frac{4}{\tilde{\gamma}_i^{\mathrm{nl}}}\log\left(1 - c\frac{\tilde{\gamma}_i^{\mathrm{nl}}}{4\tilde{\Gamma}_i}e^{-\tilde{\Gamma}_i t_1}\right) + \Phi. \tag{4.29}$$

Again Φ is a constant whose value depends on the initial conditions. Substituting the derived expressions for $A_i(T_1)$ and $\varphi_i(T_1)$ in Eq. (4.24) we obtain the zeroth order term of the solution $u_{i,0}(t_0, t_1)$.

The problem of finding the first order solution reduces to solving the following equation

$$\begin{aligned}\partial_{t_0 t_0} u_{i,1} + \Omega_i^2 u_{i,1} = \Omega_i F_3 \sin\Big(3\Omega_i t_0 + 3\varphi_i(t_1)\Big) + \\ + \Omega_i F_4 \cos\Big(3\Omega_i t_0 + 3\varphi_i(t_1)\Big),\end{aligned} \tag{4.30}$$

with F_3 and F_4 are defined in Eqs. (5.27). However, we decide to keep only the zeroth order terms in ϵ, e. g. the full solution is represented by $u_i(t) \approx u_{i,0}(t_0, t_1)$. Within this condition we only need to substitute the expression for $A_i(t_1)$ and $\varphi_i(t_1)$ into Eq. (4.24) and impose the initial condition in Eq. (4.16). Finally, we write the solution in terms of the initial parameters and the natural timescale t, which coincides with the experiment timescale. After imposing the initial condition in Eq. (4.16) we obtain the solution

$$u_i(t) = A_i(t)\cos(\Omega_i t + \varphi_i(t) + \Phi), \tag{4.31}$$

where

$$A_i(t) = \frac{A_{i,0}e^{-\frac{\Gamma_i}{2}t}}{\sqrt{1 + \frac{\gamma_i^{\mathrm{nl}}}{4\Gamma_i}A_{i,0}^2\left(1 - e^{-\Gamma_i t}\right)}}, \tag{4.32a}$$

$$\varphi(t) = \frac{3}{8}\frac{4\beta_i}{\gamma_i^{\mathrm{nl}}}\log\left(1 + \frac{\gamma_i^{\mathrm{nl}}}{4\Gamma_i}A_{i,0}^2\left(1 - e^{-\Gamma_i t}\right)\right) + \Phi. \tag{4.32b}$$

The constant Φ is still unknown. Defining it would require an additional initial condition on $\dot{u}_i(0)$. Since we are interested only in the resonance frequency shift, knowing its value does not give us any additional parameter as we show in the next steps.

From Eqs. (4.32) we are able to describe the time evolution of the displacement amplitude and phase in the presence of geometric nonlinearities during the ringdown. As expected, the amplitude decay is only affected by the nonlinear damping term. From Eq. (4.32a) we observe few things. We notice that from the amplitude decay we can extract both the linear and the nonlinear damping term. Then we observe that the contribution of the nonlinear damping is relevant only at the beginning of the ringdown. When the exponential term at the denominator becomes ≈ 1, the displacement amplitude decay can be approximated by the standard exponential decay.

Differently, the Eq. (4.32b) describing the time evolution of the phase shift is affected by both the nonlinear damping and the Duffing nonlinearity and, at a first look, it is hard to associate with the description of a Duffing oscillator given in Sec. (4.1). Nevertheless, if we perform the time derivative of the phase we find a time-dependent shift of the resonance frequency with the following form:

$$\Omega_i'(t) = \frac{d\varphi_i}{dt} = \Omega_i + \frac{3}{8}\beta_i \underbrace{\frac{A_{i,0}^2 e^{-\Gamma_i t}}{1 + \frac{\gamma_i^{\mathrm{nl}}}{4\Gamma_i} A_{i,0}^2 \left(1 - e^{-\Gamma_i t}\right)}}_{A_i^2(t)} . \tag{4.33}$$

Importantly the above equation has the same form of the backbone equation (Eq. (4.2)). The only difference is that Eq. (4.33) describes the instantaneous frequency shift as a function of the instantaneous amplitude instead of the maximum frequency shift in terms of the maximum displacement amplitude associated with a given driving strength. This result confirmed that we can extract the nonlinear Duffing parameter from a ringdown measurement if we are able to monitor the instantaneous frequency shift and the displacement amplitude simultaneously.

4.4 MEASURING NONLINEARITIES

In the previous section we derived the time evolution of the amplitude and of the instantaneous resonance frequency shift. In this section, we apply those laws to extract the nonlinear parameters from a real measurement. The requirement to perform the measurement is being able to monitor the displacement amplitude and the instantaneous resonance frequency shift simultaneously. To measure the displacement we use a fiber based Mach-Zehnder interferometer described in Sec. 3.1. We then feed the interferometric signal to a lock-in amplifier which returns the amplitude and the phase of the signal (see Sec. 3.2). Finally, from the time derivative of the phase we extract the instantaneous resonance frequency shift (more details in Sec. 3.5). Notice that to express the nonlinear damping and the Duffing parameter in their standard units ($\mathrm{Hz/m^2}$ and $\mathrm{Hz^2/m^2}$) we need to calibrate the displacement in unit of m. For this set of measurements we apply an absolute calibration method. Details regarding the calibration procedure are reported in Sec. 3.3.1.

We perform this sets of measurements using the heterodyne detection scheme. The measurement protocol does not require an active stabilization of the resonance frequency since the Duffing resonance frequency shift is happening at a faster timescale than the thermal drifts discussed in Sec. 3.6. Moreover, we expect the geometric nonlinearities to become relevant when the condition $w \approx h$ is satisfied. For the thicker membranes (100 nm-thick) the resulting phase modulation is so large that we need to correct for nonlinear optical transduction of the interferometer signal, what we call the carrier correction. To perform such correction

the heterodyne detection is advantageous. Details about the carrier correction can be found in Sec. 3.4.

The measurement procedure consists in driving the membrane resonator through piezoelectric excitation up to an amplitude where we expect to observe nonlinear effects. Then, we stop driving and we monitor the amplitude and the phase during the ringdown time. From the amplitude decay we derive the linear and the nonlinear damping parameter using Eq. (4.32a) as fitting function. An example of a nonlinear amplitude decay for the first bandgap mode of a Dahlia generation 2 membrane 19 nm-thick is reported in Fig. 4.2 (a). It is interesting

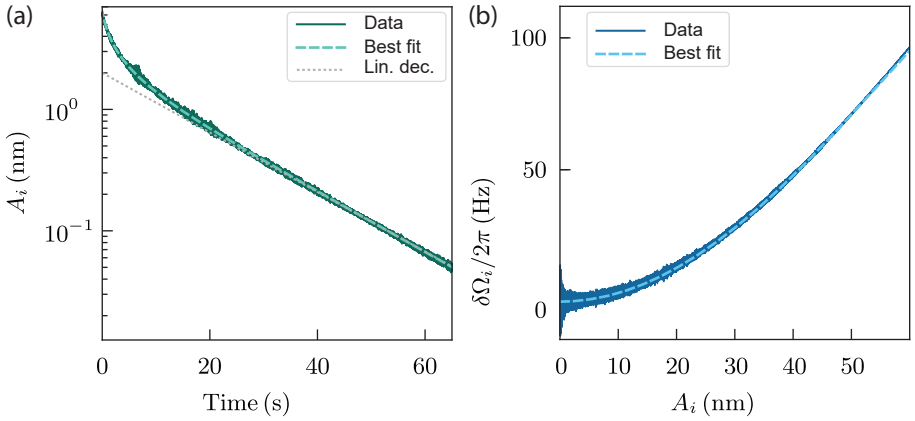

Figure 4.2: Displacement amplitude and instantaneous resonance frequency shift during the ringdown. (a) Nonlinear ringdown of the displacement amplitude. The dark green solid line represents the real data, the light green dashed line is the best fit. The grey dot line is the linear ringdown with Γ_i extracted from the best fit of the nonlinear decay. (b) Instantaneous resonance frequency shift against the displacement amplitude. The dark blue solid line represents the real data, the light blue dashed line is the best fit. We use the amplitude obtained from the best fit in (a) as displacement amplitude.

to notice that the amplitude decay starts to deviate from the linear exponential one when the displacement amplitude is comparable with the membrane thickness as expected.

To measure the Duffing parameter we extract the instantaneous frequency from the measured phase and we plot it against the displacement amplitude. As a fit function we use Eq. (4.33) including an additional correction term $\propto A^4$. An example of a measured resonance frequency shift is reported in Fig. 4.2 (b). From these two measurements we are able to extract the nonlinear parameters and the linear damping. The only parameter missing to have a complete characterization of a membrane resonator is the mechanical frequency. We assume that the resonance frequency coincide with the demodulator frequency Ω_d that we always use to set the frequency of the driving force. Therefore, from

a nonlinear ringdown we not only get the nonlinear parameters but also the linear decay rate and the resonance frequency. From the last two parameters we estimate the quality factor.

To confirm that the Duffing parameter measured during the ringdown and the one extracted from the standard driven measurement coincide, we superimposed the instantaneous resonance frequency shift to a sweep measurement. First we perform a ringdown and extract the instantaneous frequency shift. Then we move to perform a set of sweep measurements. To reduce the measurement time we broaden the mechanical linewidth increasing the vacuum chamber pressure up to 3×10^{-3} mbar. Since the Duffing parameter is a purely geometric term, it should not be affected by the presence of the gas damping. In Fig. 4.3

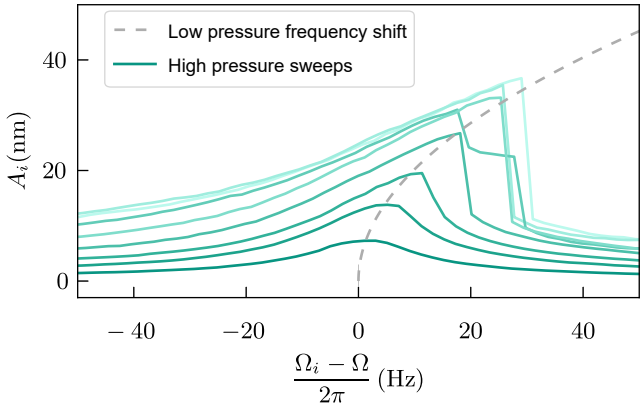

Figure 4.3: High pressure sweeps. For each color we use a different driving strength. Each curve is obtained averaging 5 different curves measured with the same condition. The grey dotted line represents the fit of the frequency shift measured on the same membrane at low pressure through the ringdown technique.

we plot the fit of the instantaneous frequency shift measured during low pressure ringdown on top of the high pressure sweeps. The low pressure frequency shift is superimposed to the maximum frequency shift point of each curve and is following the backbone curve as expected. We are not performing any resonance frequency stabilization but, before each sweep, we measure the central mechanical frequency and we use it to center all the curves. We attribute the small discrepancy between the ringdown shift and the maximum shift point to residual thermal drift happening during the driven frequency sweep. The sweeps are performed using the network analyzer sweeper function of the HF2LI.

Next we want to prove the consistency of the model we derived in sec 4.2. To do so, we need to measure the nonlinear parameters and compare them with the simulated values evaluated through Eq. (4.14d) and Eq. (4.14e). We choose as geometry of interest the Dahlia generation 2 membrane design. The presence of several bandgap modes characterized by high quality factor, e. g. easy to drive in the nonlinear regime also at room temperature, together with our knowledge about the accuracy

of our simulated modeshapes [Bar+16] makes them the ideal samples for this type of measurements. We characterize the first 4 bandgap modes. The simulated modeshapes and the simulated frequencies are reported in Fig. 4.4 (a). For each modeshape we perform 5 nonlinear

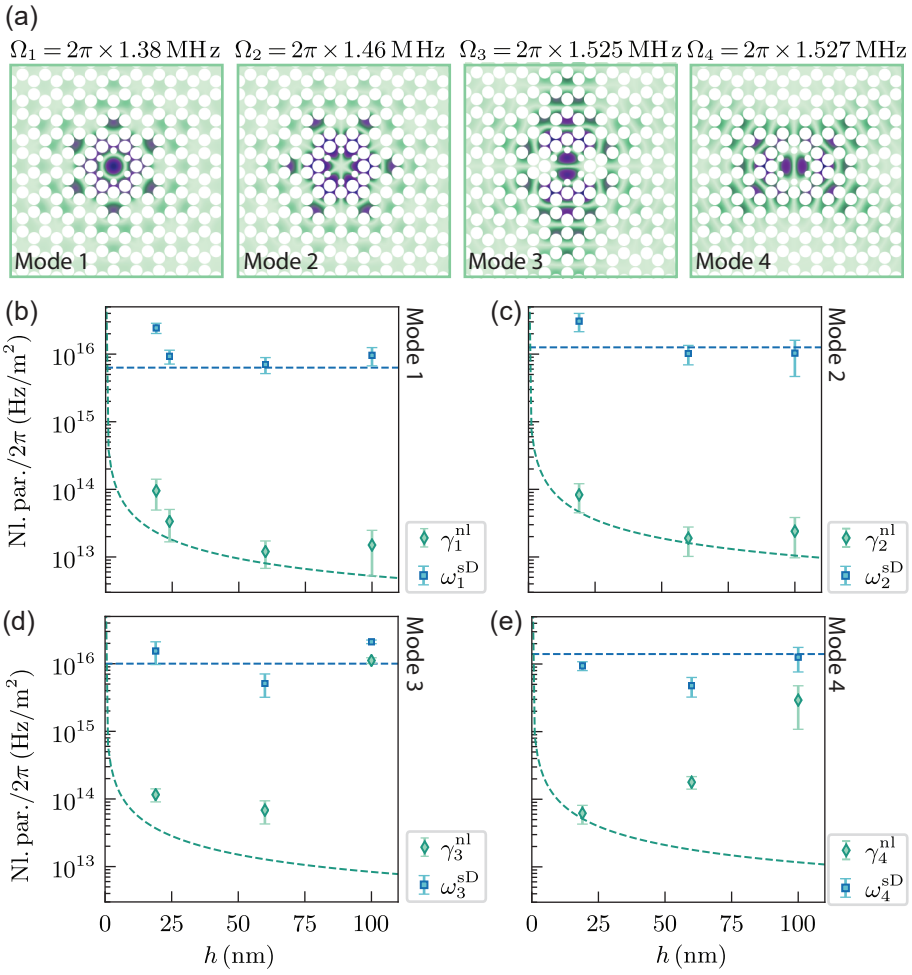

Figure 4.4: Nonlinear parameters. (a) Simulated modeshapes and frequencies of the four bandgap modes considered. (b)-(e) Nonlinear parameters as a function of membrane thickness. Blue squares are Duffing per unit displacement while the green diamonds are the measured nonlinear damping terms. Each point is the median over the fit results of an ensemble of nominally identical membranes. The data on each panel are related to the modeshape listed at the right of the panel. The dashed lines are the nonlinear parameters obtained from FEM simulation.

ringdowns and we average the fit results. As relative errors on the resulting parameters we use the 95 % confidence interval. We discard the fits if the confidence interval exceeds 10 % of the parameter value. We repeat the measurement on ensembles consisting of 6 to 12 nominally identical membranes. Each ensemble is characterized by a different thickness. The complete set of measured nonlinear parameters is shown

in Figs. 4.4 (b)-(e), where instead of β_i we plot the Duffing shift per displacement $\omega_i^{\mathrm{D}} = \beta_i/2\Omega_i$ expressed in unit of $\mathrm{Hz/m^2}$ as the nonlinear damping [CTS20]. Each point is the median of all the extracted values measured on the same mode of all the membranes of a given ensemble. The error bars are estimated through the median absolute deviation. This type of analysis guarantees a more robust estimation due to the presence of few outliers [PGH01]. For the third bandgap mode on two membranes 100 nm-thick we measured a negative Duffing shift. Since we do not understand yet the source of these softening phenomena and we observed some damages on the phononic crystal as well, we decided to discard those data.

Notice that according to Eq. (4.14d) and Eq. (4.14e), β_i and γ_i^{nl} are independent of thickness. The thickness dependence in γ_i^{nl} comes from the time lag τ. Recall that the time delay is related with the intrinsic losses through the loss angle $Q_{\mathrm{intr}}^{-1} = \theta_{\mathrm{lin}} = \tau\Omega_i$ which depends on the resonator thickness. Such dependence can be found in the phenomenological formula in Eq. (1.48). The relation between nonlinear parameters, time lag and intrinsic losses is discussed in more detail in Sec. 4.5.

We compare the measured geometric nonlinearities plotted as green (nonlinear damping) and blue (Duffing shift per displacement) points with the simulated ones plotted as dashed lines is Fig. 4.4 (b)-(e), respectively. To predict the nonlinear parameters we simulate the modes transverse profile using FEM simulations. Then we evaluate ω_i^D and γ_i^{nl} through Eq. (4.14d) and Eq. (4.14e) using the simulated modeshapes. For the first two modes, which we refer to as low-order bandgap modes, we observe a good agreement between measured and simulated values for all the thicknesses. In the high-order bandgap modes, e. g. modes 3 and 4, we observe a good agreement for the Duffing nonlinearity, while the nonlinear damping matches the predictions only for the thinner membranes. For the thicker membranes we observe an excessive nonlinear damping which cannot be modeled through this simple geometrical discussion. We have not understood yet the source of this excessive nonlinear damping. One of our hypotheses is that excessive nonlinear damping is generated by a nonlinear energy exchange mediated by vibrational modes of the supporting frame [Pat+15] or other membrane modes [Ata+16]. In particular, the first hypothesis is supported by the fact that the shielding provided by the phononic crystal is worse for the two high-order bandgap modes [Tsa+17].

4.5 NONLINEAR LOSSES AND DISSIPATION DILUTION

The whole model presented in Sec. 4.2 is based on geometrical considerations. Both the damping and the nonlinear damping are a geometrical manifestations of the same dissipation source. In this chapter we want to look more closely at the relation between the source of dissipation, e. g. the intrinsic losses, and its connection with the nonlinear terms.

The dissipation channel enters in our modeling as a dephasing term in the stress-strain relation ($\theta_{\text{lin}} = \Omega_i \tau = Q_{\text{intr}}^{-1}$). From Eq. (1.23) and Eq. (4.14e), we observe that both the linear (Γ_i) and nonlinear (γ_i^{nl}) damping terms are proportional to the lag time τ. This proportionality matches the expectation, since the two terms are two geometrical expressions of the same dissipation channel. At the same time we notice that, in the context of dissipation dilution (see Sec. 1.3.2 for more details), the linear dissipation is commonly expressed as

$$\Gamma_i = \frac{1}{D_{Q,i}} \frac{\Omega_i}{Q_{\text{intr}}}, \tag{4.34}$$

where $D_{Q,i} \gg 1$ is the dissipation dilution factor and is determined by the geometry of the mode i [Gon00; Ver+07; UFPK10; Sch+11; Tsa+17; Fed+19]. Notice that Q_{intr} coincides with the quality factor of the resonator in the absence of a tensile stress if the intrinsic losses constitutes the dominant source of dissipation. Including a tensile stress in the system we introduce a dissipation dilution factor which leads to a higher measured quality factor:

$$Q_{\text{meas}} = \frac{\Omega_i}{\Gamma_i} = D_{Q,i} Q_{\text{intr}} = D_{Q,i} \theta_{\text{lin}}^{-1}. \tag{4.35}$$

The price to pay to get this increase in the quality factor is that we cannot access the information related to the dissipation dilution factor and the Q_{intr} separately. However, if we look at the nonlinear parameters we notice that neither the Duffing nor the nonlinear damping show a dependence from the tensile stress and, as a consequence, from the dissipation dilution factor. Moreover, we notice that they are characterized by the same dependence on the mode pattern. Therefore, the ratio between the two nonlinear parameters is independent from the mode pattern and is proportional to the time delay τ. In principle such time delay is the same between the linear and the nonlinear damping parameter and the associated loss angles should coincide as well. Because of the uncertainty of such assumption we introduce the so-called *nonlinear loss angle* θ_{nl}, a dephasing term associated with the time delay extracted from the nonlinear parameters, which is expressed as

$$\theta_{\text{nl}} = \Omega_i \tau = \frac{\gamma_i^{\text{nl}} \Omega_i}{2\beta_i}. \tag{4.36}$$

Notably the nonlinear loss angle is expressed in terms of quantities we can all measure experimentally. Moreover, we want to highlight that, despite the dependence of β_i and γ_i^{nl} on the displacement calibration, their ratio is independent of that. The final remark we want to make is that, if the intrinsic losses are our only source of dissipation, the time delay inducing the linear and the nonlinear damping is the same, e. g. the linear and the nonlinear loss angle should coincide

$$\theta_{\text{lin}} = \Omega_i \tau = \theta_{\text{nl}}. \tag{4.37}$$

Therefore, the knowledge of the nonlinear parameters would allow us to indirectly measure the intrinsic losses. Furthermore, by knowing the value of the diluted quality factor we would be able to estimate the dissipation-dilution factor experimentally.

To be able to use the relation between nonlinear parameters and time delay, we need to prove the validity of Eq. (4.37). From our measurement protocol we are able to extract all the parameters needed to evaluate both Q_{meas} and θ_{nl}. Additionally, from Eq. (4.35) we know the relation between Q_{meas} and θ_{lin}. To prove our hypothesis we use the parameters measured through a nonlinear ringdown to plot Q_{meas} against $\theta_{\mathrm{nl}}^{-1}$ (yellow points in Fig. 4.5). From Eq. (1.48) we can deduce the intrinsic

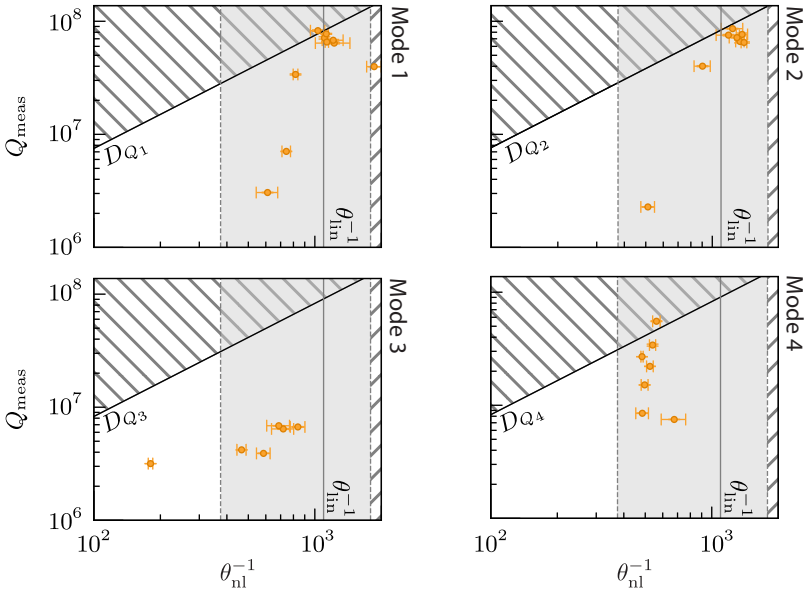

Figure 4.5: Measured quality factors against measure nonlinear loss angles. In each panel we report the data of a single mode listed at the right of the panel. The yellow points are Q_{meas} against $\theta_{\mathrm{nl}}^{-1}$ obtained from 5 ringdown repetitions performed on the same membrane. We are plotting only the data related to the ensemble of 19 nm-thick membranes. The vertical grey line is the expected linear loss angle for S_iN membranes of the considered thickness, while the grey area represents the uncertainty associated with the expected value as reported in [VS14] (for this thickness the grey area corresponds to the uncertainty $\theta_{\mathrm{lin}}^{-1}(19\,\mathrm{nm}) \pm 700$). The black line represents the equality $Q_{\mathrm{meas}} = D_Q \theta_{\mathrm{nl}}^{-1}$, with the dissipation dilution factor obtained from simulation. The hatched area is the region incompatible with the model presented.

linear losses expected for a given sample (vertical line in Fig. 4.5). Due to the phenomenological origin of this formula the uncertainty on that value is large and we represent it as a grey area. We expect the inverse of nonlinear losses to coincides with the inverse of the linear one with fluctuations we can attribute to the variation of the material quality between different fabrication runs. Therefore, if our hypothesis is correct,

the relation $Q_{\mathrm{meas}}^{-1} = D_{Q,i}\theta_{\mathrm{nl}}^{-1}$ should hold. We plot this relation as a diagonal line and it represents an upper bound for the measured quality factor defined by the simulated dissipation dilution factor [Tsa+17].

The ideal situation is represented by all the points falling at the intersection between the simulated dilution factor (diagonal line) and the expected intrinsic quality factor $\theta_{\mathrm{lin}}^{-1}$ (vertical line). Extra losses due to worse material properties or improper handling result in larger loss angle, however the abscissa of those points should move towards the left following the oblique black line. Reduction of the dissipation dilution properties due to imperfections or damages during the fabrication process or additional losses, e. g. gas damping, would reduce the measured quality factor without affecting the intrinsic losses. Hence we expect the measured points to fall in a well-defined region. We highlight the areas where the presence of points cannot be explained by any of those mechanisms as hatched. If the points fall in those areas the relation between Q_{meas} and θ_{nl} does not hold. For the set of membrane 19 nm-thick reported in Fig. 4.5, almost all the points of the ensemble are falling in the expected region. We want to point out that the majority of the points measured for the two low-order bandgap modes lie at the intersection between the grey and the black line, suggesting the validity of our hypothesis.

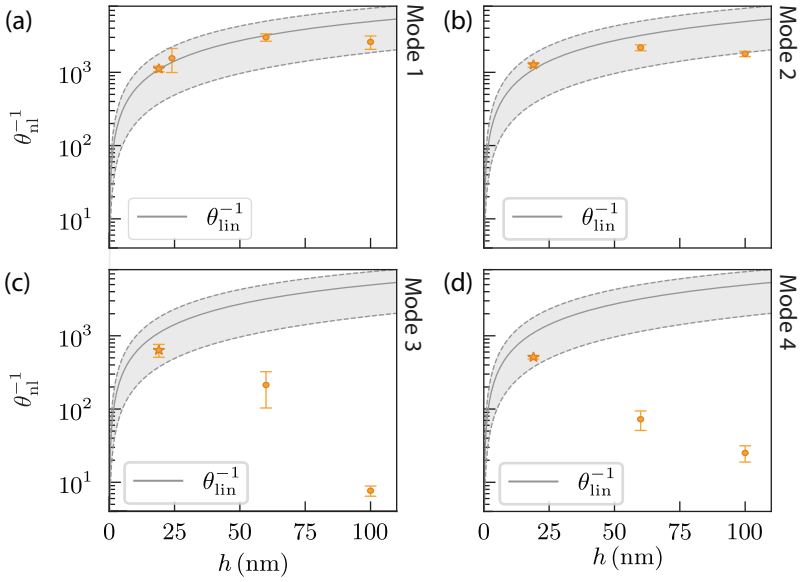

Figure 4.6: Measured nonlinear loss angle as a function of the membrane thickness. In each panel we plot the data from a single modeshape listed at the right of the panel. The grey solid lines represent the expected linear loss angle as a function of membrane thickness and the grey areas is the uncertainty on that value. Each point is the median over all the nonlinear losss angle measured for a single mode on all the membranes of an ensemble with a given thickness. The error bars are the median absolute deviations. The stars represent the median of the points shown in Fig. 4.5.

Next we analyze how the measured nonlinear loss angle changes with the membrane thickness (Fig. 4.7). Each point is the median of all the nonlinear loss angles measured for the same mode on all the membranes of a given ensemble and the error bars are the median absolute value. We compare the data with Eq. (1.48) which describes how the linear loss angle evolves as a function of the thickness. For the two low-order bandgap modes the measurement points follow the phenomenological formula within the uncertainty, corroborating our hypothesis. On the other hand, the two high-order bandgap modes show a dependence on the membrane thickness which we cannot justify with our model. In particular, on the thicker membranes, the two higher-order bandgap modes consistently show high measured nonlinear loss angles corresponding to high measured quality factors, i. e. for those samples the majority of the points fall in the hatched area above the dilution factor line. We attribute this inconsistency with the model to the excess nonlinear damping we discussed in the previous section. In appendix A we show the measured quality factors against $\theta_{\mathrm{nl}}^{-1}$ for all the membranes in each ensembles.

Despite the inconsistency observed in the high-order bandgap modes, the data match the prediction for the two low-order bandgap modes suggesting that the proposed relation between geometric nonlinearities and intrinsic losses is valid for those two geometries. We now discuss the last set of measurements performed to support our hypothesis. It consists in characterizing the intrinsic losses at different temperatures. We realize it only on the first bandgap mode of a 19 nm-thick membrane.

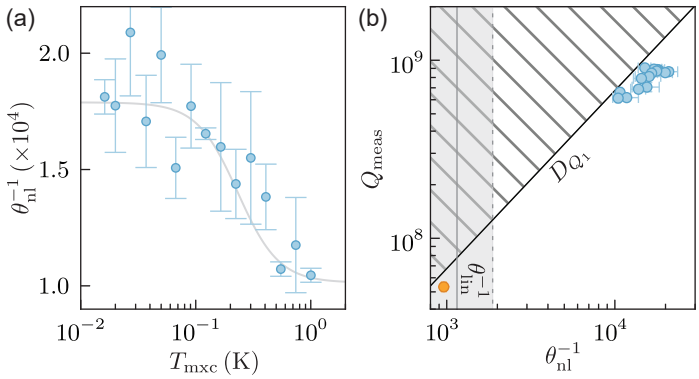

Figure 4.7: Nonlinear loss angle as a function of temperature. (a) Measured $\theta_{\mathrm{nl}}^{-1}$ as a function of the dilution fridge temperature, T_{mxc}. The grey line is a polynomial fit, roughly showing the behavior. (b) Measured quality factors against measured nonlinear loss angle, taken at room temperature (yellow) and cryogenic temperatures (blue). The grey line is the expectation value of $\theta_{\mathrm{lin}}^{-1}$ at room temperature, and the grey area reflects uncertainty on this value. The black line is the simulated dissipation dilution factor. Error bars are the mean absolute deviation among 3 repetitions.

We place one of the membranes belonging to the ensemble of the selected thickness in a dilution refrigerator. With a similar setup working at

a wavelength of 830 nm we perform a set of ringdown measurements varying the temperature from 20 mK to 1 K. Details on the type dilution fridge are not relevant for this thesis work, but are reported in [Sei21]. We observe that the membrane experiences a heating process due to optical absorption [Pag+21; Ros20]. To minimize the heating process we use an optical power of 100 nW. In Fig. 4.7 (a) we plot the measured quality factor against the mixing chamber temperature. As it is also reported in [YCS15; Fau+14; Fis+16; Pag+21], the quality factor increases as the temperature decreases until it reaches a plateau. The measured quality factor saturates around 10^9 suggesting the presence of additional linear undiluted losses. In Fig. 4.7 we plot the measured quality factors against the measure nonlinear loss angles. The yellow point has been measured at room temperature. We observe that the nonlinear loss angle decreases with the temperature reduction, however the ratio between Q_{meas} and θ_{nl} is constant, consistent with our hypothesis.

5

COUPLED HARMONIC OSCILLATORS

Coupled micro- and nanomechanical resonators attract a lot of attention in a variety of technological applications. The high quality factors of nanomechanical devices and the possibility of interface them with different types of systems make them promising platform for force sensing experiment and mechanically mediated transduction. In this chapter we discuss how to implement the concepts of coupled harmonic oscillators with all the advantages of the soft-clamped resonators. We start discussing the simple case of two point-like harmonic oscillators coupled with each other. Then we introduce a new phononic dimer geometry, consisting of soft-clamped membrane with two defects embedded in the same phononic crystal. This geometry can be intuitively described as two defect oscillators coupled through the common substrate. We characterize the geometrical dependence of the normal mode splitting and the force sensitivity, both essential for force sensing applications. Finally we use the theoretical results and the experimental protocol developed in the previous chapter to study the dynamics of this new geometry in the large displacement amplitude regime. We measure the Duffing nonlinearity and the nonlinear damping for different dimers resonator and we compare them with the simulated values. Additionally, we observe the presence of cross-nonlinear phenomena that we phenomenologically model starting from the equation of motion of two damped harmonic oscillators in the large displacement amplitude regime.

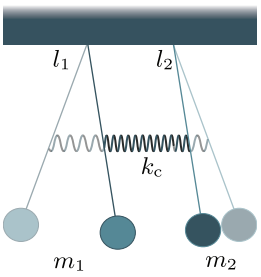

Coupled simple pendula.

5.1 LINEAR COUPLED HARMONIC OSCILLATORS

We define two harmonic oscillators to be coupled with each other when they are connected in such a way that there is an energy transfer between them. To mention a few examples, they can be constituted by two simple pendula connected by a spring, two extended objects, such as cantilevers or doubly clamped beams elastically coupled through a common mechanical ledge [KCR09], or magnetically coupled through external fields [LLA10], or even resonators consisting of vacancies in phononic structures coupled by the common substrate [MIC14; CTS20; Ber+21]. We want to start the discussion of coupled harmonic oscillators already in the lumped-element description.

Let us consider two linear oscillators coupled with each other. We call u_n (u_m) the displacement of the first (second) mode with respect to its equilibrium position. We assume the two harmonic oscillators to be identical with same mass m, elastic constant k and damping rate Γ. The equation of motion describing the two oscillators is

$$m\ddot{u}_m + \Gamma m\dot{u}_m + ku_m - k_c u_n = 0, \tag{5.1a}$$
$$m\ddot{u}_n + \Gamma m\dot{u}_n + ku_n - k_c u_m = 0, \tag{5.1b}$$

where k_c is the coupling constant and the last term on the left hand side of the equation is the strength of the coupling force. For simplicity we are not considering any external force applied to the resonators. We can decouple the two equations considering the sum and difference of Eqs. (5.1a) and (5.1b) moving to the new coordinate system:

$$u_S = u_m + u_n, \tag{5.2a}$$
$$u_A = u_m - u_n. \tag{5.2b}$$

After applying the transformation above we obtain the following:

$$\ddot{u}_S + \Gamma\dot{u}_S + \Omega_S^2 u_S = 0, \tag{5.3}$$
$$\ddot{u}_A + \Gamma\dot{u}_A + \Omega_A^2 u_A = 0, \tag{5.4}$$

where $\Omega_S^2 = (k - k_c)/m$, and $\Omega_A^2 = (k + k_c)/m$. The oscillations of the individual oscillators hybridize when we include the coupling constant. As a result, the coupled systems start a joint harmonic motion characterized by two new modes. From Eqs. 5.2 we recognize that the new modes are constituted by the in-phase u_S and the out-of-phase u_A motion of the coupled oscillators. We refer to them as the symmetric and the antisymmetric mode, respectively. The two modes are characterized by different resonant frequencies, Ω_S and Ω_A, that we can resolve only if the difference between the two, i. e. the normal mode splitting, is larger than the modes damping rate Γ.

In the more general case of two oscillators with different masses $m_{m,n}$ and elastic constants $k_{m,n}$ the equations of motions are not as easy to decouple. Nevertheless we can still find a solution to the problem using a slightly different approach. To simplify the problem, we do not include the contribution of the damping terms. Within these conditions Eq. (5.1) can be written in matrix form as:

$$\begin{pmatrix} m_m & 0 \\ 0 & m_n \end{pmatrix} \begin{pmatrix} \ddot{u}_m \\ \ddot{u}_n \end{pmatrix} + \begin{pmatrix} k_m & -k_c \\ -k_c & k_n \end{pmatrix} \begin{pmatrix} u_m \\ u_n \end{pmatrix} = 0, \tag{5.5}$$

where the first matrix is the mass matrix M and the second is the spring matrix K. To find the solution of Eq. (5.5) we substitute u_n and u_m with the harmonic test functions $A_n e^{i\Omega t}$ and $A_m e^{i\Omega t}$, respectively. We find the frequencies of the new modes by solving the eigenvalue problem

$$K \begin{pmatrix} u_m \\ u_n \end{pmatrix} = \Omega^2 M \begin{pmatrix} u_m \\ u_n \end{pmatrix}. \tag{5.6}$$

Notice that for identical masses and elastic constants we recover the solution obtained through the first method.

5.2 SOFT-CLAMPED PHONONIC DIMERS - LINEAR CASE

We want to realize a device analogous to two coupled harmonic oscillators with all the advantages provided by the dissipation dilution and the soft clamping techniques [CTS20]. We implement this idea by introducing a second defect in the phononic crystal structure. We use as starting membrane design a Dahlia generation 1. In this section we give a phenomenological description of this design where we treat the two defects as two individual oscillators and we use the elastic equation to derive the coupling constant between the two. Then we discuss the device characterization and the measurement of the linear properties.

5.2.1 *Device principle and dimerization*

To understand what enables the coupling mechanisms in our highly stressed resonator we start writing the simplified elastic equation of motion for the out-of-plane displacement field:

$$\sigma_0 \nabla \cdot \nabla w = \rho \ddot{w}, \tag{5.7}$$

which coincides with Eq. (1.8a) when we neglect the damping term, we keep only the dominant conservative term proportional to the tensile stress, and we do not include any external force. Similarly to the procedure described in Sec. 1.2.3, we expand $w(x, y, t)$ on a basis of out-of-plane eigenmodes ϕ_n associated with the out-of-plane displacement u_n

$$\sigma_0 u_n \nabla \cdot \nabla \phi_n = \rho \ddot{u}_n \phi_n, \tag{5.8}$$

where the repeated indexes are summed over. At this point we apply the Galerkin method [You11] on the above equation and we obtain the following equation:

$$\sigma_0 u_n \int_S \nabla \phi_m \nabla \phi_n dS = \rho \ddot{u}_n \int_S \phi_m \phi_n dS. \tag{5.9}$$

ϕ_m is the test function and usually corresponds to an eigenmode, and to write the first term on the left hand side we used the divergence theorem (Eq. (1.20)). To simplify the calculation we consider a spatial-independent tensile stress. From Eq. (5.8) we write the effective spring and mass matrices for a highly stressed membrane:

$$K_{nm} = \sigma_0 \langle \nabla \phi_m | \nabla \phi_n \rangle, \tag{5.10a}$$

$$M_{nm} = \rho \langle \phi_m | \phi_n \rangle, \tag{5.10b}$$

where $\langle \cdot \rangle$ represents the integral over the surface. Substituting Eq. (5.10) we recover the eigenvalue problem that we can use to determine the

resonance frequencies of the various membrane modes. In the particular case of a soft-clamped membrane we can think of ϕ_n and ϕ_m as the eigenmodes of the central defect. Usually we derive the spatial profile of this modes through FEM simulations [Tsa+17].

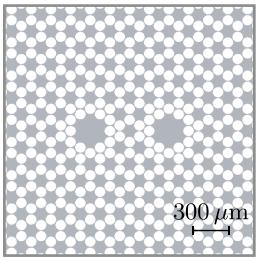

Phononic dimer.

Let us now introduce a second defect in the phononic crystal. The new system is characterized by a new set of eigenmodes delocalized on both the defects. The frequencies of the normalized mode can be predicted through Eq. (1.24) by using the new, hybridized modeshapes. However, to give an intuitive description on how the bandgap modes are modified with respect to the single defect case, we build a phenomenological model treating the two defects as two separate oscillators vibrating one next to the other. We call ϕ_1 a mode of one defect in the absence of the second and we associate it with the time dependent displacement u_1, while we call ϕ_2 a mode of the second defect in the absence of the first associated with the time dependent displacement u_2. We assume the two defects to be identical, therefore the mode ϕ_1 and ϕ_2 vibrates with the same frequency Ω. Then we assume that the effective spring and mass matrices of the system are described by Eq. (5.10). Within this assumptions the eigenvalue problem reduces to

$$K_{11}u_1 + K_{12}u_2 = \Omega^2(M_{11}u_1 + M_{12}u_2), \tag{5.11a}$$
$$K_{21}u_1 + K_{22}u_2 = \Omega^2(M_{21}u_1 + M_{22}u_2). \tag{5.11b}$$

For two identical defects and ϕ_1 and ϕ_2 describing the same bandgap mode, we have that $K_{12} = K_{21}$, $K_{11} = K_{22}$, $M_{12} = M_{21}$ and $M_{11} = M_{22}$. Within these conditions Eq. (5.11) coincides with the eigenvalue problem of the system described in Eq. (5.1). The coupling term is represented by:

$$K_{12} = \sigma_0\langle\nabla\phi_1|\nabla\phi_2\rangle. \tag{5.12}$$

The only difference with respect to the simple case in Sec. 5.1 is the presence of non-zero off-diagonal elements in the effective mass matrix which coincides with the overlap integral between the two defects modes.

We can decouple Eq. (5.11) performing the transformation in Eq. (5.2). After some algebra we find two equations for the new displacements u_S and u_A associated with two hybrid modes ϕ_S and ϕ_A, describing the out-of-plane displacement profiles of the two coupled defects. From the

solution of the eigenvalue problem for the new variables we find the new frequencies:

$$\Omega_{\mathrm{S}} = \sqrt{\frac{K_{11} + K_{12}}{M_{11} + M_{12}}} \tag{5.13a}$$

$$\Omega_{\mathrm{A}} = \sqrt{\frac{K_{11} - K_{12}}{M_{11} - M_{12}}} \tag{5.13b}$$

In the limit of weak coupling ($K_{12} \ll K_{11}$ and $M_{12} \ll M_{11}$) we can approximate the modeshapes of the double-defect structure with the following expressions [MIC14]:

$$\phi_{\mathrm{S}} \approx \phi_1 + \phi_2, \tag{5.14a}$$

$$\phi_{\mathrm{A}} \approx \phi_1 - \phi_2. \tag{5.14b}$$

Hence the presence of the coupling term between the two defects motion generates two hybrid modes delocalized on both the defects oscillating in-phase (ϕ_S) and out-of-phase (ϕ_{A}). The frequency splitting between the two hybrid modes in the weak coupling approximation can be predicted from the modeshape of the single defect using the following expression

$$\frac{\Omega_{\mathrm{A}} - \Omega_{\mathrm{S}}}{\Omega} \approx \frac{M_{12}}{M_{11}} - \frac{K_{12}}{K_{11}}, \tag{5.15}$$

where we performed an expansion to the first order in K_{12}/K_{11} and M_{12}/M_{11}.

A similar linear combination approach is often used to describe the combination of atomic orbitals in dimer molecules, therefore we named this geometry *a phononic dimer*.

5.2.2 *Linear characterization*

In this section we experimentally characterize the phononic dimer structure. At first, we want to verify the accuracy of the simulated eigenfunctions. We are only interested in the symmetric and antisymmetric modes generated from the first bandgap mode of a single defect. On a 14 nm-thick membrane we realize a raster scan to image the symmetric and antisymmetric mode (Fig. 5.1 (a)). The x-y map of the two modeshapes has been realized with a free space Mach-Zehnder interferometer with a homodyne detection scheme operated at 1064 nm, similar to the one described in Sec. 3.1. Details about the measurement procedure can be found in [Bar+16]. We compare the measured modeshapes with the one obtained through FEM simulations (see Fig. 5.1 (b)) finding a good agreement. Finally, we show the parity of the two modes by plotting the cross-section of the simulated modeshapes (Fig. 5.1 (c)).

One of the main advantages of this structure is that we can tune the coupling, and the frequency splitting between the symmetric and

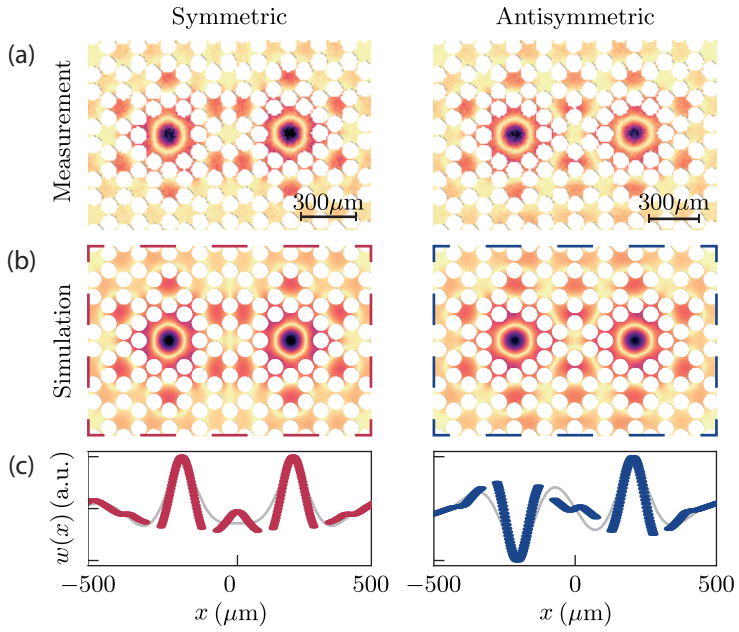

Figure 5.1: Soft-clamped phononic dimer. (a) Measured out-of-plane displacement of the phononic dimer symmetric (left) and antisymmetric (right) modes. The left mode is the symmetric, the right mode is the antisymmetric. (b) Simulated out-of-plane desiplacement of the symmetric (left) and antisymmetric (right) mode. (c) Simulated cross-section of the symmetric (left) and antisymmetric (right) mode. The red (blue) points represent the simulated displacement for the symmetric (antisymmetric) mode, the grey line is the addition (subtraction) of two exponential decays with an oscillating component.

antisymmetric mode, by changing the overlap between the two single defect mode curvatures (see Eq. 5.12). We can act on the curvature superposition by varying the relative positions of the defects within the phononic crystal. We have two main parameters we can change: the relative distance between the defects (d_{sep}) and their relative angle with respect to the phononic crystal (θ). The two parameters are depicted in Fig. 5.2. The angles and the dimer separations cannot be varied continuously. The phononic crystal symmetry allows us to realize dimer structures with orientations $\theta = [0°, 13.91°, 30°, 46.1°]$ and separations corresponding to $d_{\text{sep}} = [0, 1, 2, 3]$ unit cells. We could explore weaker coupling and maybe reach a distance so large that the two defects do not interact anymore increasing the number of unit cells. This requires to increase the membrane side length. To guarantee a good isolation from the frame, we usually fabricate the membrane in such a way that there are 9 unit cells between the defect and the frame. To maintain this distance on all the sides of each defect we need to increase the membrane size. However, the larger the size gets, the more fragile the membrane becomes, i. e. the fabrication yield reduces. We report a table with the corresponding outer dimension in Appendix B.

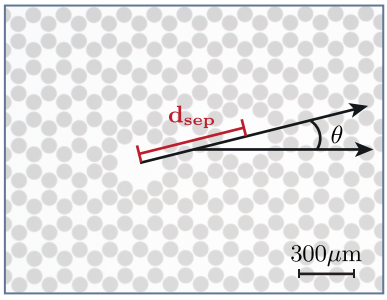

Figure 5.2: Micrograph of a soft-clamped phononic dimer. In black and red we highlight the orientation θ and the dimer separation d_{sep}, respectively.

We fabricate a set of membranes 14 nm-thick, with the orientations and separations listed above. For each geometry we fabricate three samples. We then measure the frequency splitting on all of the fabricated devices through the FFT of the photocurrent and we compare them with the simulated values (see Fig. 5.3 (b)). Within the geometries under study, we measure a normal mode splitting varying from 2 kHz to 100 kHz. Interestingly, we observe a consistent effect due to the orientation. In particular in Fig. 5.3 (a) we show the spectra measured on different membranes characterized by $d_{\text{sep}} = 1$ unit cell with varying orientations θ.

It is interesting to notice that for some of the measured geometries the frequency of the symmetric and antisymmetric mode is inverted, i. e. the antisymmetric mode is associated with the lower frequency. This phenomenon takes place for all the geometries characterized by an orientation $\theta = 30°$ as well as in the geometry characterized by the orientation $\theta = 0°$ and dimer separation $d_{\text{sep}} = 3$ unit cells. Looking at the derivation performed in Sec. 5.1 this might be counter-intuitive. To understand this observation, it is instructive to compare the displacement profiles of two configurations showing opposite behavior. In particular we consider the geometry $\theta = 0°$ and $d_{\text{sep}} = 1$ unit cell, where the lower frequency mode coincides with the symmetric mode, and the geometry $\theta = 30°$ and $d_{\text{sep}} = 1$ unit cell, where the lower frequency mode coincides with the antisymmetric. We first simulate the modeshapes for the two individual defects in the two cases, Fig. 5.4 (a) and Fig.5.4 (c). Then, we plot the out-of-plane displacement along the line representing the orientation of interest, black dashed line in Fig. 5.4 (a) and Fig.5.4 (c). Comparing the normalized displacement profile of the left mode with the the normalized displacement profile of the right mode with opposite signs, we observe that for $\theta = 0°$ the left and the right defect displacements are largely in-phase for the symmetric combination (see Fig. 5.4 (b)). Recall that we define ϕ_i as normalized mode satisfying the condition $\phi_i^{\max} = 1$. On the other hand, for $\theta = 30°$ the left defect and the right defect displacements are largely in-phase for instead the antisymmetric combination (see Fig. 5.4 (d)). Therefore

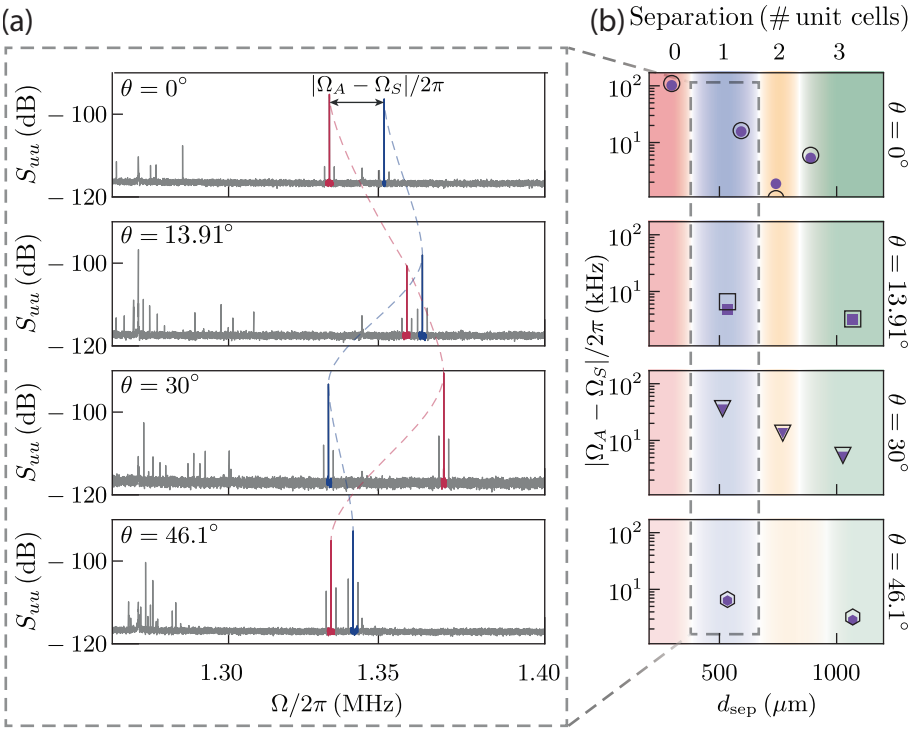

Figure 5.3: Geometrical dependence of the normal mode splitting. (a) Thermomechanical wide spectra for the four possible orientations of the phononic dimers characterized by $d_{\text{sep}} = 1$ unit cell. The red peaks are the symmetric modes, the blue peaks the antisymmetric ones. The dashed lines are a guide to the eye to emphasize the order swap between symmetric and antisymmetric mode. The satellite peaks around the modes are induced by the turbo pump vibrations. (b) Frequency splitting for all the orientations and all the separations. The filled symbols are the measured values, the empty symbols the simulated ones. The same number of unit cells separation on different orientations can correspond to a slightly different distance between the two defects. The different colors highlight the range of distances corresponding a given number of unit cells.

we are naming the two modes as symmetric and antisymmetric based on the maximum displacement point symmetry, however the frequency order is defined by the overall modeshapes superposition.

This membrane design is particularly interesting for force sensing applications due to the large working area represented by the two defects. As a matter of fact, the presence of two defects simplify the spatial separation between the region where we apply the force we want to detect and the optical readout of the induced vibration [H+̈21b]. For such applications the quality factor and the effective mass are two crucial parameters. Therefore, we move to characterize them. We measure the quality factor through a ringdown technique introduced in Sec. 1.2.4. We perform the measurement on all the geometries extracting the value over 5 ringdown repetitions. We average the results obtained from all

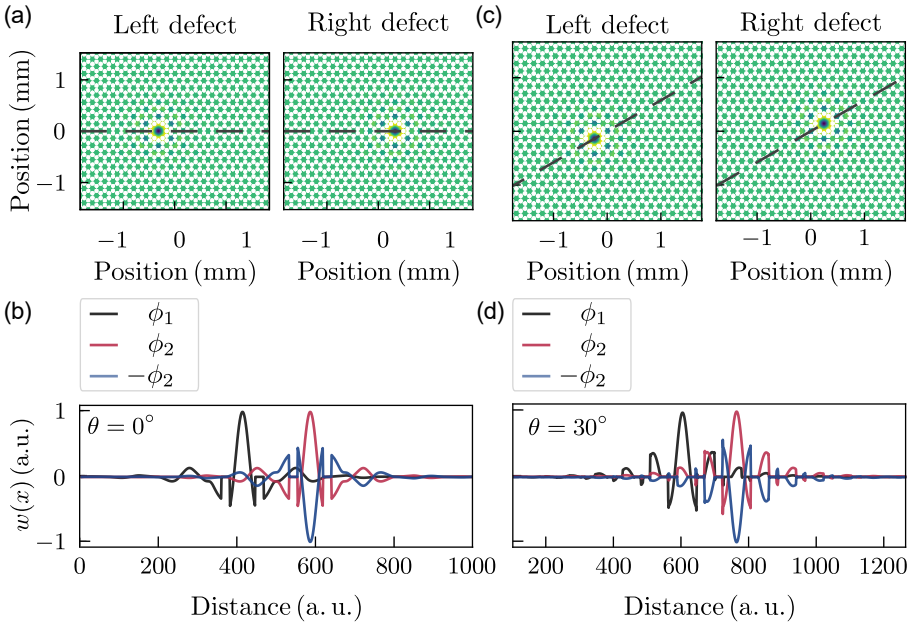

Figure 5.4: Comparison of the simulated out-of-plane displacements of the two individual defects for different geometries. (a) Simulated out-of-plane displacement of two individual defects (one for each panel) for the geometry $\theta = 0°$ and $d_{\text{sep}} = 1$ unit cell. The black dashed line connects the two defects center and represents the orientation. (b) Cross-sectional view of the defects displacement along the dashed line in (a). The black line is the left defect cross-section. The red and blue lines are the right defect cross-section with opposite signs. (c) Simulated out-of-plane displacement of two individual defects (one for each panel) for the geometry $\theta = 30°$, $d_{\text{sep}} = 1$ unit cell. The black dashed line connects the two defects center and represents the orientation. (d) Cross-sectional view of the defects displacement along the dashed line in (c). The black line is the left defect cross-section. The red and blue lines are the right defect cross-section with opposite signs.

the nominally identical membrane fabricated. In Fig. 5.5 we report the measured quality factors for all the geometries of interest and we compare them with FEM simulation. Details on the simulation of the quality factor can be found in [Tsa+17].

We then move to evaluate the effective masses. We use the simulated eigenmodes and we use them to calculate the effective mass through Eq. (1.22). In Table 5.1 we report simulation results for all the geometries studied in this section. As expected, for the majority of the geometries the effective mass of the hybridized modes is approximately twice the effective mass associated with a single defect [Tsa+17], consistent with Eq. (5.14). However, when the dimer separation becomes small, the simulated effective masses deviates from the ones expected from Eq. (5.14), suggesting a stronger mixing in the modeshapes. We try to validate the simulations performing a measurement of the effective mass.

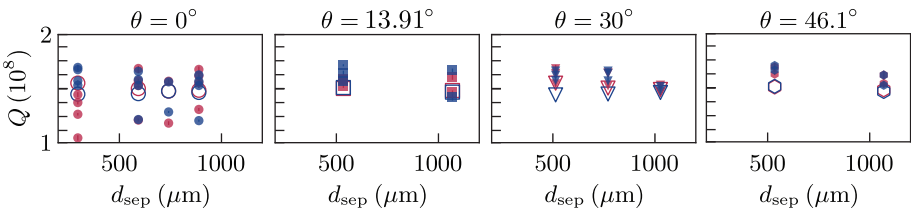

Figure 5.5: Quality factor for all the orientation as a function of the dimer separation. Filled red (blue) points represent the measured quality factor for the symmetric (antisymmetric) mode. The empty red (blue) points the simulated value for the symmetric (antisymmetric) mode. Each symbol coincides with the orientation listed above the panel.

θ	0 unit cells		1 unit cell		2 unit cells		3 unit cells	
	$m_{\text{eff,S}}$	$m_{\text{eff,A}}$	$m_{\text{eff,S}}$	$m_{\text{eff,A}}$	$m_{\text{eff,S}}$	$m_{\text{eff,A}}$	$m_{\text{eff,S}}$	$m_{\text{eff,A}}$
0°	2.6	1.8	1.9	1.7	1.7	1.9	1.9	1.8
13.91°	–	–	1.7	2.0	–	–	1.8	1.9
30°	–	–	1.7	2.0	1.8	1.8	1.9	1.8
46.1°	–	–	1.7	2.0	–	–	1.8	1.9

Table 5.1: Simulated effective masses for all the fabricated geometries. The numbers are expressed in nanograms. For the simulation we assume a membrane 14 nm-thick and a material density of $\rho = 3200\ \text{kg/m}^3$.

We accurately align our interferometer with the expected maximum displacement point. We leave the mode of interest in its thermal state and we acquire the two mechanical quadratures for approximately 15 minutes. We divide the time-trace in shorter traces of 1 minute and we perform the FFT on the acquired data. To evaluate the effective mass we need to calibrate the measured spectra. In this particular case, since the effective mass is the parameter to be measured, we perform the relative displacement calibration described in Sec. 3.3.2. Once we obtain the calibrated spectra, we numerically evaluate the areas under them. Then we use the relation in Eq. (3.7) to evaluate the effective mass on each spectrum and we average the results. Simultaneously, we save the two quadratures of the carrier beat note to compensate for interferometer phase drifts and fluctuations in the light intensity. We perform the measurement only on the geometry characterized by $\theta = 13.91°$, $d_{\text{sep}} = 1$ unit cell. We identify this configuration as the most interesting for force sensing applications because it is characterized by a frequency splitting of the order of 7 kHz. This frequency match the possible spin-flip frequencies and is particularly interesting for the implementation of a parametric protocol for an MRFM experiment [Koš+20] involving the use of our phononic dimer geometry. The measured effective masses for the two modes are $m_{\text{S}} = 3\,\text{ng}$ and $m_{\text{A}} = 4\,\text{ng}$. The discrepancy between

the simulated and the measured values is probably due to an imperfect overlap between the optical and the mechanical mode. Considering the accuracy with which we can simulate the frequency, and the limited control on beam spot dimension and alignment in our setup, we believe the simulated data are more accurate for this type of information.

From the linear properties of our devices, we can estimate the force sensitivity $\sqrt{S_{\mathrm{FF}}}$ using Eq. (1.37). Using the measured quality factor and the simulated effective mass, we evaluate the force noise at room temperature for the symmetric, $\sqrt{S_{\mathrm{FF_S}}} = 28.2\,\mathrm{aN}/\sqrt{\mathrm{Hz}}$, and the antisymmetric mode, $\sqrt{S_{\mathrm{FF_A}}} = 29.9\,\mathrm{aN}/\sqrt{\mathrm{Hz}}$, of the geometry with $\theta = 13.91°$ and $d_{\mathrm{sep}} = 1$ unit cell. To reduce the force noise contribution, the force sensing experiments are usually performed at cryogenic temperature. Beside the temperature reduction we observe an increase in the quality factor at cryogenic temperature, see Fig. 4.7 or [Ros20; Pag+21; Sei21]. Assuming an increase of a factor 3 on the quality factor and a temperature of 4 K, the projected force sensitivities for the two modes are $\sqrt{S_{\mathrm{FF_S}}} = 1.9\,\mathrm{aN}/\sqrt{\mathrm{Hz}}$ and $\sqrt{S_{\mathrm{FF_A}}} = 2.0\,\mathrm{aN}/\sqrt{\mathrm{Hz}}$.

5.3 NONLINEAR COUPLED HARMONIC OSCILLATORS

In the first section we opened the discussion with two harmonic oscillators interacting through a coupling term (k_{c}) and explained how we decouple them by moving to the new coordinate system of the symmetric and antisymmetric mode. In this section, we want to perform the same derivation by including the contribution of the geometric nonlinear terms introduced in Chapter 4.

We start writing the equation of motion for two nonlinear oscillators coupled together through a coupling term k_{c}. We assume two identical oscillators with the same mass, frequency, damping and nonlinear parameters. Following the formalism in Sec. 5.1, we use the subscript n for one oscillator and m for the other. The two new coupled equations take the form:

$$\ddot{u}_m + (\Gamma + \gamma^{\mathrm{nl}} u_m^2)\dot{u}_m + (\Omega^2 + \beta u_m^2)u_m - \frac{k_{\mathrm{c}}}{m}u_n = 0, \tag{5.16}$$

$$\ddot{u}_n + (\Gamma + \gamma^{\mathrm{nl}} u_n^2)\dot{u}_n + (\Omega^2 + \beta u_n^2)u_n - \frac{k_{\mathrm{c}}}{m}u_m = 0. \tag{5.17}$$

We want to write the two equations of motion in term of the new variable u_{S} and u_{A} derived in the linear case. To do so, we substitute u_n and u_m through the transformation in Eqs. (5.2). Then we sum and subtract the resulting equations. After some algebra we end up with the following equations of motion for the new variables:

$$\ddot{u}_i + \Gamma\dot{u}_i + \frac{\gamma^{\mathrm{nl}}}{4}\left(u_i^2 + u_j^2 + 2u_iu_j\right)\dot{u}_i + \Omega_i^2 u_i + \frac{\beta}{4}(u_i^3 + 3u_iu_j^2) = 0, \tag{5.18}$$

where $i, j \in [\mathrm{S}, \mathrm{A}]$ with $i \neq j$ and $\Omega_i = (k \mp k_{\mathrm{c}})/m$.

From the above equation we immediately notice that the change of variables doesn't lead to decouple equations. Additionally, the new cross-terms are connected with the nonlinear parameters we introduced in chapter 4. To distinguish between the nonlinear terms depending only on the mode of interest and the one resulting from a correlation between the two modes we will refer to them as *self-nonlinear terms* (β_i^{s} and γ_i^{snl}) and *cross-nonlinear terms* (β_i^{x} and γ_i^{xnl}), respectively.

The derivation above is a simplistic description giving an intuitive explanation of the presence of cross-nonlinear terms in the equation of motion. More formally, we could derive these extra nonlinear terms for a membrane resonator starting from elasticity equations including an intermodal coupling contribution. This can be generalized to all the combination of modes in a membrane resonators. Nevertheless, for dimer resonators we expect an overlap between the symmetric and antissymmetric mode leading to cross-nonlinearities more pronounced with respect to other pairs of modes. Examples of cross-nonlinearities in pairs of modes with opposite symmetry have been observed in a variety of resonators [MIC14; KCR09; Wes+10].

We describe the dynamics of the pairs of modes with opposite symmetry with the following generalized equations of motions:

$$\ddot{u}_i + (\Gamma_i + \gamma_i^{\mathrm{snl}} u_i^2 + \gamma_{ji}^{\mathrm{xnl}} u_j^2 + \gamma_{ij}^{\mathrm{xnl}} u_j u_i)\dot{u}_i + (\Omega_i^2 + \beta_i^{\mathrm{s}} u_i^2 + \beta_{ji}^{\mathrm{x}} u_j^2) u_i = 0 \tag{5.19}$$

where we included two phenomenological cross-nonlinear terms. Ω_{S} and Ω_{A} coincide with Eqs. (5.13), and β_i^{S} and γ_i^{snl} can be evaluated knowing the modeshapes using Eq. (4.14d) and Eq. (4.14e), respectively. On one hand, we want to understand how the nonlinearities affect the dynamics of the system. On the other, we want to quantify the strength of such nonlinear effects in our structure.

To simplify the problem we distinguish two regimes where we can characterize the self-and the cross-nonlinearities separately. From the the model in Sec. 4.2 we know that the contribution of the geometric nonlinearities start to be relevant for displacement comparable with the membrane thickness. From the simplistic model above, we can deduce that the contribution of the cross-nonlinear terms starts to be relevant under the same condition. If we apply an external driving force such that we only drive one of the two modes in the nonlinear regime, we can remove the contribution of only one type of nonlinearities at the time. In the following we analyze the solution of the equations in two limiting cases: negligible cross-nonlinearities and negligible self-nonlinearities.

Nl. Dampings	Value (2π Hz)	Duffings	Value ($4\pi^2$ Hz^2)
$\gamma_i^{\mathrm{snl}} u_i^2$	10^{-1}	$\beta_i^{\mathrm{s}} u_i^2$	10^7
$\gamma_{ji}^{\mathrm{xnl}} u_j^2$	10^{-7}	$\beta_{ji}^{\mathrm{x}} u_j^2$	10
$\gamma_{ij}^{\mathrm{xnl}} u_j u_i^2$	10^{-4}		

Table 5.2: Self- and cross-nonlinear components contribution in the equation of motion for $u_j \ll u_j$. We assume $u_i \approx 10\,\mathrm{nm}$ and $u_j \approx 10\mathrm{pm}$. On the left side hand side of the table we write the values of the terms proportional to the self- and the cross- nonlinear damping terms, on the right hand side we write the values of the terms proportional to the self- and cross-duffing nonlinearities.

Case 1: self-nonlinearities

In the first case, we resonantly drive the mode i up to the nonlinear regime, we leave the mode j in its thermal state, i. e. $u_j \ll u_i$. We focus on the dynamics of the mode i. We consider a displacement of the mode i and of the mode j to be $u_i \approx 10\,\mathrm{nm}$ and $u_j \approx 10\,\mathrm{pm}$. Then we assume the cross-nonlinearites to be of the same order of magnitude of the simulated self-nonlinearities, i. e. $\gamma_i^{\mathrm{snl}} \approx \gamma_{ij}^{\mathrm{xnl}} \approx \gamma_{ji}^{\mathrm{xnl}} \approx 2\pi\, 10^{14}\,\mathrm{Hz/m^2}$, and $\beta_i^{\mathrm{s}} \approx \beta_{ji}^{\mathrm{x}} \approx 4\pi^2\, 10^{22}\,\mathrm{m^{-2}s^{-2}}$. Within these conditions, the order of magnitude of the different components of the equation of motion are reported in Table 5.2.

We remark that all the cross-terms $\propto u_j$ are negligible with respect to the self-nonlinear terms. By neglecting the contribution of the cross-nonlinear terms, the new equation does not include any coupling term with the mode j and coincides with Eq. (4.13). From the discussion in Sec. 4.3, we know that the self-nonlinearities introduce an amplitude-dependent damping term in the amplitude decay, and a resonance frequency shift proportional to the displacement amplitude squared. Using the laws describing the nonlinear amplitude decay and the resonance frequency shift, we can measure the self-nonlinear parameters in these samples as well.

Case 2: cross-nonlinearities

In the second case, we resonantly drive the mode j up to the nonlinear regime, and we leave the mode i in its thermal state (or in the linear regime), i. e. $u_j \gg u_i$. We again focus on the equation of motion describing the dynamics of the mode i. This time we consider a displacement of the mode i and of the mode j to be $u_i \approx 10\,\mathrm{pm}$ and $u_j \approx 10\,\mathrm{nm}$ respectively, and we assume the self- and cross-nonlinearities to be of the same order of the previous case. The order of magnitude of the different components of the equation of motion are reported in Table 5.3. From the values reported in Table 5.3, we notice that all the terms

Nl. Dampings	Value (2π Hz)	Duffings	Value ($4\pi^2$ Hz^2)
$\gamma_i^{\mathrm{snl}} u_i^2$	10^{-7}	$\beta_i^{\mathrm{s}} u_i^2$	10
$\gamma_{ji}^{\mathrm{xnl}} u_j^2$	10^{-1}	$\beta_{ji}^{\mathrm{x}} u_j^2$	10^7
$\gamma_{ij}^{\mathrm{xnl}} u_j u_i^2$	10^{-4}		

Table 5.3: Self- and cross-nonlinear components contribution in the equation of motion for $u_j \gg u_i$. We assume $u_i \approx 10\,\mathrm{pm}$ and $u_j \approx 10\mathrm{nm}$. On the left side hand side of the table we write the values of the terms proportional to the self- and the cross- nonlinear damping terms, on the right hand side we write the values of the terms proportional to the self- and cross-duffing nonlinearities.

$\propto u_i^2$, u_i^3 are negligible. The equation of motion reduces to:

$$\ddot{u}_i + (\Gamma_i + \gamma_{ji}^{\mathrm{xnl}} u_j^2)\dot{u}_i + (\Omega_i^2 + \beta_{ji}^{\mathrm{x}} u_j^2) u_i = 0. \tag{5.20}$$

The term $\gamma_{\mathrm{ji}}^{\mathrm{xnl}} u_i u_j \dot{u}_i$ is negligible in both the regimes. It starts to be relevant when both the modes are strongly driven. Given the complexity of distinguishing between the various nonlinear terms in that case, we do not consider it.

As in the self-nonlinear case, we want to solve the equation of motion for the free evolving oscillator to understand how the cross-nonlinear terms affect the displacement amplitude and the mechanical frequency during the ringdown. First, we impose that the mode of interest (u_i) is initially displaced from its rest position, Eq. (4.16). Moreover we assume that the displacement of the strongly driven mode (u_j) is oscillating with fix amplitude A_j

$$u_j = A_j \cos(\Omega_j' t), \tag{5.21}$$

where Ω_j' is the resonance frequency shifted according to Eq. (4.33). Since the displacement amplitude is fixed, we assume that Ω_j' is constant. Following the procedure implemented in Sec. 4.3, we solve the equation through the multiple-scales method. At first, we highlight the small terms with an epsilon

$$\ddot{u}_i + (\epsilon\tilde{\Gamma}_i + \epsilon\tilde{\gamma}_{ji}^{\mathrm{xnl}} u_j^2)\dot{u}_i + (\Omega_i^2 + \epsilon\tilde{\beta}_{ji}^{\mathrm{x}} u_j^2) u_i = 0, \tag{5.22}$$

where $\Gamma_i = \epsilon\tilde{\Gamma}_i$, $\gamma_{ji}^{\mathrm{xnl}} = \epsilon\tilde{\gamma}_{ji}^{\mathrm{xnl}}$ and $\beta_{ji}^{\mathrm{x}} = \epsilon\tilde{\beta}_{ji}^{\mathrm{x}}$. Then, we assume that the solution can be expressed in terms of a fast (t_0) and a slow ($t_1 = \epsilon t$) time scale. First we write the displacement as a function of the two new time-scales, $u_i(t_0, \epsilon t_1)$ and we write the equation of motion writing the time derivatives using the transformations in Eqs. (4.19). The resulting equation of motion is

$$\begin{aligned} &(\partial_{t_0 t_0} + \epsilon\partial_{t_0 t_1})\, u_i + \epsilon\left(\tilde{\Gamma}_i + \tilde{\gamma}_{ji}^{\mathrm{xnl}} A_j^2 \cos^2(\Omega_i' t_0)\right)\partial_{t_0} u_i + \\ &+ \left(\Omega_i^2 + \tilde{\beta}_{ji}^{\mathrm{x}} A_j^2 \cos^2(\Omega_i' t_0)\right) u_i = 0, \end{aligned} \tag{5.23}$$

where we neglected all the higher order terms in ϵ. Then we substitute $u_i(t, \epsilon t)$ with an uniform approximate solution defined in Eq. (4.21). The equation of motion becomes

$$\partial_{t_0 t_0} u_{i,0} + \Omega_i^2 u_{i,0} + \epsilon \Big[\partial_{t_0 t_0} u_{i,1} + 2\partial_{t_0 t_1} u_{i,0} + \tilde{\Gamma}_i \partial_{t_0} u_{i,0} + \\ + \tilde{\gamma}_{ji}^{\mathrm{xnl}} A_j^2 \cos^2(\Omega_j' t_0) \partial_{t_0} u_{i,0} + \tilde{\beta}_{ji}^{\mathrm{x}} A_j^2 \cos^2(\Omega_j' t_0) u_{i,0} + \Omega_i^2 u_{i,1} \Big] = 0, \tag{5.24}$$

where we explicitly wrote u_j using Eq. (5.21). Finding a solution for this equation corresponds to solving the following system

$$\partial_{t_0 t_0} u_{i,0} + \Omega_i^2 u_{i,0} = 0 \tag{5.25a}$$

$$\begin{aligned} \partial_{t_0 t_0} u_{i,1} + \Omega_i^2 u_{i,1} = &- 2\partial_{t_0 t_1} u_{i,0} - \tilde{\Gamma}_i \partial_{t_0} u_{i,0} + \\ &- \tilde{\gamma}_{ji}^{\mathrm{xnl}} A j^2 \cos^2(\Omega_j' t_0) \partial_{t_0} u_{i,0} + \\ &- \tilde{\beta}_{ji}^{\mathrm{x}} A j^2 \cos^2(\Omega_j' t_0) u_{i,0}. \end{aligned} \tag{5.25b}$$

The solution of Eq. (5.25a) coincides with the solution of Eq. (4.23a). Therefore we substitute Eq. (4.24) in Eq. (5.25b) which becomes

$$\partial_{t_0 t_0} u_{i,1} + \Omega_i^2 u_{i,1} = F_1 \sin(\Omega_i t_0 + \varphi_i(t_1)) + F_2 \cos(\Omega_i t_0 + \varphi_i(t_1)), \tag{5.26}$$

where we performed the following substitutions:

$$\begin{aligned} F_1 =& 2\Omega_i \partial_{t_1} A_i(t_1) + \Omega_i \tilde{\Gamma}_i A_i(t_1) + \frac{\tilde{\gamma}_{ji}^{\mathrm{xnl}}}{2} A j^2 A_i(t_1) \Big[1 + \cos(2\Omega_j' t_0) \Big], \\ F_2 =& 2\Omega_i A_i(t_1) \partial_{t_1} \varphi_i(t_1) + \frac{\tilde{\beta}_{ji}^{\mathrm{x}}}{2} A_j^2 A_i(t_1) \Big[1 + \cos(2\Omega_j' t_0) \Big]. \end{aligned}$$

Importantly, all the coefficients in Eqs. (5.27) are functions of the slow time scale t_1. The only two terms showing a dependence on the fast scale are the oscillating terms. We notice that those terms are oscillating faster than all the other terms in the system. Therefore we can assume that they average to zero and the above equations reduce to

$$F_1 = 2\Omega_i \partial_{t_1} A_i(t_1) + \tilde{\Gamma}_i A(t_1) \Omega_i + \frac{\tilde{\gamma}_{ji}^{\mathrm{xnl}}}{2} A_j^2 A_i(t_1) \tag{5.28a}$$

$$F_2 = 2\Omega_i A_i(t_1) \partial_{t_1} \varphi_i(t_1) + \frac{\tilde{\beta}_{ji}^{\mathrm{x}}}{2} A_j^2 A_i(t_1). \tag{5.28b}$$

Next, we impose $F_1 = 0$ and $F_2 = 0$ to avoid secular terms. Solving Eq. (5.28a) imposing the former condition allows us to find the time evolution of the displacement amplitude which is described by the following expression:

$$A_i(t_1) = c e^{-\left(\frac{\tilde{\Gamma}_i}{2} + \frac{\tilde{\gamma}_{ji}^{\mathrm{xnl}}}{4} A_j^2 \right) t_1}. \tag{5.29}$$

We determine the constant c from the initial condition. Substituting Eq. (5.29) in Eq. (5.28b) with the above condition for F_2, we find the time evolution of the phae ϕ_i to be

$$\varphi_i(t_1) = \frac{1}{4}\tilde{\beta}^{\mathrm{x}}_{ji} A_j^2 t_1 + \Phi, \tag{5.30}$$

with Φ being a constant determined by the initial condition. We substitute Eq. (5.29) and Eq. (5.30) in the zeroth order solution $u_0(t_0, t_1)$. Similarly to the self-geometric nonlinearities case, Sec. 4.3, we only keep the zeroth order term in ϵ, therefore the solution $u_i(t_0, t_1)$ coincides with $u_0(t_0, t_1)$. Finally we apply the inverse transformation to write the solution as a function of the natural time scale t. The solution of the equation of motion after applying the initial condition reads

$$u_i(t) = A_i(t)\cos(\Omega_i t + \varphi_i(t)), \tag{5.31}$$

where the displacement amplitude and the phase take the following forms

$$A_i(t) = A_{i,0} e^{-\left(\frac{\Gamma_i}{2} + \frac{\gamma^{\mathrm{xnl}}_{ji}}{4} A_j^2\right) t}, \tag{5.32a}$$

$$\varphi_i(t) = \frac{\beta^{\mathrm{x}}_{ji}}{4} A_j^2 t + \Phi. \tag{5.32b}$$

Notice that $A_{i,0}$ is the initial displacement. The constant Φ is still unknown, but it is not relevant for our analysis.

Let us discuss the solution we obtain for the cross-nonlinearities case. Both the amplitude and the phase show a dependence which is quadratic with the displacement amplitude of the strongly driven mode. In particular, from Eq. (5.32a) we observe that for a constant oscillation of the mode j, the mode i decays linearly with an increased decay rate which depends on the amplitude A_j

$$\Gamma_i' = \Gamma_i + \frac{\gamma^{\mathrm{xnl}}_{ji}}{2} A_j^2. \tag{5.33}$$

On the other hand, from the time derivative of Eq. (5.32b) we can derive the instantaneous resonance frequency shift. As expected, the cross-duffing term introduces a shift of the resonance frequency which depends quadratically on A_j with the following expression:

$$\Omega_i' = \Omega_i \left(1 + \frac{\beta^{\mathrm{x}}_{ji}}{4} A_j^2\right). \tag{5.34}$$

5.4 SOFT-CLAMED PHONONIC DIMERS - NONLINEAR CASE

We now discuss how we experimentally measure both the self- and the cross-nonlinear parameters in the phononic dimer geometries, already linearly characterized in Sec. 5.2.2. In Sec. 5.3 we identified two regimes where we can measure the two nonlinear contributions separately and we derived the laws we can use to extract the relevant information through a ringdown measurement. Similarly, we proceed with an experimental characterization in two steps, where we measure the two types of nonlinearities independently.

5.4.1 *Measuring self-nonlinearities*

We start by characterizing the self-nonlinearities, i. e. the geometrical nonlinearities entering in the dynamics of the mode of interest when its displacement amplitude is comparable with the membrane thickness. To perform this measurement, we monitor the displacement amplitude and the frequency shift of the mode of interest while we are leaving the other mode in its thermal state. In this way we can neglect the cross-nonlinearities. The measurement procedure coincides with the one described in Sec. 4.4.

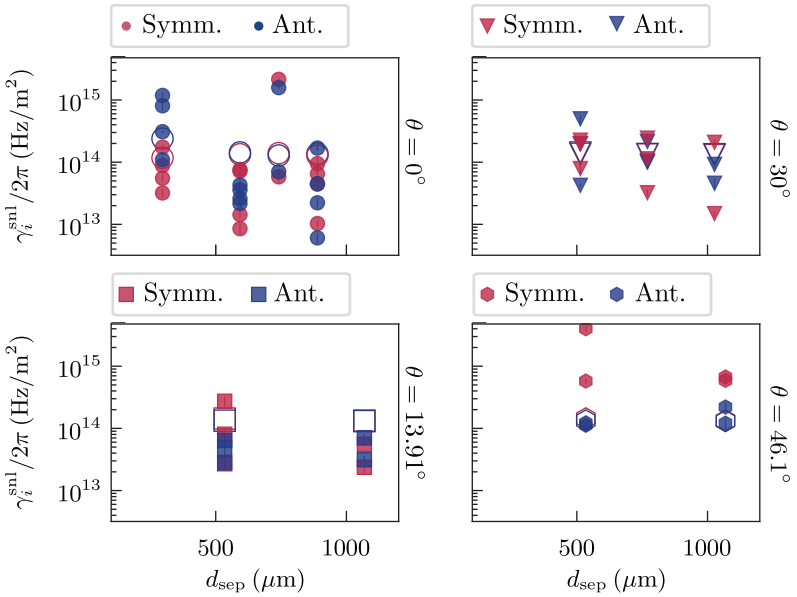

Figure 5.6: Self-nonlinear damping in phononic dimers. In each panel we plot the self-nonlinear damping against the dimer separation for a given orientation, represented by a different symbol. Each filled symbol represents the measured self-nonlinear damping of a single membrane. We extract the self-nonlinear damping averaging the fit result from 5 ringdowns. The error bar is one standard deviation. The empty symbols are the simulated values. Red (blue) symbols are associated with the symmetric (antisymmetric) mode. The orientations are listed at the right of each panel.

Let us first consider the self-nonlinear damping terms. The measured parameters for both the symmetric and antisymmetric modes of all the samples are reported in Fig. 5.6 (red and blue filled points). We simulate the nonlinear damping by substituting the eigenfunctions estimated through FEM simulations in Eq. (4.14e). The simulation outcomes coincide with the measurement results within the experimental scattering.

Then we move to discuss the self-Duffing terms. To express the measurement results in the same unit used in Chapter 4, we consider the self-Duffing shift per displacement $\omega_i^{\mathrm{sD}} = \beta_i^{\mathrm{s}}/2\Omega_i$. In Fig. 5.7 we report all the measured self-Duffing parameters for the symmetric (blue filled points) and the antisymmetric (red filled points) for all the samples. We compare the measured self-Duffing terms with the simulated values obtained from Eq. (4.14d) normalized to twice the resonance frequency. The experimental and simulated results agree within the experimental scatter.

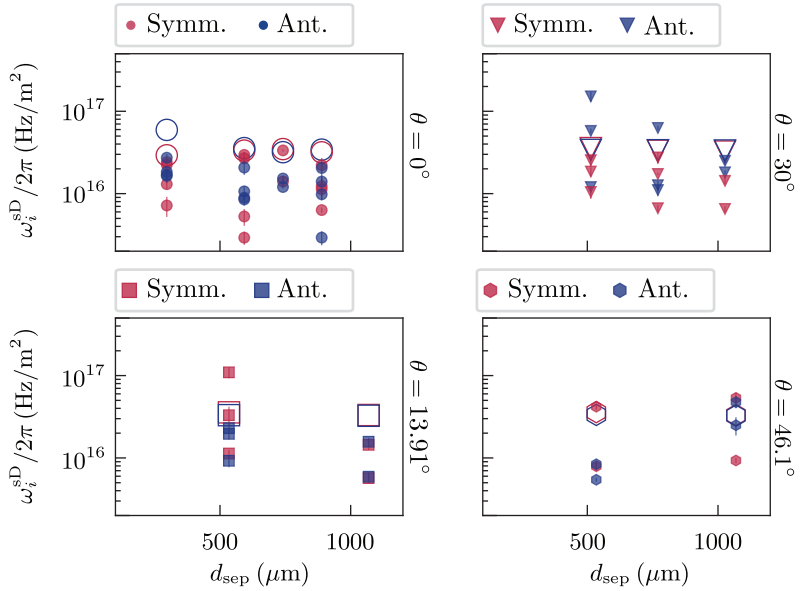

Figure 5.7: Self-Duffing in phononic dimers. In each panel we plot the self-Duffing shift per displacement as a function of dimer separation for a given orientation. Each symbol is associated with a different dimer separation. The filled red (blue) points are the measured values for the symmetric (antisymmetric) mode. Each point is the self-Duffing shift per displacement measured on a single membrane. We extract it by performing 5 ringdown repetitions, then we average the fit results. The error bars correspond to one standard deviation. The empty red (blue) points correspond to the simulated value for the symmetric (antisymmetric) mode. The orientations are listed on the right of each panel.

5.4.2 *Measuring cross-nonlinearities*

We now characterize the cross-nonlinear terms in the fabricated devices. In contrast to the self-nonlinear case, we cannot measure the cross-Duffing and the self-nonlinear damping simultaneously. We need to implement two separate measurement procedures where we need to monitor the vibration of both the symmetric and the antisymmetric mode.

We start with the estimation of the cross-Duffing parameters. For this measurement procedure we leave the mode of interest (u_i) in its thermal state. Simultaneously we drive the second mode (u_j) to an amplitude where we expect to observe nonlinear phenomena. Then, we turn off the drive and we monitor both the modes u_i and u_j using two separate demodulators in the lock-in amplifier. To extract the

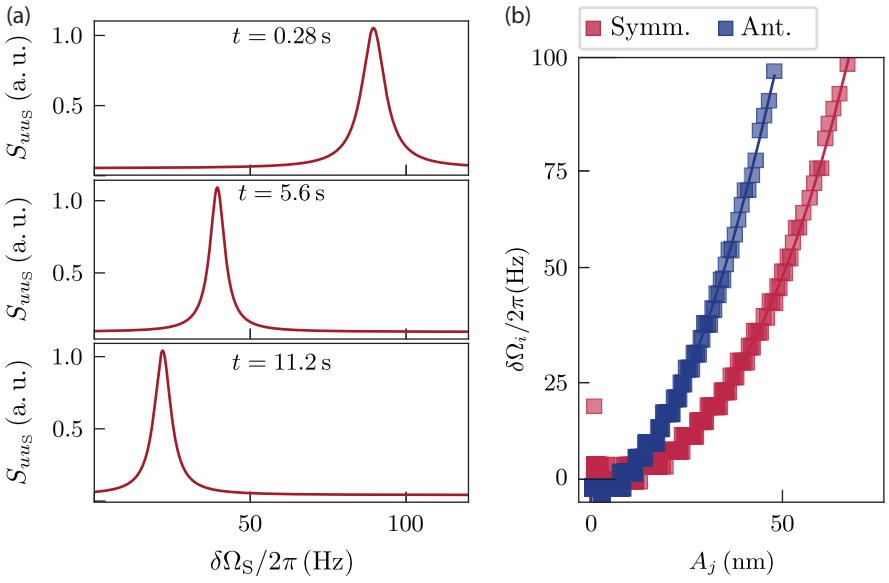

Figure 5.8: Example of a cross-Duffing measurement. (a) Lorentzian fit performed at different times on the FFT of the thermally-driven mode. We only show the fit of the symmetric mode. Each panel shows a Lorentzian fit extracted from a different time interval. (b) Example of a frequency shift of the thermally-driven mode as a function of the amplitude of the strongly driven mode. The frequency shift is extracted from the fit shown in (a). The red (blue) points corresponds to the case where the antisymmetric (symmetric) mode is strongly driven. The solid lines are the quadratic fit. The data are extracted from a membrane with $\theta = 13.91°$ and $d_{\text{sep}} = 1$ unit cell.

instantaneous frequency shift $\Omega_i'(t)/2\pi$ of the mode left in the thermal state, we perform an FFT every 0.28 s of acquired data. We fit the obtained spectrum with a Lorentzian peak. Then, we assume that the peak center frequency corresponds to the instantaneous resonance

frequency $\Omega_i'(t)/2\pi$. During the ringdown we observe the peak shifting towards lower frequencies. An example of a Lorentzian peak position at different times is shown in Fig. 5.8 (a). Simultaneously, in each time interval we measure the calibrated amplitude A_j and we take its mean value for the 0.28 s period. We apply the absolute calibration method described in Sec. 3.3.1. To extract the cross-Duffing term we plot the instantaneous resonance frequency $\Omega_i'/2\pi$ against the calibrated amplitude A_j measured in the same time interval. We plot an example of the frequency shift of the mode u_i against the amplitude of the mode u_j in Fig. 5.8 (b). We use Eq. (5.34) as the fitting function. We repeat the measurement for all dimer separations and orientations. The fit results are reported in Fig. 5.9.

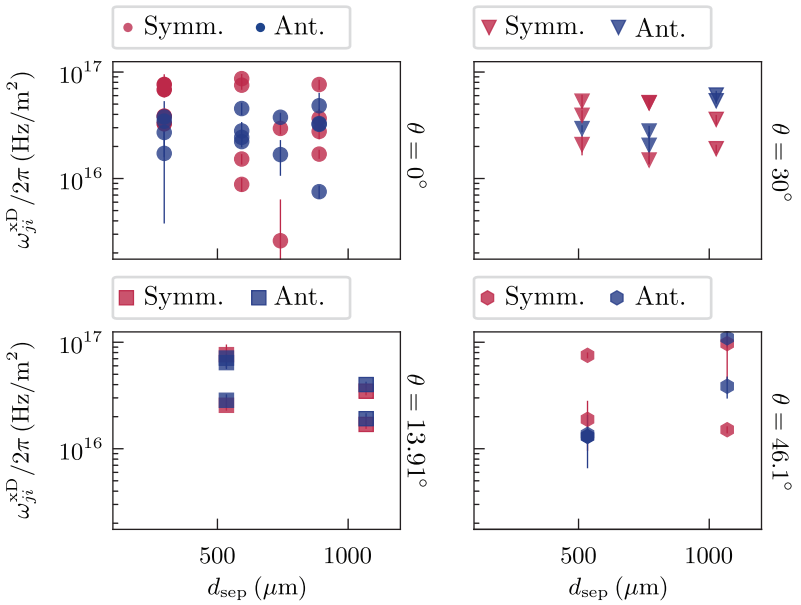

Figure 5.9: Cross-Duffing nonlinearity in phononic dimers. In each panel we plot the measured cross-Duffing nonlinearity against the dimer separation for all the samples of a given orientation. Each orientation is associated with a different symbol. The orientation is listed at the right of each panel. The filled red (blue) points are the measured values for the symmetric (antisymmetric) mode estimated from an average over 5 ringdown repetitions performed on the same membrane. The error bars correspond to one standard deviation.

We use a phenomenological model to introduce the cross-nonlinear terms, therefore we do not have a rigorous derivation that we can use to simulate the cross-nonlinear terms from the modeshapes, yet. However, it is interesting to compare the measured self-Duffing and the cross-Duffing parameters to have an idea of the relation between the two. In Fig. 5.10 we plot the cross-Duffing against the self-Duffing measured on the same sample for all the geometries. We extract the ratio between the two values using a linear fit (black dashed line in Fig. 5.10). From the linear fit we obtain a ratio between the nonlinear terms given by

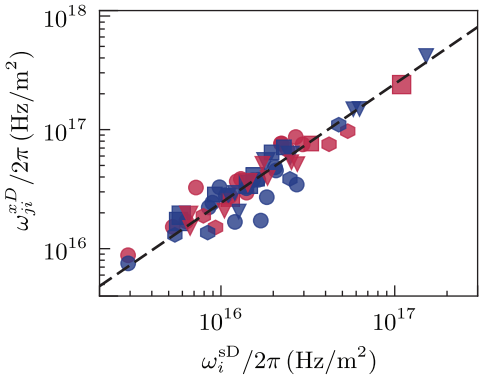

Figure 5.10: Self-Duffing against cross-Duffing. Each symbol represents a different angle. The red (blue) points are the data relative to the symmetric (antisymmetric) mode. Each point represents the parameters associated with a single membrane. The black dashed line is a linear fit.

$\omega_{ji}^{\mathrm{xD}}/\omega_i^{\mathrm{sD}} = 2.6 \pm 0.5$. The error on the linear fit corresponds to a 95% confidence interval. Interestingly, the factor we get is compatible with the factor of 3 predicted by the phenomenological model, see Eq. (5.18).

Finally, we measure the cross-nonlinear damping in our structure. For this particular type of measurement we need to drive both modes simultaneously. First we choose a driving voltage for the mode of interest (u_i) small enough to avoid any type of self-nonlinear effects. Then, we apply a second driving tone at the frequency $\Omega_j/2\pi$ with a strength large enough to drive second mode (u_j) in the nonlinear regime. We turn off the drive of the weakly driven mode (u_i) and we monitor simultaneously the amplitudes $A_i(t)$ and A_j. Notice that the drive on the mode u_j is on and constant during the whole measurement. From the exponential decay of the weakly driven mode we extract the effective linear damping Γ_i' which is related to the amplitude A_j through Eq. (5.33).

We repeat the measurement varying the driving strength on the mode j, i. e the amplitude A_j. The larger the amplitude of the nonlinear mode, the faster the decay. An example of a set of amplitude decays of the linear symmetric mode i measured for different driving strengths applied on the antisymmetric mode is reported in Fig. 5.11 (a). If we plot the measured effective decay rate Γ_i' against the calibrated displacement amplitude A_j, we can extract the cross-nonlinear damping term using Eq. (5.33) (see Fig. 5.11 (b)). We calibrate the amplitudes A_j in unit of meters applying by applying an absolute calibration method (see Sec. 3.3.1).

We characterized the cross-nonlinear damping term for the geometry $\theta = 13.91°$ and $d_{\mathrm{sep}} = 1$ unit cell because this parameters is particularly interesting for force sensing applications. As a matter of fact, the cross-nonlinear damping has been identified as a limiting factor for the force sensitivity of phononic dimers in the MRFM protocol proposed in

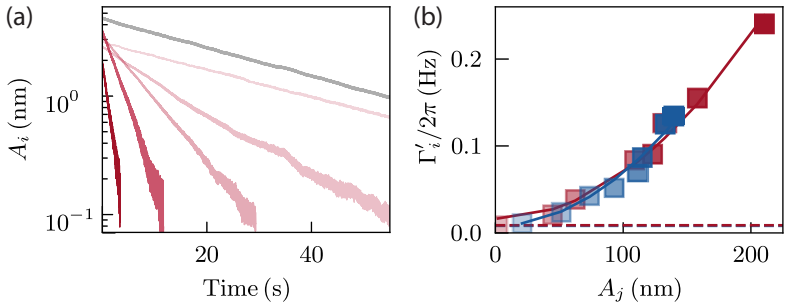

Figure 5.11: Measured cross-nonlinear damping in phononic dimers. (a) Ringdown of the weakly driven mode $A_{\mathrm{S}}(t)$ for growing amplitude of the strongly driven mode A_{A} (from light to dark red). A_{A} is constant during the ringdown time. The grey line is the ringdown in absence of the strong drive in the antisymmetric mode for comparison. (b) Effective linear damping measured from the exponential decay of the weakly driven mode against the amplitude of the strongly driven one. Red (blue) points coincide with the case where the antisymmetric (symmetric) mode is strongly driven. The solid lines are the quadratic fits from which we extract the cross-nonlinear damping parameter. The red (blue) dashed line represents the damping rate in absence of any cross-nonlinear effect for the symmetric (antisymmetric) mode.

[Koš+20]. The cross-nonlinear damping values extracted for the symmetric and antisymmetric modes are $\gamma_{\mathrm{AS}}^{\mathrm{xnl}}/2\pi = 1 \times 10^{13}\mathrm{Hz/m^2}$ and $\gamma_{SA}^{\mathrm{xnl}}/2\pi = 1 \times 10^{13}\mathrm{Hz/m^2}$, respectively. Notably, the cross-nonlinear terms coincide, as suggested from the phenomenological model. However, if we compare the cross-nonlinear damping with the self-nonlinear damping term we observe a big discrepancy between the two, suggesting a more complicated mechanism behind the presence of the cross-nonlinear damping term.

6

PARAMETRICALLY-DRIVEN HARMONIC OSCILLATOR

In this chapter we show some preliminary results of our research work on parametric effects in dissipation-diluted nanomechanical resonators. By modulating the in-plane stress we can model our membrane resonator as parametric oscillator, i. e. a harmonic oscillator with one of the system parameter modulated in time. We start with a general description of a parametric harmonic oscillator where the modulated parameter is the resonance frequency, then we show that in this situation the harmonic oscillator turns into a mechanical amplifier. We describe how we can modulate the elastic constant of a soft-clamped membrane resonator and we compare the parametric gains obtained on different bandgap modes. From the parametric characterization we deduce that the parametric driving strength has a non-trivial geometric dependence. We extend the linear continuum elastic model presented in Sec. 1.2 to explain the observed geometric dependence of the parametric driving strength. At the end of the chapter we describe how we can interpret and verify the model, and we show the preliminary results.

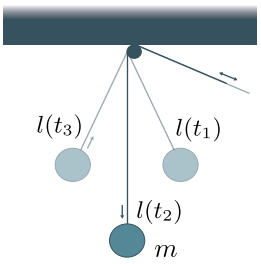

Parametrically excited simple pendulum.

6.1 DEGENERATE PARAMETRIC OSCILLATION

We define a parametric oscillator as a harmonic oscillator where the motion is driven by the time modulation of a system parameter. Here we focus on the case of a parametric oscillator where the modulated parameter is the elastic constant. In particular, we are interested in the *degenerate* parametric oscillator, i. e. a parametrically-driven harmonic oscillator where the modulation happens at twice the resonance frequency. Examples of parametric oscillators are a simple pendulum with a length varying during the oscillation or with a support moving harmonically along the vertical direction or beam subjected to a periodic modulation of its elastic constant. [RG91].

We start the discussion already writing the equation of motion of a single vibrational mode associated with an out-of-plane displacement u_i. In the presence of a modulation of the elastic constant, this equation

takes the form of a parametrically-driven harmonic oscillator which is usually written as follow

$$\ddot{u}_i + \Gamma_i \dot{u}_i + \Omega_i^2 u_i + \frac{k_{\mathrm{p}_i}(t)}{m_i} u_i = \frac{f_i^{\mathrm{ext}}}{m_i} \cos(\Omega_i t + \varphi_{\mathrm{r}}) \tag{6.1}$$

where $k_{\mathrm{p}_i}(t)$ represents the modulation of the elastic constant and we include the presence of an external resonant force characterized by a phase φ_{r}. We are interested in a degenerate parametric modulation. Hence we can write the modulated component of the elastic constant as

$$k_{\mathrm{p}_i}(t) = k_{\mathrm{p}_i} \sin(2\Omega_i t) \tag{6.2}$$

where k_{p_i} is the strength of the modulation.

Eq. (6.1) is also known as damped Mathieu equation [Cle03]. To solve it, we need to use a different approach with respect to the one in Sec. 4.3 and Sec. 5.3. Following the mathematical derivation in [RG91; Cle03], we introduce the complex variables

$$a_i = \dot{u}_i + i\omega_i^* u_i, \tag{6.3a}$$
$$a_i^* = \dot{u}_i^* - i\omega_i u_i^*, \tag{6.3b}$$

where * represents the complex conjugate, i is the imaginary unit and the complex frequency ω_i is defined as

$$\omega_i = \Omega_i \left[\sqrt{1 - \frac{1}{4Q^2}} + \frac{i}{2Q} \right], \tag{6.4}$$

with Q the quality factor of the linear harmonic oscillator. We can invert Eqs. (6.3) to get an expression for u_i and $\dot{u}_i$ as a function of the new variables

$$u_i = \frac{a_i - a_i^*}{i(\omega_i^* + \omega_i)}, \tag{6.5a}$$
$$\dot{u}_i = \frac{\omega_i a_i + \omega_i^* a_i^*}{\omega_i^* + \omega_i}. \tag{6.5b}$$

We want to express the equation of motion in terms of the new variables. To perform the transformation we still need to find an expression for $\ddot{u}_i$. Writing $\dot{u}_i$ from Eq. (6.3a) and performing the time derivative we get

$$\ddot{u}_i = \dot{a}_i - i\omega_i^* \dot{u}_i = \dot{a}_i - i\omega_i^* \left(\frac{\omega_i a_i + \omega_i^* a_i^*}{\omega_i^* + \omega_i} \right), \tag{6.6}$$

where we use Eq. (6.5b) in the last step. Substituting Eqs. (6.5) and Eq. (6.6) in Eq. (6.1) and after some algebraic manipulations we obtain the following equation of motion in the new variables

$$\dot{a}_i = i\omega_i a_i + i \frac{k_{\mathrm{p}_i}(t)}{m_i} \frac{a_i - a_i^*}{\omega_i + \omega_i^*} + \frac{f_i^{\mathrm{ext}}}{m_i} \cos(\Omega_i t + \varphi_{\mathrm{r}}). \tag{6.7}$$

We assume now that the equation above has a solution with the general form $a_i = A_i e^{\mathrm{i}\Omega_i t}$, where A_i is a complex number. Inserting the general solution and factoring out the terms proportional to $e^{i\Omega_i t}$, the problem of finding the solution for Eq. (6.7) reduces to solving the following equation

$$i\frac{\Omega_i}{2Q}A_i + \frac{k_{\mathrm{p}_i}}{4m_i\Omega_i}A_i^* - \frac{f_i^{\mathrm{ext}}}{2m_i}e^{i\varphi_{\mathrm{r}}} = 0, \tag{6.8}$$

where we dropped out all the fast oscillating terms and we canceled the time dependent term $e^{i\Omega_i t}$. Moreover, we made the approximations $\omega_i^* + \omega_i \approx 2\Omega_i$ and $\omega_i - \Omega_i = \mathrm{i}\frac{\Omega_i}{2Q}$, which are valid when we are in the low dissipation regime ($Q \gg 1$). This condition is always satisfied in our system. We can solve Eq. (6.8) writing the complex variable A_i as $\Re(A_i) + i\Im(A_i)$. After some algebra we find the solution

$$A_i = \frac{f_i^{\mathrm{ext}} Q m_i}{\Omega_i}\left[\frac{\cos(\varphi_{\mathrm{r}})}{1+\frac{Qk_{\mathrm{p}_i}}{2k_i}} + i\frac{\sin(\varphi_{\mathrm{r}})}{1-\frac{Qk_{\mathrm{p}_i}}{2k_i}}\right]. \tag{6.9}$$

The above equation represents the amplitude of the general solution in the complex variable A_i. To derive the solution in the initial variable u_i we need to substitute the general solution $A_i e^{i\Omega_i t}$ in Eq. (6.5a), where we use Eq. (6.9) to express the amplitude:

$$u_i = \Im(A_i)\cos(\Omega_i t) + \Re(A_i)\sin(\Omega_i t), \tag{6.10}$$

with $\Re(A_i)$ and $\Im(A_i)$ the real and imaginary part of A_i respectively. To understand the effect of the parametric drive it is convenient to look at the displacement amplitude ($|u_i|$). From Eq. (6.10) it coincides with $|u_i| = \sqrt{\Im(A_i)^2 + \Re(A_i)^2}$. We notice that with $k_{\mathrm{p}_i} = 0$, i. e. no parametric force applied, we recover the displacement amplitude for a simple harmonic oscillator driven at resonance.

When the parametric force is applied, the displacement amplitude increases or decreases accordingly with the phase of the resonant drive. Therefore, the parametric drive acts on the displacement amplitude of a driven harmonic oscillator as a mechanical amplifier. The gain G of the amplification is defined as the ratio between the displacement amplitude when a parametric modulation is applied and the amplitude when only the resonant force is applied. From Eq. (6.10) and Eq. (6.9) we find the following expression for the gain

$$G = \frac{|u_i|}{|u_i|_{k_{\mathrm{p}_i}=0}} = \left[\frac{\cos^2(\varphi_{\mathrm{r}})}{\left(1+\frac{Qk_{\mathrm{p}_i}}{2k_i}\right)^2} + \frac{\sin^2(\varphi_{\mathrm{r}})}{\left(1-\frac{Qk_{\mathrm{p}_i}}{2k_i}\right)^2}\right]^{1/2}. \tag{6.11}$$

Here we highlight that the gain is a periodic function of the phase and we can move from amplification to deamplification by varying the resonant phase. The phase dependence of the gain is shown in Fig. 6.1 (a). Moreover, by choosing a well defined phase, the parametric gain increases

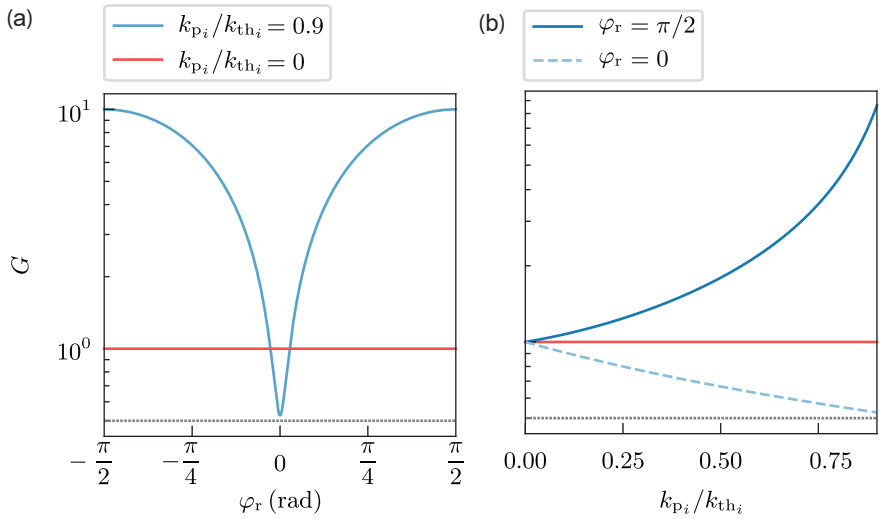

Figure 6.1: Theoretical amplitude gain. (a) Amplitude gain against the resonant drive phase (blue line), the gain in absence of any parametric drive is shown for comparison (red line). The dotted line represents the minimum gain $G \to 0.5$ corresponding to $k_{p_i}/k_{th_i} \to 1$. (b) Amplitude gain against the k_{p_i}/k_{th_i} in the two limiting cases of maximum (solid blue) and minimum (dashed light blue) amplification. The grey dotted line represents the minimum gain corresponding to $k_{p_i}/k_{th_i} \to 1$. The solid red line is the gain without any parametric drive.

as the ratio $Qk_{p_i}/2k_i$ approaches 1. In Fig. 6.1 (b) we show the amplitude gain as a function of the $Qk_{p_i}/2k_i$ ratio in the two limiting case of $\varphi_r = 0$ (maximum deamplification) and $\varphi_r = \pi/2$ (maximum amplification). We introduce the parametric threshold $k_{th_i} = 2k_i/Q$ representing the maximum modulation we can apply. When the parametric modulation approaches the threshold the gain approaches infinity and we enter in the instability regime. We highlight that while the amplification goes to infinity for $k_{p_i}/k_{th_i} \to 1$, the maximum deamplification is limited to $G \to 0.5$. In this thesis we are only interested in the stable regime.

The amplitude gain can be generalized to include a varying phase φ_p of the parametric drive

$$G = \left[\frac{\cos^2(\phi_r - \frac{\phi_p}{2})}{(1 + \frac{k_p}{k_{th}})^2} + \frac{\sin^2(\phi_r - \frac{\phi_p}{2})}{(1 - \frac{k_p}{k_{th}})^2} \right]^{1/2} . \tag{6.12}$$

We show how the gain varies as a function of both the phases in the contour plot in Fig. 6.2.

In our system we decide to vary the parametric phase φ_p so we move on horizontal lines in Fig. 6.2. The resonant phase can vary due to phase delays introduced by instruments and cables. Therefore our horizontal line is characterized by an offset determined by the effective resonant

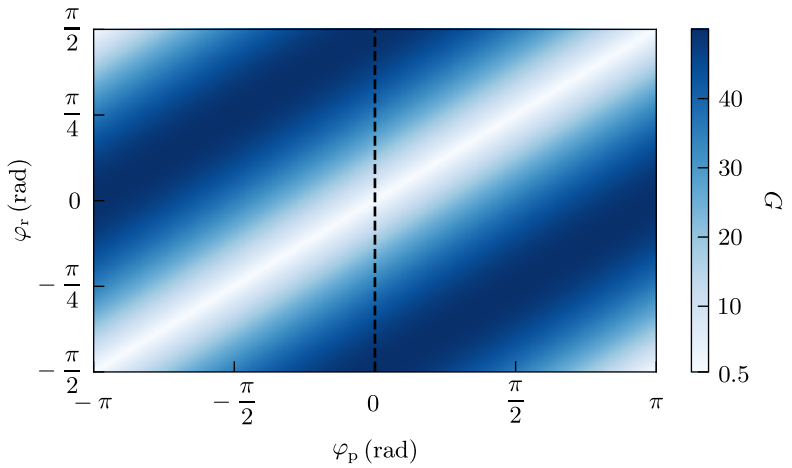

Figure 6.2: Phase dependence of the amplitude gain. The two axes represent the two phases while the colors represent the gain. We choose a parametric strength $k_{\mathrm{p}_i}/k_{\mathrm{th}_i} = 0.98$, close to threshold. The black dashed line coincides with the case reported in Fig. 6.1 (a).

phase. The experimental maximum amplification and deamplification phase are defined by this offset.

We now discuss the effect of a parametric drive applied to a harmonic oscillator driven by the stochastic thermal force. Intuitively we expect the fluctuating phase of the thermal force to span all the possible relative phases between resonant and parametric drive, producing both amplification and deamplification. However, to understand the effect of the parametric drive on a thermal state, it is convenient to look at the mechanical quadratures X_1 and X_2, already introduced in Sec. 1.2.5, substituting the out-of-plane displacement u_i with the ansatz $u_i(t) = X_1 \cos(\Omega_i t) + X_2 \sin(\Omega_i t)$. Following the same approach used in the linear oscillator, we substitute Eq. (1.39) in Eq. (6.1) writing the external force as the sum between a sine ($f^{\mathrm{ext}}_{i,\mathrm{s}}$) and a cosine ($f^{\mathrm{ext}}_{i,\mathrm{c}}$) component. After this transformation, we can divide the equation of motion in two equations, one for X_1 and one for X_2

$$\dot{X}_1 + X_1 \left(\frac{\Gamma_i}{2} - \frac{k_{\mathrm{p}_i}}{2 m_i \Omega_i} \right) = -\frac{f^{\mathrm{ext}}_{i,\mathrm{s}}}{2\Omega_i}, \tag{6.13a}$$

$$\dot{X}_2 + X_2 \left(\frac{\Gamma_i}{2} + \frac{k_{\mathrm{p}_i}}{2 m_i \Omega_i} \right) = \frac{f^{\mathrm{ext}}_{i,\mathrm{c}}}{2\Omega_i}, \tag{6.13b}$$

where we neglected all the terms proportional to $\Omega_i X_i$ (except for the one containing the elastic constant modulation) and the fast terms oscillating terms at $\pm 3\Omega_i t$ and $\pm 2\Omega_i t$. From Eq. (1.45) we know that the two quadratures of a linear oscillator subjected to a random stochastic force are fluctuating with a variance defined by the thermal energy. We are interested in deriving how the parametric drive affects the stochastic

thermal fluctuations. We first solve Eqs. (6.13) in the frequency domain

$$X_1(\Omega) = -\frac{\mathcal{F}^{\mathrm{ext}}_{i,\mathrm{s}}(\Omega)}{2\Omega_i}\frac{1}{\left(\frac{\Gamma_i}{2} - \frac{k_{\mathrm{p}_i}}{2m_i\Omega_i} - i\Omega\right)}, \tag{6.14a}$$

$$X_2(\Omega) = \frac{\mathcal{F}^{\mathrm{ext}}_{i,\mathrm{c}}(\Omega)}{2\Omega_i}\frac{1}{\frac{\Gamma_i}{2} + \frac{k_{\mathrm{p}_i}}{2m_i\Omega_i} - i\Omega}. \tag{6.14b}$$

The solution for the two quadratures has the same form as the one for a linear oscillator except for a term proportional to the elastic constant modulation. This term acts with opposite sign on the two quadratures, meaning that the response to a sinusoidal resonance force ($\varphi_{\mathrm{r}} = \pi/2$) is amplified while the response to a cosine force ($\varphi_{\mathrm{r}} = 0$) is deamplified. Knowing the solution in the frequency domain we can evaluate the two following PSDs using Eq. (1.36)

$$S_{X_1X_1} = \frac{m_i k_{\mathrm{B}} T}{2\Omega_i Q}\frac{1}{\left(\frac{\Gamma_i}{2} - \frac{k_{\mathrm{p}_i}}{2m_i\Omega_i}\right)^2 + \Omega^2}, \tag{6.15a}$$

$$S_{X_2X_2} = \frac{m_i k_{\mathrm{B}} T}{2\Omega_i Q}\frac{1}{\left(\frac{\Gamma_i}{2} + \frac{k_{\mathrm{p}_i}}{2m_i\Omega_i}\right)^2 + \Omega^2}, \tag{6.15b}$$

where we use Eq. (1.37) to express the PSD of the thermal force. Finally, applying Eq. (1.38) we can estimate the variances using the PSD in Eq. (6.15), which have the following expressions

$$\langle X_1^2\rangle = \frac{k_{\mathrm{B}}T}{2m_i\Omega_i^2}\frac{1}{1 - \frac{k_{\mathrm{p}_i}}{k_{\mathrm{th}_i}}}, \tag{6.16a}$$

$$\langle X_2^2\rangle = \frac{k_{\mathrm{B}}T}{2m_i\Omega_i^2}\frac{1}{1 + \frac{k_{\mathrm{p}_i}}{k_{\mathrm{th}_i}}}. \tag{6.16b}$$

$$\tag{6.16c}$$

From the equations above we see that the presence of the parametric drive does not affect the two quadratures symmetrically. One of the two variances is amplified while the other is deamplified below the thermomechanical noise. Thus a parametric modulation applied on a thermally-driven harmonic oscillator generates a thermomechanical squeezed state [RG91], that is a thermal state with a quadrature fluctuations below the thermomechanical noise. In particular, the maximum amount of squeezing we can get with the parametric modulation before reaching the instability regime coincides with a variance of $\langle X_2^2\rangle = \frac{k_{\mathrm{B}}T}{2m_i\Omega_i^2}\frac{1}{2}$.

6.2 MEASURING PARAMETRIC STRENGTH

We are interested in generating and quantifying the parametric effects in our soft-clamped SiN membrane. From an independent work conducted

by D. Halg et al. [H+21a] on dimer membranes constituted by two Lotus defects, we already have an indication of the parametric driving strength we can reach for our soft-clamped devices. In particular they quantified the non-degenerate parametric coupling between the symmetric and antisymmetric mode in a parametric upconversion scheme and with an electrostatic parametric drive. Here we are interested in investigating the strength of the degenerate parametric drive when we apply a purely mechanical modulation and the role played by the mode geometries.

The first set of parametric measurements has been realized on a Dahlia generation 2 membrane. The presence of multiple bandgap modes allows us to compare the strength of the parametric phenomena on different modeshapes, thus geometries, with comparable mechanical properties within the same experiment run. We introduce the purely mechanical parametric modulation by gluing the membrane frame on a piezoelecric ring actuator. Every time we apply a voltage to the ring piezo it experiences an expansion (contraction) along the vertical axis and consequently the ring radius contracts (expands). As the ring radius changes, the membrane in-plane stress varies thanks to the gluing process.

To understand the amount of modulation the gluing process can introduce in the system, the first measurement we perform consists of applying a DC voltage to the ring piezo and monitoring the resonance frequency. We repeat the measurement for several voltages. The strength of such a frequency shift is strongly dependent on the gluing process and is not well reproducible from sample to sample. We observe frequency shifts from 50 Hz/V up to 500 Hz/V. Nevertheless, once the gluing process has been realized, we do not observe any relevant difference in the generated frequency shift among different modes. Examples of frequency shift measured on the first and the third bandgap mode of the same membrane are shown in Fig. 6.3. A comparable frequency shift between different modes of the same membrane has been consistently observed from sample to sample.

The frequency shift measured by applying a DC voltage determines the upper bound for the modulation we can produce with the piezo expansion. For the parametric protocol we operate the piezo at a frequency > 2MHz, well above the resonance frequency of the ring piezo. Thus we expect a reduction of the piezo expansion during the parametric drive due to the above-resonance operation. However, the parametric modulation generated by a given voltage between different modes should experience the same attenuation. From this preliminary measurement we do not expect any influence of the geometry on the elastic constant modulation. To verify this expectation we quantify the parametric driving strength on the first and third bandgap modes.

We quantify the parametric strength through the gain relations presented in Sec. 6.1. In particular we want to extract the parametric threshold from Eq. (6.12). The parameters we can vary are φ_r, φ_p and

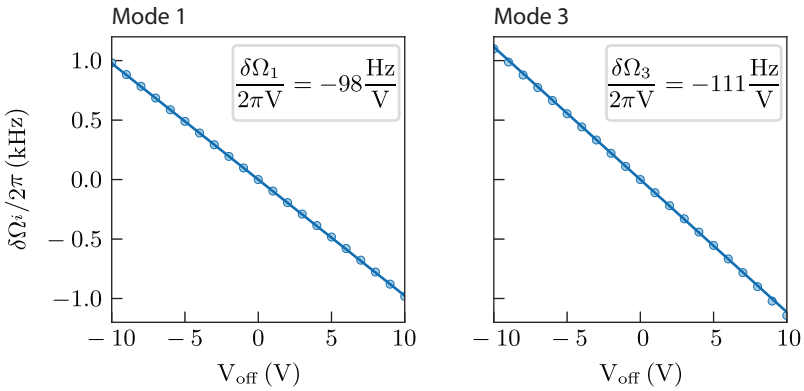

Figure 6.3: Frequency shifts produced by a DC voltage applied to a ring piezo. For each point we extract the peak frequency position from an FFT. Then we subtract it from the frequency peak position when no DC voltage is applied to derive the frequency shift. The solid line is a linear fit to extract the shift per unit voltage. On the left panel we report the data related to the first bandgap mode, on the right panel the data related to the third bandgap mode.

k_{p_i}. We can control the phase of both the resonant and the parametric drive through the lock-in amplifier. Currently, we do not have a way to directly quantify k_{p_i}. We set the amplitude voltage of the modulation, but we cannot directly translate it into an elastic constant modulation. We assume that the voltage applied is linearly transduced into an elastic constant modulation, meaning that $k_{p_i}/k_{th_i} = V_{p_i}/V_{th_i}$, where V_{p_i} is the voltage amplitude of the parametric drive and V_{th_i} is the voltage we need to apply in order to get a modulation of the elastic constant comparable with k_{th_i}.

In the measurement protocol, we need to drive the mechanical mode both resonantly and parametrically. Unwanted frequency detunings happening during the measurement time between the driving frequency and the mechanical frequency have to be smaller than the mechanical linewidth, only few tens mHz in our bandgap modes. Within the measurement time for the parametric measurement ($>$ 2min), the frequency fluctuations due to the instability of the ambient temperature and other sources of frequency noise introduce a frequency detuning larger than the mechanical linewidth (see Fig. 3.4 (a)).

To reduce the effects of frequency instability we mainly apply two techniques. First, we take advantage of the control we have on the in-plane stress to stabilize the frequency. We drive resonantly a second mode that we call *thermometer mode*, usually an out-of-bandgap mode. Monitoring the thermometer mode phase we generate an error signal that we send to a PID controller. The PID output is sent to the piezo to counteract the effect of the frequency drifts modifying the in-plane stress. To implement this method we need to have the interferometer in a homodyne detection scheme. Therefore, all the measurements in this chapter are realized in this configuration.

The second method we apply is a feedback scheme. We realize a mechanical feedback cooling scheme to broaden the linewidth of the mechanical mode and increase the tolerance to frequency fluctuations. The mechanical damping force is applied through the axial expansion of the piezo. Further details on the implementation and effectiveness of these two techniques can be found in Sec. 3.6. These two methods reduce the frequency drift to tens of mHz per minute. With a measurement time of $\approx 2\,\mathrm{min}$ we need to broaden the linewidth to at least $\Gamma_1/2\pi = 1\mathrm{Hz}$. We usually set the feedback in order to reach a quality factor $Q \approx 10^6$. If the feedback force is not enough to reach this value we increase the pressure in the chamber by reducing the rotational speed of the turbo pump, that is introducing an additional source of gas damping. More detail about the effect of gas damping can be found in Sec. 1.2.1 and 3.6. All the measurement discussed in this chapter are realized using the frequency stabilization methods, see Sec. 3.6.1. The feedback and the gas damping are introduced only if we need an additional damping to reduce the quality to $Q \approx 10^6$.

To estimate the parametric modulation on the modes of interest, we reproduce the theory curves presented in Fig. 6.1 for the more general case represented in Fig. 6.2. We can do so by recording the signal amplitude while sweeping either the phase or the amplitude of the parametric drive. We perform two types of measurement, the first of which we refer to as *parametric phase sweep*. We apply both a resonant and a parametric drive. The strength of the driving forces is constant throughout the whole measurement. We monitor the displacement amplitude while sweeping the phase of the parametric drive. The sweep is repeated for several parametric drive amplitudes. For each parametric drive amplitude we repeat the measurement 3 times and average the curves. We fit the curves using Eq. 6.12 multiplied by a pre-factor A_{0_i} that represents the amplitude without the parametric drive. During the sweep, we move along a horizontal line in Fig. 6.2. The phase of the resonant drive determines the height of the horizontal cut, i. e. changes the phase relative to the maximum amplification ($\varphi_\mathrm{p}^\mathrm{max}$) and deamplification ($\varphi_\mathrm{p}^\mathrm{min}$). The strength of the parametric drive defines the contrast. From the fit we extract A_{0_i} and $\mathrm{V}_{\mathrm{th}_i}$. From the latter we can extract k_{th_i} knowing the quality factor and the mechanical frequency. Then, comparing $\mathrm{V}_{\mathrm{th}_i}$ and k_{th_i}, we can calculate the conversion factor to derive the applied k_{p_i}.

The measurement of the displacement amplitude is subjected to fluctuations due to variation in the light intensity caused by polarization drifts or instabilities in the system. To correct for such fluctuations we save the amplitude of the thermometer mode during the sweep and use its fluctuations to extract a correction factor. In Fig. 6.4, we show the parametric phase sweeps for the first and third bandgap mode. Each curve is normalized with A_{0_i} extracted from the fit. From Fig. 6.4, we notice that the phase relative to the maximum amplification and

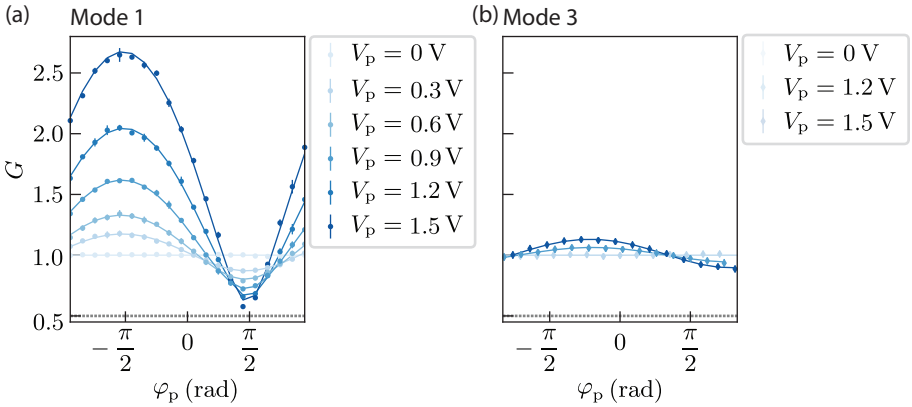

Figure 6.4: Parametric phase sweeps on the first (a) and third (b) bandgap mode. Each color represents a different driving strength. The points are the measured gains at a given phase, the solid lines are the best fit. The dotted grey lines represent the minimum gain ($G = 0.5$) we can reach before the instability regime.

deamplification are different in the two modes investigated. We attribute this phenomenon to different phase delays experienced by the resonant signal at two different frequencies. Furthermore, we notice a large difference between the parametric effects. After applying the feedback cooling, both the modes are characterized by $Q = 10^6$. From the measured the quality factor, the measured resonance frequency, and the simulated effective mass we can estimate the parametric threshold for the two modes $k_{\mathrm{th}_1} = (0.26 \times 10^{-3})$ N/m and $k_{\mathrm{th}_3} = (0.56 \times 10^{-3})$ N/m. From the predicted parametric threshold and the measured frequency shift in Fig. 6.3, we expect the parametric strength on the first mode to be around twice that of mode 3. Comparing the curves for 1.5 V parametric driving voltage, we observe that the gain for mode 3 is less than 1/2 the gain of mode 1.

To confirm the different magnitude of the parametric effects, we extract the voltage needed to reach the parametric threshold for the two modes. A more accurate measurement to extract $\mathrm{V}_{\mathrm{th}_i}$ is one we named *parametric amplitude sweeps*. As with the parametric phase sweeps, we drive a mechanical mode both resonantly and parametrically and monitor the displacement amplitude while we sweep one parameter. In this measurement, we sweep the amplitude of the parametric drive. For each measurement setting we perform two sweeps and we average the curves. For each mode we perform the amplitude sweeps at two phases of the parametric drive, one coinciding with the maximum amplification and the other with the maximum deamplification. We select these two phases from the phase sweeps in Fig. 6.4. We fit the two curves using Eq. (6.12). The measurement time for this sweep is shorter, and hence is less sensitive to frequency fluctuations. Therefore, we believe this

measurement is more robust for the estimation of V_{th_i}. The results are reported in Fig. 6.5.

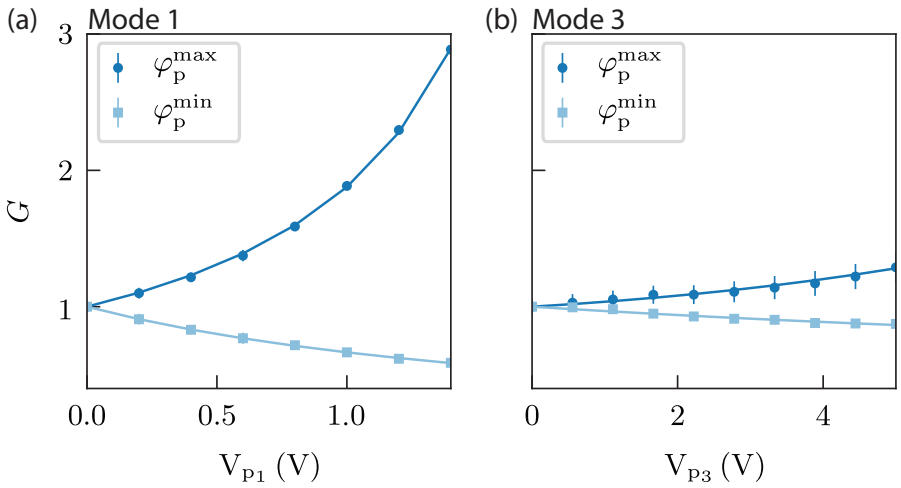

Figure 6.5: Parametric amplitude sweeps for the first (a) and third (b) bandgap mode as a function of the parametric drive amplitude. The dark (light) blue points (squared) are the measured gains for the parametric phase corresponding to the maximum amplification (deamplification), the solid lines are the best fits. From the best fit we derive $V_{th_1} = 2.5\,V$ and $V_{th_3} = 19.8\,V$.

From the best fit of the parametric amplitude sweeps in Fig. 6.5, we extract V_{th_i}. From the measured V_{th_i} and the estimated k_{th_i}, we derive a conversion constant in $N/m \cdot V$ that we use to estimate the resonance frequency modulation we generate by applying a given voltage $(k_p/2\Omega_i m_i)$. In particular for the first mode with a $V_{p_1} = 1.5\,V$, we derive a parametric modulation $k_{p_i}/2m_i\Omega_i \approx 1.2\,rad\,s^{-1}$ with a quality factor of 10^6. The authors in [H+21a] report a non-degenerate parametric strength $k_{p_i}/2m_i\Omega_i \approx 1.3\,rad\,s^{-1}$ for a dimer Lotus membrane with $Q \approx 10^8$ and an electrostatic drive of $V_p = 10\,V$

Interestingly, we find that the voltage needed to reach the threshold for mode 3 is almost 8 times higher than the one needed for mode 1, though we were expecting only a factor 2. Probably one of the assumptions we made in the above discussion is not correct. Our first hypothesis, the one that we investigate in the rest of the chapter, is that the modulation of the elastic constant k_{p_i} is not simply a linear transduction of the voltage as suggested by Fig. 6.3, but has a geometric source. From a parallelism with the optical spontaneous parametric down conversion [Fox06], we can describe a parametric amplification as a 3-wave mixing process where the energy of a pump mode (ω_p) is transferred to a signal (ω_s) and an idler mode (ω_i), which satisfies the frequency relation $\omega_p = \omega_s + \omega_i$. This modeling is particularly popular in the context of non-degenerate parametric oscillator $(\omega_s \neq \omega_i)$ both in electro- and optomechanical [Del+19; Bur+19] and purely mechanical

system [Mah+14; Pat+15; H¨21a]. To our knowledge, only in [Pat+15] a modeling and indirect measure of a mechanical pump mode has been provided. However, in our specific case, we cannot attribute the transfer of energy to the same source. Patil et al. in [Pat+15] attribute the energy transfer to a frame mode. We believe that the strong localization of the defect modes prevents an energy transfer between them and the frame. Moreover, if we monitor the displacement around the frequency of the parametric drive we do not see any mode excited or affected by the parametric motion. Instead we hypothesize that the pump mode is an in-plane membrane mode driven by the radial expansion of the piezo. Although they cannot be measured through standard interferometric techniques, we predict them through FEM simulation. In the following sections we first derive a continuum elastic modeling which includes the effect of the in-plane drive. In the last part of this chapter, we present the preliminary measurements carried out to prove the model.

6.3 CONTINUUM ELASTIC MODELING

We now derive a continuum elastic model to understand the effects of an in-plane force on the out-of-plane membrane motion. In Sec. 1.2 we derive the equation of motion when an out-of-plane force is applied by starting from the displacement vector and the stress-strain relation. Here, we generalize the model to include the contribution of an additional external force applied in the in-plane direction, and the contribution of the in-plane modes. The first key difference from the linear model can be found in the the displacement vector. In the linear case we perform the out-of-plane approximation and neglect the contribution of the in-plane displacement components v_x and v_y in Eq. (1.6). Instead, in the present case we assume the presence of an in-plane force stretching the membrane in the in-plane direction. Hence, the in-plane displacement components cannot be neglected. Using the displacement vector defined in Eq. (1.6) and imposing $\sigma_{iz} = 0$, we find that the strain tensor components defined in Eq. (1.7a) in the presence of the in-plane displacement contribution become

$$\varepsilon_{\alpha\beta} = \varepsilon_0 \delta_{\alpha\beta} + \frac{1}{2}\left(\partial_\alpha v_\beta + \partial_\beta v_\alpha\right) - z\partial_{\alpha\beta} w, \tag{6.17}$$

where the Greek indexes represent the two in-plane direction x and y. Notice that we are not including the elongation due to a large out-of-plane oscillation. Inserting Eq. (6.17) into Eq. (1.7b) we obtain the conservative stress tensor components

$$\begin{aligned}
\sigma_{xx}^{\text{cons}} &= \frac{E}{1+\nu}\varepsilon_0 + \frac{E}{1-\nu^2}\left(\partial_x v_x - z\partial_{xx} w + \nu\partial_y v_y - \nu z\partial_{yy} w\right), \\
\sigma_{yy}^{\text{cons}} &= \frac{E}{1+\nu}\varepsilon_0 + \frac{E}{1-\nu^2}\left(\nu\partial_x v_x - \nu z\partial_{xx} w + \partial_y v_y - z\partial_{yy} w\right), \\
\sigma_{xy}^{\text{cons}} &= \frac{E}{2(1+\nu)}\left(\partial_x v_y + \partial_y v_x - 2z\partial_{xy} w\right).
\end{aligned} \tag{6.18}$$

Following the approach presented in Sec. 1.2.1, we include the dissipative stress tensor through a time lag τ in the stress-strain relation, leading to the following dissipative stress tensor components:

$$\begin{aligned}
\sigma_{xx}^{\text{diss}} &= \frac{E\tau}{1-\nu^2}\left(\partial_x \dot{v}_x - z\partial_{xx}\dot{w} + \nu\partial_y \dot{v}_y - \nu z\partial_{yy}\dot{w}\right), \\
\sigma_{yy}^{\text{diss}} &= \frac{E\tau}{1-\nu^2}\left(\nu\partial_x \dot{v}_x - \nu z\partial_{xx}\dot{w} + \partial_y \dot{v}_y - z\partial_{yy}\dot{w}\right), \\
\sigma_{xy}^{\text{diss}} &= \frac{E\tau}{2(1+\nu)}\left(\partial_x \dot{v}_y + \partial_y \dot{v}_x + 2z\partial_{xy}\dot{w}\right).
\end{aligned} \tag{6.19}$$

From these stress components we can determine the stress resultants defined in Eq. (1.10), yielding to the equation of motion. In the situation we are describing there are two forces acting on the membrane resonator, one in the out-of-plane direction and one acting on both in-plane directions. With this condition, the equations of motion in terms of stress resultant takes the following form [TK87]:

$$\rho h\ddot{w} - \partial_{\alpha\beta}M_{\alpha\beta} - \nabla\cdot\vec{n} = F^{\text{res}}\cos(\Omega_{\text{r}}t + \varphi_{\text{r}}), \tag{6.20a}$$
$$\rho h\ddot{v}_1 - \partial_x N_{xx} - \partial_y N_{xy} = F^{\text{par}}\cos(\Omega_{\text{p}}t), \tag{6.20b}$$
$$\rho h\ddot{v}_2 - \partial_x N_{xy} - \partial_y N_{yy} = F^{\text{par}}\cos(\Omega_{\text{p}}t), \tag{6.20c}$$

where $\vec{n}$ is defined in Eq. (1.9). We assume that the parametric force has the same intensities in both the in-plane directions.

The bending momenta are not affected by the in-plane displacement terms. In contrast, the shear forces include such terms. We first find explicit expressions for $M_{\alpha\beta}$ and $N_{\alpha\beta}$ by substituting Eq. (6.18) and Eq. (6.19) in Eqs. (1.10). The resulting equation of motion is

$$\rho h\ddot{w} + D(\tau\partial_{\alpha\alpha\beta\beta}\dot{w} + \partial_{\alpha\alpha\beta\beta}w) - \nabla\cdot\vec{n} = F^{\text{res}}\cos(\Omega_{\text{r}}t). \tag{6.21}$$

The vector $\vec{n}$ can be written in matrix form as

$$\vec{n} = \begin{bmatrix} k_1\partial_x w\left(\varepsilon_0 + \partial_x(\mathcal{V}_x) + \nu\partial_y\mathcal{V}_y\right) + k_2\partial_y w\left(\partial_x\mathcal{V}_y + \partial_y\mathcal{V}_x\right) \\ k_1\partial_y w\left(\varepsilon_0 + \partial_y\mathcal{V}_y + \nu\partial_x\mathcal{V}_x\right) + k_2\partial_x w\left(\partial_x\mathcal{V}_y + \partial_y\mathcal{V}_x\right) \end{bmatrix}, \tag{6.22}$$

where $k_1 = Eh/(1-\nu^2)$, and $k_2 = Eh/2(1+\nu)$. Moreover we performed the following substitution:

$$\mathcal{V}_x = v_x + \tau\dot{v}_x, \tag{6.23a}$$
$$\mathcal{V}_y = v_y + \tau\dot{v}_y. \tag{6.23b}$$

Looking at Eq. (6.22), we recognize that it contains coupling terms between in-plane and out-of-plane displacement proportional to wv_x and wv_y. To write the equation of motion for the out-of-plane modes in a more familiar form, we need to find an expression for the in-plane displacement components. To do this, we write Eq. (6.20b) and Eq.

(6.20c) in terms of the in-plane displacement components. After some algebraic manipulation we obtain the following equations:

$$\rho h\ddot{v}_x - (k_1\partial_{xx} + k_2\partial_{yy})\mathcal{V}_x + (-k_1\nu\partial_{xy} + k_2\partial_{yy})\mathcal{V}_y + \\ - h\partial_x\sigma_0 = F^{\text{par}}\cos(\Omega_{\text{p}}t), \tag{6.24a}$$

$$\rho h\ddot{v}_y - (k_1\nu\partial_{xy} + k_2\partial_{xx})\mathcal{V}_x - (k_1\partial_{yy} - k_2\partial_{xx})\mathcal{V}_y + \\ - h\partial_y\sigma_0 = F^{\text{par}}\cos(\Omega_{\text{p}}t). \tag{6.24b}$$

The above equations are not trivial to solve. However, we notice that they are two linear differential equations in v_x and v_y. Similarly to the out-of-plane displacement field w, we can separate the spatial and the temporal dependence of the in-plane displacement and expand the former over a basis of in-plane normalized mode $v_x(x,y,t) = \psi_{x_m}(x,y)\nu_{x_m}(t)$ and $v_y(x,y,t) = \psi_{y_m}\nu_{x_m}(t)$. Then we can apply the Galerkin method and the single mode approximation [You11] choosing as a test function the normalized mode ϕ_d with the mechanical frequency closer to Ω_{p}. We use the subscript d to refer to the excited in-plane mode. After this transformation, the Eqs. (6.24) can be interpreted as two linear coupled harmonic oscillators. Without de-coupling and solving the two equations, we can say that v_x and v_y are the two components of an in-plane vector $\vec{v} = (v_x, v_y) = (\psi_{x_m}\nu_{x_m}, \psi_{y_m}\nu_{y_m})$ whose dynamics is described by the coupled harmonic Eqs. (6.24). Therefore, we can write the displacement vector $\vec{v}$ as following

$$\vec{v}(x,y,t) = \vec{\psi}_d(x,y)\underbrace{\vec{\nu}_{d,0}\cos(\Omega_{\text{p}}t + \Phi)}_{\vec{\nu}_d(t)} \tag{6.25}$$

where we assume only one mode $\vec{\psi}_d$ gives a non-negligible contribution to the in-plane displacement. $\vec{\nu}_{d,0}$ represents the displacement amplitude of the driven in-plane mode. It depends on the parametric force applied and we assume it to be constant constant. The two x and y components can be written as $v_{d_x} = \psi_{d_x}\nu_{d,0}\cos(\Omega_{\text{p}}t + \Phi)$ and $v_{d_y} = \psi_{d_y}\nu_{d,0}\cos(\Omega_{\text{p}}t + \Phi)$. For simplicity, we assume the displacement amplitude in the two in-plane directions coincides. In principle, we could also include the possibility of having multiple in-plane modes excited at the driving frequency by considering a superposition of modes v_i with weights c_i, i. e.

$$\vec{v} = \vec{\nu}_{i,0}\cos(\Omega_{\text{p}}t + \Phi)c_i\vec{\psi}_i(x,y),$$

where the repeated indexes are summed over. We decide to neglect the influence of multiple in-plane modes. For the current treatment we write $\vec{v}$ as expressed in Eq. (6.25).

We can use Eq. (6.25) to describe the in-plane displacement. Now we go back the equation of motion for the out-of-plane modes, i. e. Eq. (6.21). At first we expand w in the latter equation over a basis

of normalized modes,$w = \phi_n(x,y)u_n(t)$. Similar to the modeling in Chapter 1 and Chapter 4 we use the convention $\phi_n^{\max} = 1$. Then, we apply the Galerkin method choosing as a test function the normalized mode ϕ_i

$$\rho h \ddot{u}_n \int_S \phi_i \phi_n dS + D\tau \dot{u} \int_S \phi_i \partial_{\alpha\alpha\beta\beta}\phi_n dS + D u_n \int_S \phi_i \partial_{\alpha\alpha\beta\beta}\phi_n dS + \\ - \int_S \phi_i \nabla \cdot \vec{n} dS = \int_S \phi_i F^{\text{res}} \cos(\Omega_{\text{r}} t + \varphi_{\text{r}}) dS. \tag{6.26}$$

On the last term on the left hand side of the equation we can apply the divergence theorem, see Eq. (1.20).

$$\rho h \ddot{u}_n \int_S \phi_i \phi_n dS + D\tau \dot{u} \int_S \phi_i \partial_{\alpha\alpha\beta\beta}\phi_n dS + D u_n \int_S \phi_i \partial_{\alpha\alpha\beta\beta}\phi_n dS + \\ \int_S n_x \partial_x \phi_i dS + \int_S n_y \partial_y \phi_i dS = f_i^{\text{res}} \cos(\Omega_{\text{r}} t + \varphi_{\text{r}}) \tag{6.27}$$

Finally, we substitute all the v_x and v_y in n_α with the two components of Eq. (6.25), and we perform the single mode approximation. After some algebraic manipulation, we obtain an effective equation describing the dynamics of the system when we are introducing an in-plane force

$$\ddot{u}_i + \Gamma_i \dot{u}_i + \Omega_i^2 u_i + \nu_{i,0}\lambda_i u_i \cos(\Omega_{\text{p}} + \Phi) + \\ + \nu_{i,0}\lambda_i \tau \Omega_{\text{p}} u_i \sin(\Omega_{\text{p}} t + \Phi) = f_i^{\text{res}} \cos(\Omega_{\text{r}} t + \varphi_{\text{r}}), \tag{6.28}$$

with $f_i^{\text{res}} = \int_S \phi_i F^{\text{res}} dS$. The symbol λ_i represents the spatial overlap between the in-plane and the out-of-plane modes and has the following form

$$\lambda_i = \frac{k_1}{m_i} \int_S \left[(\partial_x \phi_i)^2 \left(\partial_x \psi_{d_x} + \nu \partial_y \psi_{d_y} \right) + (\partial_y \phi_i)^2 \left(\nu \partial_x \psi_{d_x} + \partial_y \psi_{d_y} \right) \right] dS + \\ + \frac{k_2}{m_i} \int_S \left[\partial_x \phi_i \partial_y \phi_i \left(\partial_x \psi_{d_y} + \partial_y \psi_{d_x} \right) \right] dS, \tag{6.29}$$

while all the other effective parameters coincide with the ones evaluated in Sec. 1.2. We can manipulate Eq. (6.28) further to combine the last two terms on the left hand side. We notice that if we choos $\Omega_{\text{p}} = 2\Omega_i$, we can write $\tau\Omega_{\text{p}} = 2\tau\Omega_i = 2\theta_{\text{lin}}$, where θ_{lin} is the linear loss angle we discussed at the end of Chapter 4. In the case of a SiN membrane with thickness $h \leq 100\,\text{nm}$ we set $\theta_{\text{lin}} \ll 1$, as seen from Eq. (1.48) and as confirmed by the measurements presented in Sec. 4.5. Therefore, we can make the following approximations:

$$\sin(2\tau\Omega_i) \approx 2\tau\Omega_i, \tag{6.30a}$$

$$\cos(2\tau\Omega_i) \approx 1. \tag{6.30b}$$

Using Eqs. (6.30) and the trigonometric identity $\cos(\alpha-\beta)=\cos(\alpha)\cos(\beta)+\sin(\alpha)\sin(\beta)$ in Eq. (6.28), we obtain the effective equation

$$\ddot{u}_i+\Gamma_i\dot{u}_i+\Omega_i^2u_i+v_{i,0}\lambda_i\cos(\Omega_{\mathrm{p}}t+\underbrace{\Phi-2\tau\Omega_i}_{\varphi_{\mathrm{p}}})u_i=f_i^{\mathrm{res}}\cos(\Omega_{\mathrm{r}}t). \tag{6.31}$$

By choosing $\Omega_{\mathrm{p}}=2\Omega_i$ and $\Omega_{\mathrm{r}}=\Omega_i$ and including a resonant phase to the out-of-plane force φ_{r}, we recover the equation of motion of the parametrically-driven harmonic oscillator presented in Eq. (6.1). The modulation of the elastic constant is $k_{\mathrm{p}}=\nu_{i,0}\lambda_i$. It is constituted by two components: one is the displacement amplitude of the in-plane mode, while the other is the spatial overlap between in-plane and out-of-plane motion. The result above can be further generalized to the nondegenerate parametric case. If we assume a parametric drive $\Omega_{\mathrm{p}}=\Omega_{\mathrm{i}}+\Omega_{\mathrm{s}}$ and include intermodal coupling term between the idler and the signal, we get two equations of motion, one for the idler and one for the signal, including a parametric modulation which depends on the spatial overlap between the three modes

$$\begin{aligned}\lambda_{is}=&\frac{k_1}{m_i}\int_S\partial_x\phi_i\partial_x\phi_s\left(\partial_x\psi_{d_x}+\nu\partial_y\psi_{d_y}\right)dS+\\&+\frac{a_1}{m_i}\int_S\partial_y\phi_i\partial_y\phi_s\left(\nu\partial_x\psi_{d_x}+\partial_y\psi_{d_y}\right)dS+\\&+\frac{k_2}{2m_i}\int_S\left[\left(\partial_x\phi_i\partial_y\phi_s+\partial_y\phi_i\partial_x\phi_s\right)\left(\partial_x\psi_{d_y}+\partial_y\psi_{d_x}\right)\right]dS.\end{aligned} \tag{6.32}$$

A more detailed analysis of the nondegenerate situation will be investigated in future works.

6.4 RESONANTLY-ENHANCED PARAMETRIC STRENGTH

We now investigate the meaning of the model presented in the previous section and we show the preliminary measurements made to confirm it. As in the rest of the chapter, we focus on the degenerate parametric case.

The treatment above suggests that the modulation of the elastic constant is generated by a coupling term between the in-plane and the out-of-plane motion. When the in-plane mode driving frequency coincides with twice the resonance frequency of the out-of-plane mode, such modulation enables a parametric drive. This means that the modulation of the elastic constant does not depend directly on the amplitude of the parametric force applied, as we thought at the beginning. The modulation of the elastic constant is determined by both the spatial overlap between the in-plane and the out-of-plane mode (λ_i), and by the displacement amplitude of the in-plane mode ($\nu_{i,0}$). Let us analyze how these two contributions affect the elastic constant modulation separately.

We consider the effect of the spatial overlap λ_i. The presence of this term implies that some combination of modes may introduce a stronger modulation than others. For instance, we expect an in-plane mode translating the defect along an in-plane axis will generate a smaller parametric modulation compared to an in-plane mode stretching the defect radially. To measure λ_i and compare it with FEM simulation, we need to separate it from $\nu_{i,0}$. This would require the possibility of measuring a calibrated displacement amplitude $\nu_{i,0}$. However, the detection of in-plane mode displacement is currently not possible in our system. Moreover, the validity of the in-plane mode simulation is still to be verified. One of the future development of this project consists in implementing an alternative detection scheme sensible to in-plane displacements.

We now clarify the role played by $\nu_{i,0}$. As we discussed in Sec. 6.1, we recognize that for a given parametric force the amplitude response of the in-plane mode depends on the proximity between the parametric drive frequency and the mode resonance frequency. In particular, the closer the drive frequency to the resonance, the larger the displacement. The response has a Lorentzian shape and is shown in Fig. 6.6 (a). We usually work with an out-of-plane mode linewidth $\Gamma_i/2\pi < 10\,\mathrm{Hz}$. Although we expect a broader resonance for the in-plane mode, the probability of having an in-plane mode with a resonance frequency coinciding with $2\Omega_i$ is extremely low. Let us call the resonance frequency of the in-plane mode Ω_{in}. If we can act on one or both the frequencies of interest in order to match the condition $\Omega_{\mathrm{in}} = 2\Omega_i = \Omega_{\mathrm{p}}$, we should observe an increase of the elastic constant modulation for the same applied force (see Fig. 6.6 (a)). Conversely, increasing the frequency mismatch should reduce the modulation.

Due to the frequency dependence of the modulation, we do not know how the voltage $\mathrm{V_{p_i}}$ output from the instrument is translated into a modulation k_{p_i} for different detunings. In contrast, the parametric threshold constant should not be affected by the resonance condition. Therefore, we can say that as we go closer to resonance the ratio $k_{\mathrm{p}_i}/k_{\mathrm{th}_i} = \mathrm{V}_{\mathrm{p}_i}/\mathrm{V}_{\mathrm{th}_i}$ increases and vice versa. Using the voltage output by the instrument as $\mathrm{V}_{\mathrm{p}_i}$ in Eq. (6.12), an increment of the elastic constant modulation is translated into a smaller effective $\mathrm{V}_{\mathrm{th}_i}$, while a reduction of the modulation into a larger $\mathrm{V}_{\mathrm{th}_i}$ (see Fig. 6.6 (b)). We could collect a first evidence of the presence of the $\nu_{i,0}$ contribution to the parametric mechanism by observing a variation of the effective threshold voltage as we pass through the resonance of the in-plane mode.

To hit the resonance condition, we need to act on the resonance frequency of the modes involved. One method is to tailor the membrane design, so that the desired in-plane mode resonances are obtained. This would require accuracy of the predictions of the out-of-plane and in-plane mode frequencies comparable with the required tolerance of 10 Hz, which

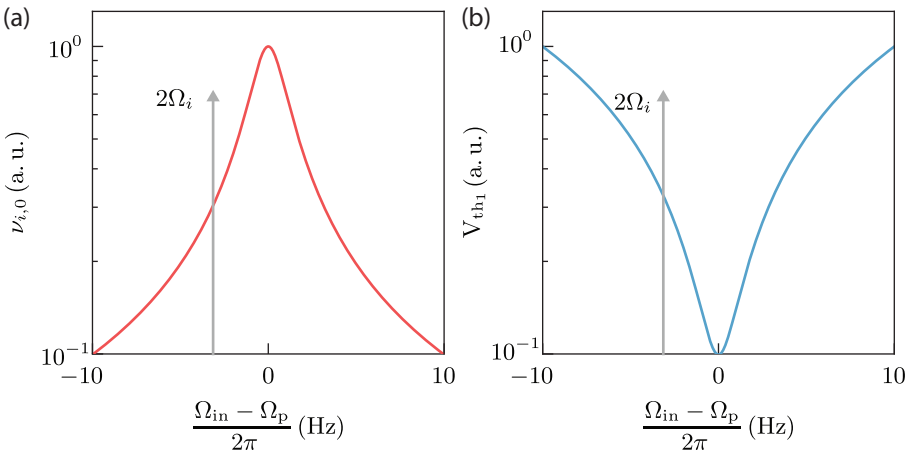

Figure 6.6: Resonantly enhanced parametric strength. (a) Driven response of the in-plane mode amplitude. The grey arrow represents the frequency corresponding to twice the resonance frequency of the out-of-plane mode, i. e. the parametric drive frequency Ω_p. If we tune the latter such that we match the resonance condition of the in-plane mode resonance, the amplitude $\nu_{i,0}$ (and the parametric modulation k_{p_i}) increases without applying a larger parametric force. (b) Effective threshold response. As the frequency $2\Omega_i$ enters the resonance condition the ratio k_{p_i}/k_{th_i} increases, hence the ratio V_{p_i}/V_{th_i} increases as well. Using the driving voltage V_{p_i} output by the instrument as measurement variable, the effect is translated into a reduction of V_{th_i}.

is beyond our fabrication control. We routinely measure fluctuations of the order of few kHz around the simulated values of the out-of-plane modes frequencies due to variations during the fabrication process. Moreover, we are still missing the information about the accuracy of the in-plane mode frequencies, and the membrane handling and gluing process can reduce the frequency in an unpredictable way. For all of the above reasons, our control on the in-plane and out-of-plane mode frequencies currently is not good enough to observe the expected resonant enhancement optimizing membrane design.

To have first evidence of the validity of the model, we need to tune the resonance frequencies of either the in-plane or the out-of-plane mode within the same sample. If this was the case, we would observe a correlation between threshold voltage and resonance condition proving the correctness of our model. Once again, we use the control we have of the in-plane stress through the glued frame. From Eq. (1.24) and Fig. 6.3, we know that the mechanical frequency of the out-of-plane mode varies with the in-plane stress. On the other hand, in Eqs. (6.24) we observe that the in-plane stress is acting as a constant displacement-independent force, therefore it should not affect the mechanical frequency. We confirm this observation through FEM simulation. A 10% variation in the tensile stress modifies the out-of-plane modes resonance frequencies by ≈ 60kHz

while the in-plane modes resonance frequencies are shifted by $\approx 100\,\mathrm{Hz}$. Therefore by applying a DC voltage to the piezo we change the resonance frequency of the out-of-plane mode, i. e. the parametric drive frequency, without changing the in-plane mode frequency. If the model in Sec. 6.3 is correct and we are close enough to the in-plane mode frequency, we should observe a variation of the extrapolated threshold voltage as we change the DC voltage.

We verify the variation of the threshold voltage with the tuning of the mechanical frequency of the out-of-plane mode. We shift the resonance frequency of the out-of-plane mode by applying a DC voltage on a range going from $-25\,\mathrm{V}$ to $25\,\mathrm{V}$. Since the maximum voltage allowed by the HF2LI is $\pm 10\,\mathrm{V}$, we use a piezo amplifier to increase the voltage range. In principle we could apply a higher voltage, but the heating induced by the piezo makes the system too unstable to perform the measurement. For each DC voltage, we measure the frequency shift by comparing the peak position on the FFT with and without any voltage applied and we perform an amplitude sweep measurement as described in Sec. 6.2 to extract $\mathrm{V_{th_i}}$. Moreover, we perform a ringdown measurement to verify that the quality factor is not affected in a significant way by the in-plane stress variation (see Sec. 1.2.4 for the definition of the ringdown measurement). We perform this set of measurements on the first and the third bandgap mode.

The results are shown in Fig. 6.7. For the first bandgap mode (Fig.

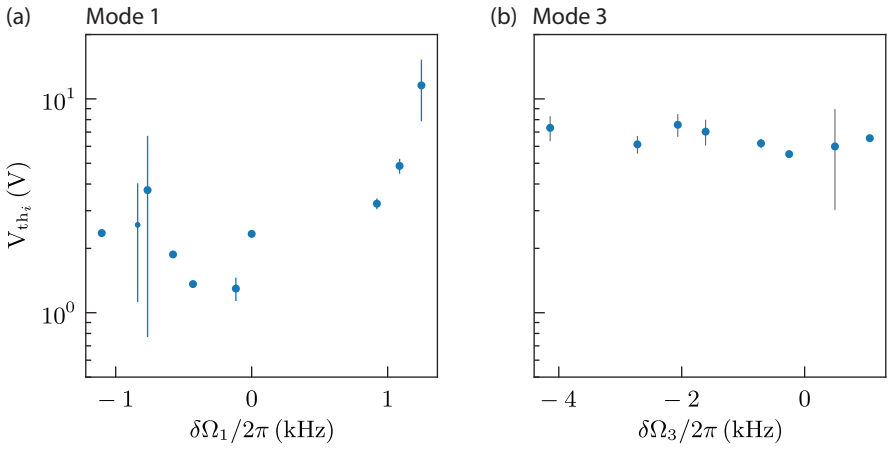

Figure 6.7: Resonantly enhanced parametric effects. We show $\mathrm{V_{th}}$ against frequency detuning on the first (a) and third (b) bandgap mode. Each point is the measured $\mathrm{V_{th_i}}$ extracted from two repetitions of amplitude sweeps.

6.7 (a)) we observe a variation of $\mathrm{V_{th_i}}$. It increases for increasing frequencies, while the data suggests that the parametric threshold does not decrease for negative detunings. We do not have enough data to confirm the model, but this might indicate that we are close to the resonance condition. In the third bandgap mode (Fig. 6.7 (b)), we do not measure any significant variation in $\mathrm{V_{th_i}}$ suggesting that for this

mode we are far away from the resonance condition. The suggested resonance conditions are consistent with the different magnitude of the two parametric strengths between the two modes reported in Fig. 6.4 and Fig. 6.5.

The detuning range we can reach through the DC voltage is limited and we have not yet succeeded in finding a membrane where the frequencies are such that we can see V_{th_i} crossing an in-plane mode resonance. However, we recognize a second feature suggesting the mechanism behind this parametric drive is the one presented in Sec. 6.3. Assuming the phase of the parametric drive coincides with the one we defined on the HF2LI, during the phase sweep measurement the φ_p^{max} and φ_p^{min} position depends only on the constant resonant phase. However, from the model presented in Sec. 6.3, the phase set on the instrument defines only the phase of the in-plane drive. The parametric force phase is then determined from the phase response of a harmonic oscillator. Following the same argument as the one advanced for $\nu_{i,0}$, φ_p should change as we enter in resonance with the in-plane mode drive, accordingly with the trend reported in Fig. 1.3 (b). In our phase sweep measurements, this is translated into a shift of φ_p^{max} and φ_p^{min}. Therefore, by monitoring the minimum (or maximum) phase position as a function of the frequency detuning we should recover the phase response reported in Fig. 1.3 (b).

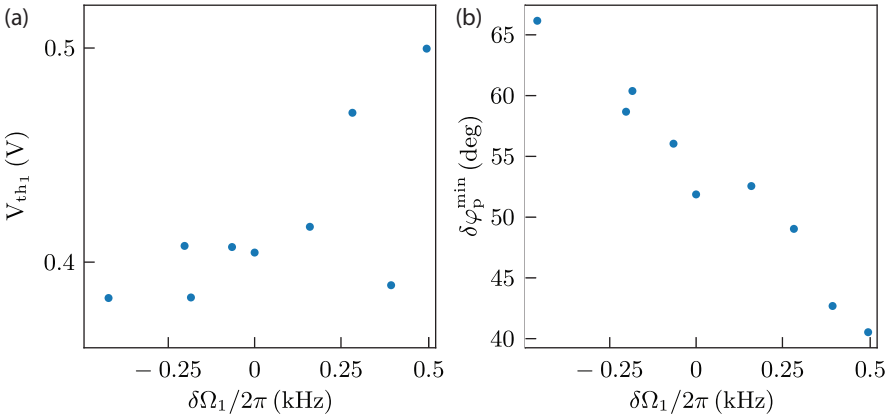

Figure 6.8: Resonantly enhanced parametric strength on Dahlia generation 2 membrane nominally identical to the one used in Fig. 6.7. (a)V_{th_i} against the frequency detuning of the first bandgap mode. Notice that the V_{th_i} decreases going towards smaller frequencies consistently with the previous sample where the resonance frequency was slightly smaller. (b) Measured phase shift against the frequency detuning on the first bandgap mode.

Unfortunately, we do not have the phase information on the membrane used for the previous data in this chapter. We attempt to confirm our hypothesis by repeating the measurement on other two membrane resonators. The first one is a Dahlia generation 2 membrane, nominally identical to the one used in this chapter and fabricated during the same fabrication run. During the membrane handling the quality factor of

this sample reduces to $Q = 1.8 \times 10^6$ and the gluing results in frequency shift of only $\pm 20\,\mathrm{Hz/V}$. In Fig. 6.8, we show $\mathrm{V_{th_i}}$ (left panel) and the phase shift of $\varphi_\mathrm{p}^\mathrm{min}$ (right panel) against the frequency detuning. Notice that the mechanical frequency of this membrane is $\approx 100\,\mathrm{Hz}$ larger than the one used for the data in Fig. 6.7.

The second membrane we characterize is a 50 nm-thick Lotus membrane with a quality factor of $Q = 39 \times 10^6$ (with both feedback and gas damping applied). For this sample we manage to get a frequency shift of $500\,\mathrm{Hz/V}$. In Fig. 6.9 we show $\mathrm{V_{th_i}}$ (left panel) and the phase shift of $\varphi_\mathrm{p}^\mathrm{min}$ (right panel) against the frequency detuning.

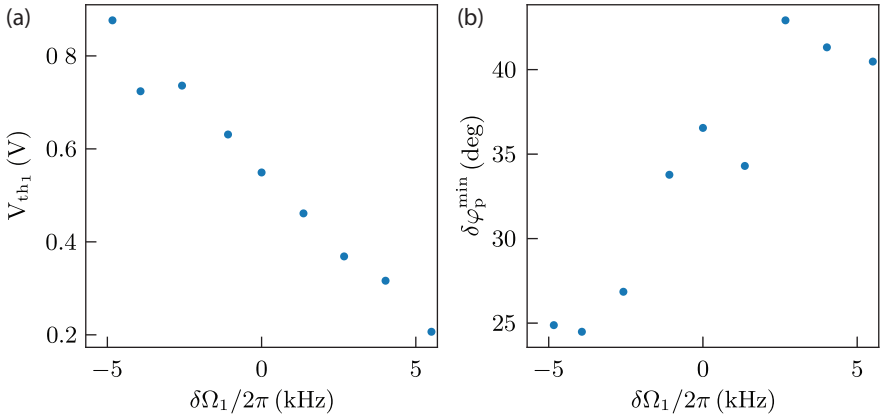

Figure 6.9: Resonantly enhanced parametric strength on a Lotus membrane. (a) $\mathrm{V_{th_1}}$ against the frequency detuning of the only bandgap mode. (b) Measured phase shift against the frequency detuning on the only bandgap mode.

We want to mention that the measurement procedure for the amplitude and the phase sweeps used to extract the data in Fig. 6.8 and Fig. 6.9 have been realized with a slightly different procedure. To minimize the effect of the residual frequency drifts instead of using the sweeper option of the HF2LI, we extract the amplitude at different phases (or driving strength) from the electronic quadratures. Between each phase (driving) steps, we turn off the drive and optimize the resonance condition.

Overall, the set of data presented we observe some indication that the model presented is describing the parametric mechanism in a qualitative way. In all the studied samples, the variation of the measured $\mathrm{V_{th_i}}$ as a function of the frequency detuning suggests different resonant conditions. This observation is corroborated by the measured phase shift and is consistent with comparison between different parametric strength within modes of the same membrane. However, to confirm the model, a larger frequency tuning range is required. In Appendix C we show the first attempt toward a wider temperature mediated frequency tuning.

CONCLUSION & OUTLOOK

Nanomechanics is a young yet very active research field, which is of interest for both technological applications and fundamental research. The work presented in this thesis collocates itself at the intersection between the two interests.

We now summarize the main results presented in this thesis. Building on a continuum elastic model, we formulate a theory for the motion of a thin membrane under large deflections. In this regime, the structural elongation generates both conservative and dissipative nonlinear terms in the dynamics. These terms, of common geometric origin, appear in the equations of motion as a Duffing frequency shift and a nonlinear damping term. The solution of the equations of motion guided us to developing an experimental protocol to measure the nonlinear parameters. We perform these measurements on various soft-clamped membrane geometries, and we find good agreement with FEM simulations. Our theory predicts that the above-mentioned geometric nonlinearities are simply related to the linear loss angle. We compare the predicted loss angle from the measured nonlinear parameters to a phenomenological model, finding an overall good agreement.

Then, we perform a similar study in a novel geometry of membranes, called soft-clamped phononic dimers, characterized by two identical defects embedded in the same phononic crystal. Intuitively, the modes of the two defects couple to each other through the common substrate, thus leading to a mode frequency splitting. This splitting can be widely tuned acting on the geometry without affecting the quality factor. We measure the Duffing nonlinearity and the nonlinear damping with the tools we developed with the single-defect membrane. In addition, we model and measure the cross nonlinearities between the two defects, a new effect peculiar to dimeric resonators.

Nonlinearities are also responsible for parametric effects, such as a modulation of resonance frequencies which finds its use in parametric amplification. We investigate the strength of a parametric modulation of the resonance frequency realized through an in-plane force exerted by the radial expansion of a ring piezo. Comparing the parametric amplification on two bandgap modes, we observe a geometric dependence of the in-plane force actuated frequency modulation. To explain this geometric dependence, we extend the continuum elastic model to include in-plane modes as well. We predict that in-plane modes can resonantly-enhance the paramtric driving done with the piezo. From preliminary measurements, we collect some evidence that tuning the in-plane mode resonance frequency indeed enhances the modulation strength. This is a promising way to achieve strong parametric modulation, and will be the subject of future studies.

In conclusion, we developed a set of measurement tools we can use to characterize different types of nonlinear phenomena on dissipation-diluted nanomechanical resonators. We showed different ways to generalize a linear continuum elastic model to describe and simulate different types of nonlinear phenomena and we prove it on a vast number of geometries, different modeshapes on both single- and double-defect designs, and thicknesses. This thesis adds experimental and theoretical evidences about the origin of geometric nonlinearities in dissipation-diluted nanomechanical resonators and give some insight on the performances of these resonators which can contribute to the realization of new geometries. Understanding the source of nonlinearities is important to control them. For instance, one could minimize the nonlinearities in force sensing application [Koš+20], where they limit the force sensitivity, or enhance them in quantum experiments, where the enhanced nonlinearities could enable the generation of genuine nonclassical features of motion [Ros19].

The thesis results presented are interesting for future developments for both classical and quantum applications. We elaborate now on some of the continuation of the work initiated within this thesis.

NANOMECHANICAL OSCILLATORS FOR FORCE SENSING APPLICATIONS

The high quality factor achieved in the soft-clamped membranes makes these resonators studied a very promising platform for force sensing experiments. The typical force sensitivity is of the order of tens of $\mathrm{aN}/\sqrt{\mathrm{Hz}}$ at room temperature, in spite of a large effective mass in the range of ng. As a matter of fact, the projected force sensitivity at cryogenic temperature for the geometries currently employed in our research group is approaching the force sensitivity of the state-of-the art nanomechanical oscillators currently used in force sensing experiments [MR01; Tao+14; Hér+18].

In Table 6.1, we compare the mechanical properties of different nanomechanical resonators. In particular, we compare state-of-the art nanomechanical resonators routinely used for force sensing applications with the new generation of soft-clamped nanomechanical resonators developed during the recent years. From Table 6.1 it is evident that the main advantage of our mechanical resonators is the large working area. Additionally our resonators, similarly to all the new generation of nanomechanical resonators developed in the last years, feature a resonance frequency in the range of MHz, higher than the one of state-of-the-art resonators normally used for sensing applications. Working with a higher frequency is advantageous because it is less subjected to technical noises and it introduces lower non-contact friction.

	m (pg)	$\Omega/2\pi$ (kHz)	Q (M)	h (nm)	Area(μm $\times$ μm)	$\sqrt{S_{FF}}$ (aN/$\sqrt{\text{Hz}}$)	
						300 K	4 K
Dahlia gen. 1[a]	16000	777	214	35	**200 × 200**	55	**4.1**
Dahlia gen. 2[b]	2310	1130	1030❄	20	**200 × 200**	25	**0.8**
Phon. dimer[c]	1870	1311	93	14	**2(200 × 200)**	28.2	**1.5**
Lotus − metal.[d(*)]	15	1487	1500❄	63	**80 × 80**		**0.65**
Nanoladder (diam.)[e]	4.1	25.22	0.162❄	100	**3 × 3**	9.9	**0.77**
Rec. beam (diam.)[e]	1600	32.14	6❄	660	**240 × 12**	81	**4.2**
Nanoladder (Si)[f]	5.5	5.52	0.045❄	100	**3 × 3**	11	**0.85**
Rec. beam (Si)[g]	270	4.98	0.150❄	290	**260 × 2.9**		**3.3**
Soft − clamp string[h]	5	2500	100	20	**60 × 1**	2.1	**0.2**
Snow − flakes[i]	9	1650	6.6❄	100	**30 × 30**	21	**4.2**
Bin. tree membr.[l]	260	100	230	20	**35 × 35**	2.6	**0.16**
Str. cryst. string[m]	4	1400	6300❄	12	**200 × 1**	0.65	**0.022**
Polygon resonator[n]	18	350	3600	20	**4(700 × 0.2)**	0.292	**0.019**

Table 6.1: Overview of the state-of-the-art nanomechanical oscillators for force sensing applications. We compare the force sensitivity for the membrane resonators developed in our group (highlighted in red) with the ones normally used in force sensing applications (highlighted in blue). For comparison, we include the force sensitivity of the new generation of nanomechanical oscillators promising for force sensing applications. We use Eq. (1.37) to express the force sensitivity. The force sensitivities highlighted in green are projected assuming an increment of a factor three of the quality factor. We report only the highest force sensitivity values stated in literature. The snowflake symbol next to the quality factors identify the quality factor measured at cryogenic temperature. (*) The cryogenic temperature for this particular device is 30mK. The superscript coincides with the following references: a=[Tsa+17], b=[Ros+18], c=[CTS20], d=[Sei+21], e=[Hér+18], f=[Tao+14], g=[MR01], h=[Gha+18], i=[Ree+19], l=[Bec+21a], m=[Bec+21b], n=[Ber+21].

.

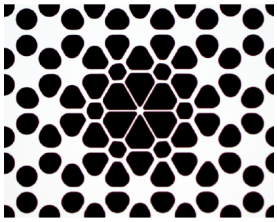

Dandelion [H+̈21b].

The membrane design can be optimized to improve the force sensitivity. We are now developing new designs which features a low effective mass for the defect modes [H+̈21b]. We refer to this particular type of resonators as *dandelion membranes*. Its defect supports two bandgap modes. Notably, the bandgap mode relevant for sensing application, i. e. the one where the maximum displacement point is on the pad, is centered within the bandgap. The central defect pad has a diameter which can be tuned in the range $18 - 36\mu$m. We successfully fabricated a 50 nm-thick membranes. The defect mode has an effective mass of 0.1 ng and a mechanical frequency of 1.6 MHz. At room temperature we measure a quality factor of 15.1 M, corresponding to $\sqrt{S_{\mathrm{FF}}} = 23\,\mathrm{aN}/\sqrt{\mathrm{Hz}}$ [H+̈21b]. The projected force sensitivity for dandelion membrane with a thickness of 15 nm at 4 K is $\sqrt{S_{\mathrm{FF}}} = 330\,\mathrm{zN}/\sqrt{\mathrm{Hz}}$ for the smaller defect and $\sqrt{S_{\mathrm{FF}}} = 500\,\mathrm{zN}/\sqrt{\mathrm{Hz}}$ for the larger one.

Let us now discuss about the possibilities associated with a large working area. It gives us the option to separate the position where the force is applied and where the motion is the readout. This precaution would help to avoid damages on the structure producing the force, e. g. biological samples or superconducting chips. This configuration has already been tested successfully in a force microscopy experiment involving a phononic membrane device as a force sensor by D. Hälg, et al. in [H+̈21b]. In Fig. 6.10 (a),(b) we report the experimental setup the authors used, while in Fig. 6.10 (c) we show the main results, that is a topographic imaging of a set of gold nanoparticles and tobacco mosaic viruses (TMV) deposited on the membrane surface. Moreover, having a large working area makes easier the integration of an optical cavity to measure the motion with higher sensitivity.

Among all our devices, the phononic dimers are promising for particularly demanding force sensing experiments such as MRFM. Here the resonance frequency of the nanomechanical resonator needs to match the spin inversion frequency [Deg+09]. For the magnetic field routinely used in MRFM experiments, the spin inversion happens at a frequency in the kHz range, as can be observed from Table 6.1, well below the resonance frequency of the soft-clamped membranes. Nevertheless, the presence of multiple high-Q bandgap modes enables the possibility of implementing non-degenerate parametric sensing protocol where the pump mode frequency can be matched to the spin inversion frequency. The performance of this protocol with phononic dimer membranes has been evaluated in a theoretical work by J. Košata et al. in [Koš+20], and initial experimental results on the strength of an up-conversion non-degenerate parametric protocol has been presented by D. Hälg et al. in [H+̈21a].

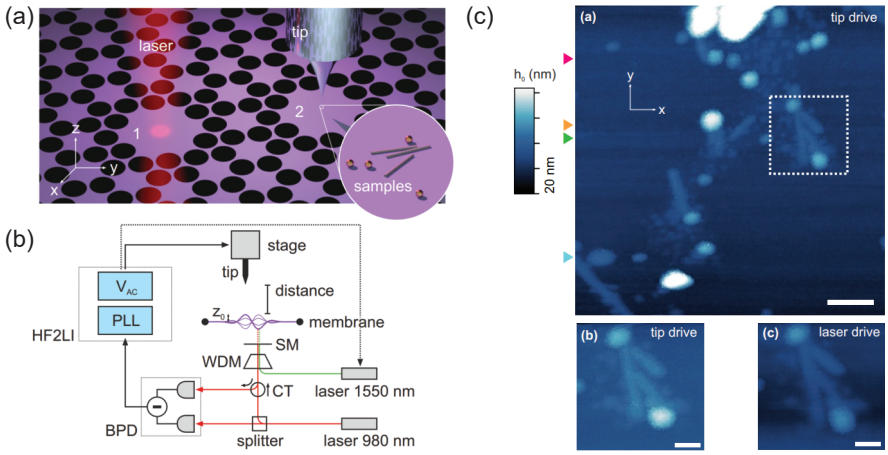

Figure 6.10: Topographic imaging through membrane based force microscopy. (a) Conceptual scheme of the experimental setup. A soft-clamped phononic dimer membrane is used as a force sensor. One defect acts as a mirror of an interferometer, while on the other defect gold nanoparticles and tobacco mosaic virus (TMV) samples have been deposited. A metallic scanning tip interacts with the samples and modifies the membrane vibrations. (b) Scheme of the experimental setup. The mechanical vibration are transduced into a phase modulation of one of the arm of an interferometric system. (c) Tomographic imaging of the samples deposited on one of the two defects. The gold nanoparticles have a nominal average diameter of 50 nm, the TMV samples a diameter of 18 nm. The bottom panels show a high resolutions scan over the area highlighted by the white square in the top panel. The membrane vibrations have been driven through electrostatic force or radiation pressure. The excitation used is listed on the top right of each panel. Figure reproduced from Ref. [H+21b].

Interestingly, one of the limiting factor for the sensitivity of the proposed parametric protocol is represented by the cross-nonlinear damping discussed in Chapter 5. The experimental realization of this parametric protocol within an MRFM experiment will benefit by the understanding and reduction of this nonlinearity.

NONLINEAR DAMPING THROUGH IN-PLANE MODE COUPLING

In Chapter 4, we give a description of the nonlinear damping starting from geometric considerations. The model discussed in Sec. 4.2 shows a good agreement with the experimental results for a various of thicknesses and modeshapes. However, it fails to describe all the measurement performed. Comparing the model presented in Sec. 4.2 with the one proposed in Sec. 6.3, we identify a possible way to generalize the model.

We introduce the geometric nonlinearities including higher order terms in the strain tensor components, see Eq. 4.6. Such extra terms in the

strain generate a stress tensor characterized by both conservative and dissipative higher-order terms. This leads to the presence of nonlinear components in the shear forces expression, Eq. (1.10a),

$$\begin{aligned} N_{\alpha\beta}^{\mathrm{nl}} =& \frac{Eh}{2(1+\nu)}\Big[(1-\nu)(\partial_\alpha w\partial_\beta w+\partial_\alpha \dot{w}\partial_\beta w)+ \\ &+\nu\delta_{\alpha\beta}((\partial_\gamma w)^2+\partial_\gamma w\partial_\gamma \dot{w})\Big]+N_{\alpha\beta}^{\mathrm{lin}}, \end{aligned} \tag{6.33}$$

from which we obtain the Duffing and the nonlinear damping term in the equation of motion for w 8Eq. (1.8a)9. $N_{\alpha\beta}^{\mathrm{lin}}$ is the linear contribution to shear forces as is described by the following expression

$$N_{\alpha\beta}^{\mathrm{lin}} = \frac{Eh}{1-\nu^2}\varepsilon_0\delta_{\alpha\beta}. \tag{6.34}$$

Importantly, the nonlinear damping modeling discussed in this thesis has been realized neglecting the contribution of the in-plane displacement components v_x and v_y.

Then in Sec. 6.3 we model the parametric drive generated on a membrane driven along the in-plane direction, including the in-plane displacement terms contribution. Here we neglect the elongation, therefore we do not have any nonlinear terms coming from the strain, but the stress definition changes due to the presence of the terms v_x and v_y, see Eq. (6.17). In this case, the shear forces components are described by

$$\begin{aligned} N_{\alpha\beta}^{\mathrm{in-plane}} =& \frac{Eh}{2(1-\nu^2)}\Big[(1-\nu)(\partial_\alpha v_\beta+\partial_\beta v_\alpha+\partial_\alpha \dot{v}_\beta+\partial_\beta \dot{v}_\beta)+ \\ &+2\nu\delta_{\alpha\beta}(\partial_\gamma v_\gamma+\partial_\gamma \dot{v}_\gamma)\Big]+N_{\alpha\beta}^{\mathrm{lin}}. \end{aligned} \tag{6.35}$$

Due to the presence of the in-plane displacement terms, the equations of motion of the overall displacement fields is constituted by 3 equations, one for each direction, described in Eqs. (6.20). We immediately notice that using Eq. (6.35) to express the shear forces introduces coupling terms $\partial_\alpha w v_x$ and $\partial_\alpha w v_y$ in the Eq. (6.20a), while Eq. (6.20b) and Eq. (6.20c) depends only on the in-plane displacement components. Before moving forward, we want to point out that in both the discussions the expression for the bending moment remains unchanged.

Piecing together the two descriptions, we could build a general model including the contribution of both the in-plane displacement components and the higher order terms in the strain. The resulting shear forces component is described as:

$$N_{\alpha\beta}^{\mathrm{full}} = N_{\alpha\beta}^{\mathrm{nl}} + N_{\alpha\beta}^{\mathrm{in-plane}} + N_{\alpha\beta}^{\mathrm{lin}}. \tag{6.36}$$

If we substitute Eq. (6.36) in Eq. (6.20), we recognize that Eq. (6.20a) contains both the standard geometric nonlinear terms and the coupling. Moreover we notice that also Eq. (6.20b) and Eq. (6.20c) include higher

order term in w. The solution of the new set of equations is not trivial and we have not investigated it yet. However we deduce that the coupling terms in the two equations describing the dynamics of the in-plane motion might lead to an energy transfer from out-of-plane to in-plane modes, similarly to the energy transfer from in-plane to out-of-plane enabling the parametric drive in Sec. 6.3. Due to the nonlinear nature of these new coupling terms, we believe that such energy transfer introduces an additional nonlinear damping source.

Merging the two models could lead to a broader description of the mechanism behind the nonlinear damping in dissipation-dilution nanomechanical resonators introducing an additional intermodal coupling contribution with a geometric origin.

MECHANICAL QUANTUM SQUEEZED STATES THROUGH PARAMETRIC AMPLIFICATION

Nanomechanical resonators in the quantum regime experienced a growing interest in the last years [AKM14]. The great amount of efforts in this field led to the preparation of mechanical states close to or at the ground state in both room temperature [GNG19; Del+20; Whi+21] and cryogenic environment [O'C+10; Cha+11; Teu+11; Wil+15; Ros+18; Sei+21; Bru+21] on various nanomechanical systems. Preparing the quantum ground state is the basis for more advanced protocols to manipulate the quantum state of mechanical modes. An example of particular interest is the preparation of mechanical mode in a quantum squeezed state [Wol+15; Pir+15], that is, a state with a quadrature fluctuations below the zero-point ones, which is the basis for improving the precision of quantum measurements [Bur+19].

A common technique used to generate mechanical squeezed states, valid in both the classical and the quantum domains, is through a parametric drive [RG91; Wu+18] modulating the resonance frequency. The parametric modulation amplifies one quadrature and squeezes the other, see Eq. (6.16). In Chapter 6, we implemented such a technique in the classical domain and we realized a thermomechanical squeezed state for our membrane mode. In Fig. 6.11, we show the typical phase space distribution for a bandgap mode characterized by linewidth of $\approx 40\,\mathrm{Hz}$. Exploiting this technique on a mechanical resonator close to its ground state is capable of generating a mechanical quantum squeezed state. Despite its simplicity, to our knowledge a quantum squeezing of mechanical motion via direct parametric driving has not been reported to date.

Parametric driving can only reduce one quadrature variance by a factor of 2, that is it can generate at most a squeezing of 3 dB. This implies that to squeeze the variance of one quadrature below the zero point motion we need to initially prepare the mechanical mode in a thermal state with an average phonon occupancy $\bar{n} < 0.5$. This is within

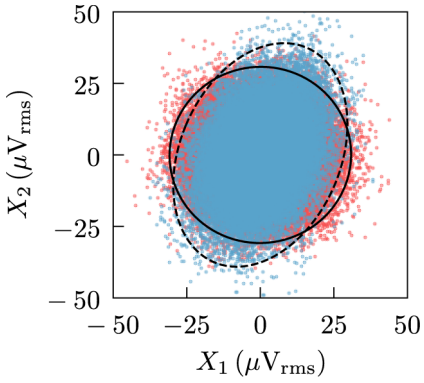

Figure 6.11: Thermomechanical squeezed state of a Dahlia generation 2 membrane at room temperature. The mechanical linewidth of this particular sample is ≈ 40 Hz. The red points represent the thermal state in absence of parametric driving, for comparison. The black solid (dashed) line is three times the covariance ellipse of the red (blue) points. From the ellipses's axes, we estimate a squeezing of ≈ 0.36 dB and an amplification of ≈ 2 dB.

reach of our soft-clamped membrane resonators with feedback cooling, as demonstrated by M. Rossi et al. [Ros+18]. Feedback cooling reduces the effective temperature of the addressed mechanical mode by adding damping, which results in broadening of the mechanical linewidth. In ref. [Ros+18] a Dahlia generation 2 membrane, at cryogenic temperature (4 K) and in an unresolved-sideband optical cavity, was prepared in a state with a phonon occupancy $\bar{n} \approx 0.29$ applying both sideband and feedback cooling simultaneously, corresponding to an effective mechanical linewidth of ≈ 2 kHz.

To reach the 3 dB limit, we need to modulate the elastic constant near the parametric threshold k_{th} defined in Sec. 6.1. This condition coincides to apply a modulation to the mechanical frequency comparable to the mechanical linewidth Γ_i. It means that the frequency modulation required will be 50 times larger than the one required in Fig. 6.11 with the additional complication of the reduced range of piezo actuator operated at cryogenic temperature.

One promising outcome of the model discussed in Chapter 6 (and still under test) is the possibility of increasing the strength of the parametric drive simply by acting on the resonance condition between out-of-plane and in-plane motion. Moreover, implementing a measurement protocol able to detect in-plane modes and engineering them could lead to the realization of a new generation of devices where the mode superposition between in-plane and out-of-plane mode is optimized to reach a stronger parametric modulation. Investigating the parametric resonant-enhancement presented in this thesis, and eventually combining it with feedback controls to go beyond the 3 dB limits [Szo+13; Szo+14; PFT15], are the next steps towards the generation of a mechanical squeezed state through parametric driving.

Looking further, a parametric driving protocol can also be applied to a non-degenerate pair of mechanical modes. In this configuration, large enough modulation strengths and initially cooled modes close to their ground states could lead to the preparation of a two-mode squeezed state, the prototypical example of entanglement between two distinct systems.

Part III

APPENDIX

A

COMPLETE SET OF MEASURED NONLINEAR LOSS ANGLES

Here we report all the measured quality factors against the measured nonlinear loss angles for all the modes and all the thicknesses studied in Chapter 4, Fig. A.1. Each point represents the measured values for a single membrane and it is the average over 5 measurements. The red points represents the two membrane where we measured negative Duffing nonlinearities. The nonlinear loss angle has been evaluated using the absolute values of the measured Duffing.

We recognize that for the low-order bandgap modes the majority of the points fall close to the cross section between the linear loss angle and the dissipation dilution or in the region that we can justified with some type of damage on the samples. Instead, the high-order bandgap modes consistently present points in the *forbidden region*. The quality factor is consistent with the simulated one. However they are characterized by a higher nonlinear losses due to the excess nonlinear damping term we discussed in Sec. 4.4

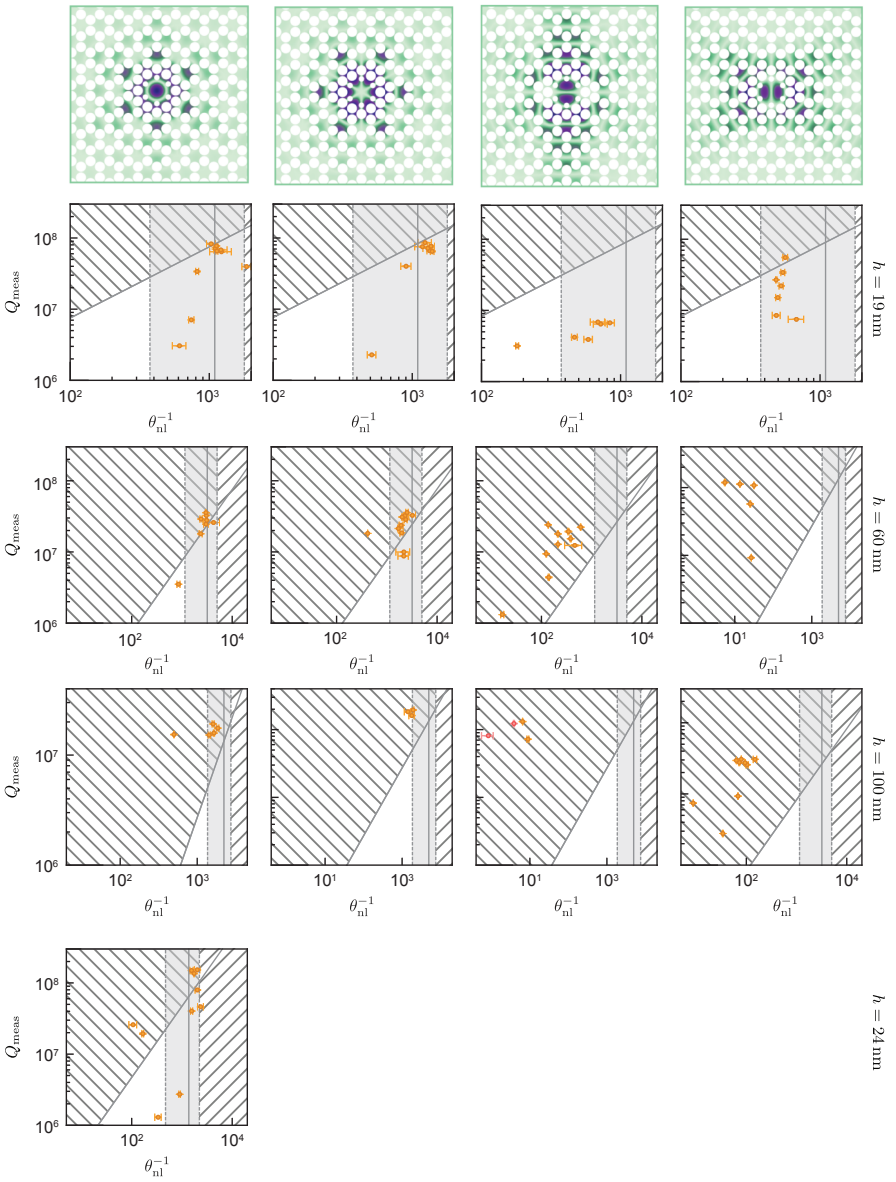

Figure A.1: Complete set of nonlinear loss angles. In the top rows we show all the modeshapes considered. Each panel shows all the measured values associated with the mode plotted above the column. The thickness is listed at the right of the rows.

B

SOFT-CLAMPED PHONONIC DIMERS: COMPLETE SET OF GEOMETRIES

In the study of the soft-clamped phononic dimers we analyze the linear and nonlinear properties of 11 different dimer geometries. They are characterized by varying dimer separation d_{sep} and relative orientation θ. We fabricate the device in such a way between all sides of the defects and the frame we always have at least 9 unit cells, distance that usually guarantees a good isolation from the environment. Since the dimer separation changes between different samples, also the outer membrane dimension changes from membrane to membrane. We show all the geometries studied listed with the outer dimension in Fig. B.1

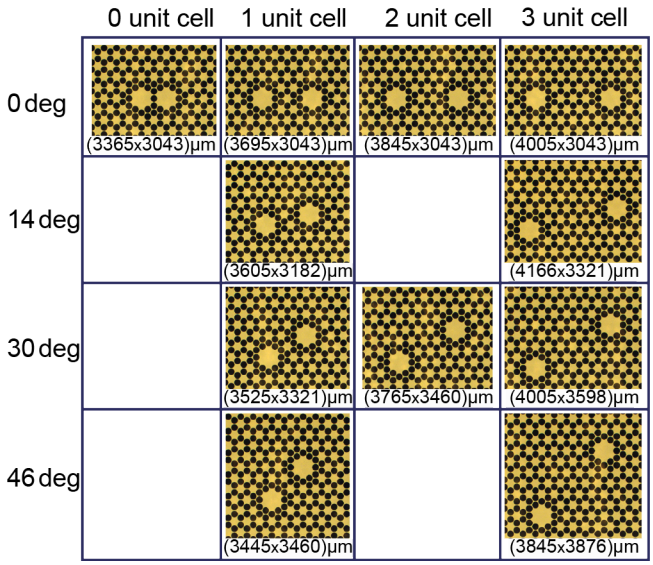

Figure B.1: Micrographs of all the device geometries studied in Chapter 5. Below each geometry we report the outer dimensions.

C

WIDE FREQUENCY TUNING

From the discussion in Sec. 6.4, we believe that the limiting factor to observe a resonantly-enhanced parametric effect is a limited control on the frequency detuning of the out-of-plane mode frequency. In this appendix we show the preliminary attempts to increase the frequency tuning through temperature control.

In the approach we are currently using, we glue the membrane frame on a ring-piezo and we tune the resonance frequency applying a DC voltage to it. The static voltage results in a piezo radial expansion (contraction) which increases (decreses) the tensile stress σ_0. The relation between tensile stress and angular frequency squared is shown in Eq. (1.24). The amount of frequency shift we can generate varies from sample to sample due to a lack of control on the gluing process. We observed a frequency shift per volt ranging from 50 Hz/V to 500 Hz/V.

To increase the resonance frequency tuning, we need an alternative way to modify the resonance frequency. To do that, we want to use the temperature dependence of the resonance frequency [Sad+20] that we observe in our modes as unwanted frequency drifts (see sec. 3.6). In the next generation of parametric measurement we are going to implement a thermal control of the resonance frequency. We realized a membrane sample holder which hosts a ring heater placed on top of a copper clamp. A sketch of the membrane assembly is reported in Fig. C.1 (a).

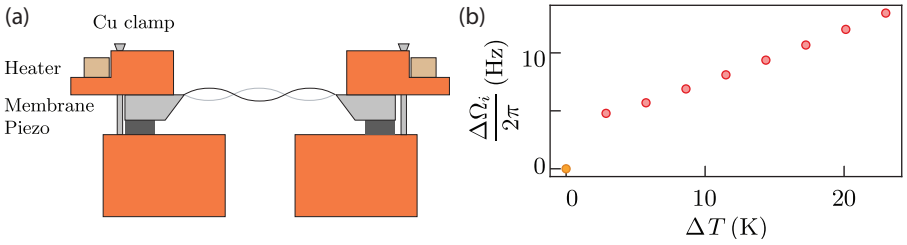

Figure C.1: Temperature frequency tuning. (a) Sketch of the sample holder cross section. The temperature variation is measured through a thermistor placed on the copper clamp. (b) Measured frequency shift against temperature variation. The yellow point corresponds to a room temperature measurement.

From the a set of preliminary measurements we observe that a temperature variation of approximately 22 K introduced a frequency shift of about 10 kHz (see Fig. C.1 (b)). The preliminary measurements suggest that the gluing is not affected by the added heat.

BIBLIOGRAPHY

Abbott, B. P. et al. (2009). "LIGO: the Laser Interferometer Gravitational-Wave Observatory." In: *Reports on Progress in Physics* 72.7, p. 076901. DOI: 10.1088/0034-4885/72/7/076901. URL: https://doi.org/10.1088/0034-4885/72/7/076901.

Aldridge, J. S. and A. N. Cleland (2005). "Noise-Enabled Precision Measurements of a Duffing Nanomechanical Resonator." In: *Physical Review Letters* 94.15. DOI: 10.1103/PhysRevLett.94.156403.

Amabili, M. (2018). "Nonlinear damping in nonlinear vibrations of rectangular plates: Derivation from viscoelasticity and experimental validation." In: *Journal of the Mechanics and Physics of Solids* 118, pp. 275–292. DOI: 10.1016/j.jmps.2018.06.004.

Antoni, T., K. Makles, R. Braive, T. Briant, P.-F. Cohadon, I. Sagnes, I. Robert-Philip, and A. Heidmann (2012). "Nonlinear mechanics with suspended nanomembranes." In: *EPL (Europhysics Letters)* 100.6, p. 68005. DOI: 10.1209/0295-5075/100/68005.

Arfken, G. B. (1985). *Mathematical method for physicists*. Academic Press City: Orlando.

Aspelmeyer, M., T. J. Kippenberg, and F. Marquardt (2014). "Cavity optomechanics." In: *Rev. Mod. Phys.* 86.4, pp. 1391–1452. DOI: 10.1103/RevModPhys.86.1391.

Atalaya, J., A. Isacsson, and J. M. Kinaret (2008). "Continuum Elastic Modeling of Graphene Resonators." In: *Nano Letters* 8.12, pp. 4196–4200. DOI: 10.1021/nl801733d.

Atalaya, J., T. W. Kenny, M. L. Roukes, and M. I. Dykman (2016). "Nonlinear damping and dephasing in nanomechanical systems." In: *Physical Review B* 94.19. DOI: 10.1103/PhysRevB.94.195440.

Bahreyni, B. (2008). *Fabrication & Design of Resonant Microdevices*. William Andrew.

Barg, A. (2014). "Optical characterization of micromechanical membranes." MA thesis. University of Copenhagen.

Barg, A., Y. Tsaturyan, E. Belhage, W. H. P. Nielsen, C. B. Møller, and A. Schliesser (2016). "Measuring and imaging nanomechanical motion with laser light." In: *Applied Physics B* 123.1. DOI: 10.1007/s00340-016-6585-7.

Beccari, A., M. J. Bereyhi, R Groth, S. A. Fedorov, A. Arabmoheghi, N. J. Engelsen, and T. J. Kippenberg (2021a). "Hierarchical tensile structures with ultralow mechanical dissipation." In: *arXiv:2103.09785* arXiv:2103.09785.

Beccari, A., D. A. Visani, S. A. Fedorov, M. J. Bereyhi, V. Boureau, N. J. Engelsen, and T. J. Kippenberg (2021b). "Strained crystalline nanomechanical resonators with ultralow dissipation." In: *arXiv:2103.09785*.

Bereyhi, M. J., A. Arabmoheghi, S. A. Fedorov, A. Beccari, G. Huang, T. J. Kippenberg, and N. J. Engelsen (2021). "Nanomechanical resonators with ultra-high-Q perimeter modes." In: *arXiv:2108.03615* arXiv:2108.03615.

Bianco, S. et al. (2006). "Silicon resonant microcantilevers for absolute pressure measurement." In: *Journal of Vacuum Science & Technology B: Microelectronics and Nanometer Structures* 24.4, p. 1803. DOI: 10.1116/1.2214698.

Brubaker, B. M., J. M. Kindem, M. D. Urmey, S. Mittal, R. D. Delaney, P. S. Burns, M. R. Vissers, K. W. Lehnert, and C. A. Regal (2021). "Optomechanical ground-state cooling in a continuous and efficient electro-optic transducer." In: *arXiv:2112.13429*.

Burd, S. C., R. Srinivas, J. J. Bollinger, A. C. Wilson, D. J. Wineland, D. Leibfried, D. H. Slichter, and D. T. C. Allcock (2019). "Quantum amplification of mechanical oscillator motion." In: *Science* 364.6446, pp. 1163–1165. DOI: 10.1126/science.aaw2884.

Cagnoli, G., J. Hough, D. DeBra, M. Fejer, E. Gustafson, S. Rowan, and V. Mitrofanov (2000). "Damping dilution factor for a pendulum in an interferometric gravitational waves detector." In: *Phys. Lett. A* 272.1-2, pp. 39–45. DOI: 10.1016/S0375-9601(00)00411-4.

Catalini, L., M. Rossi, E. C. Langman, and A. Schliesser (2021). "Modeling and Observation of Nonlinear Damping in Dissipation-Diluted Nanomechanical Resonators." In: *Physical Review Letters* 126.17. DOI: 10.1103/PhysRevLett.126.174101.

Catalini, L., Y. Tsaturyan, and A. Schliesser (2020). "Soft-Clamped Phononic Dimers for Mechanical Sensing and Transduction." In: *Phys. Rev. Appl* 14.1. DOI: 10.1103/PhysRevApplied.14.014041.

Chan, J., T. P. M. Alegre, A. H. Safavi-Naeini, J. T. Hill, A. Krause, S. Gr´oblacher, M. Aspelmeyer, and O. Painter (2011). "Laser cooling of a nanomechanical oscillator into its quantum ground state." In: *Nature* 478.7367, pp. 89–92. DOI: 10.1038/nature10461.

Chaste, J., A. Eichler, J. Moser, G. Ceballos, R. Rurali, and A. Bachtold (2012). "A nanomechanical mass sensor with yoctogram resolution." In: *Nature Nanotechnology* 7.5, pp. 301–304. DOI: 10.1038/nnano.2012.42.

Chen, J., M. Rossi, D. Mason, and A. Schliesser (2020). "Entanglement of propagating optical modes via a mechanical interface." In: *Nature Communications* 11.1. DOI: 10.1038/s41467-020-14768-1.

Cleland, A. N. (2003). *Foundations of Nanomechanics: From Solid-State Theory to Device Applications*. Springer-Verlag Berlin Heidelberg.

Corsi, C., I. Liontos, S. Cavalieri, M. Bellini, G. Venturi, and R. Eramo (2015). "An ultrastable Michelson interferometer for high-resolution spectroscopy in the XUV." In: *Optics Express* 23.4, p. 4106. DOI: 10.1364/OE.23.004106.

Cuairan, M. T, J. Gieseler, N. Meyer, and R. Quidant (2021). "Precision calibration of the Duffing oscillator with phase control." In: *arXiv:2108.12234*.

Davidovikj, D., F. Alijani, S. J. Cartamil-Bueno, H. S. J. van der Zant, M. Amabili, and P. G. Steeneken (2017). "Nonlinear dynamic characterization of two-dimensional materials." In: *Nature Communications* 8.1. DOI: 10.1038/s41467-017-01351-4.

Defoort, M., K. J. Lulla, C. Blanc, H. Ftouni, O. Bourgeois, and E. Collin (2012). "Stressed Silicon Nitride Nanomechanical Resonators at Helium Temperatures." In: *Journal of Low Temperature Physics* 171.5-6, pp. 731–736. DOI: 10.1007/s10909-012-0693-5.

Degen, C. L., M. Poggio, H. J. Mamin, C. T. Rettner, and D. Rugar (2009). "Nanoscale magnetic resonance imaging." In: *Proceedings of the National Academy of Sciences* 106.5, pp. 1313–1317. DOI: 10.1073/pnas.0812068106.

Delaney, R., A. Reed, R. Andrews, and K. Lehnert (2019). "Measurement of Motion beyond the Quantum Limit by Transient Amplification." In: *Physical Review Letters* 123.18. DOI: 10.1103/PhysRevLett.123.183603.

Delić, U., M. Reisenbauer, K. Dare, D. Grass, V. Vuletić, N. Kiesel, and M. Aspelmeyer (2020). "Cooling of a levitated nanoparticle to the motional quantum ground state." In: *Science* 367.6480, pp. 892–895. DOI: 10.1126/science.aba3993.

Duwel, A., R. N. Candler, T. W. Kenny, and M. Varghese (2006). "Engineering MEMS Resonators With Low Thermoelastic Damping." In: *Journal of Microelectromechanical Systems* 15.6, pp. 1437–1445. DOI: 10.1109/JMEMS.2006.883573.

Eichler, A., J. Moser, J. Chaste, M. Zdrojek, I. Wilson-Rae, and A. Bachtold (2011). "Nonlinear damping in mechanical resonators made from carbon nanotubes and graphene." In: *Nature Nanotechnology* 6.6, pp. 339–342. DOI: 10.1038/nnano.2011.71.

Faust, T., J. Rieger, M. J. Seitner, J. P. Kotthaus, and E. M. Weig (2014). "Signatures of two-level defects in the temperature-dependent damping of nanomechanical silicon nitride resonators." In: *Physical Review B* 89.10. DOI: 10.1103/PhysRevB.89.100102.

Fedorov, S. A., N. J. Engelsen, A. H. Ghadimi, M. J. Bereyhi, R. Schilling, D. J. Wilson, and T. J. Kippenberg (2019). "Generalized dissipation dilution in strained mechanical resonators." In: *Physical Review B* 99.5. DOI: 10.1103/PhysRevB.99.054107.

Fendley, J. J. (1982). "Measurement of refractive index using a Michelson interferometer." In: *Physics Education* 17.5, pp. 209–211. DOI: 10.1088/0031-9120/17/5/001.

Fischer, R., N. S. Kampel, G. G. T. Assumpcao, P. Yu, K. Cicak, R. W. Peterson, R. W. Simmonds, and C. A. Regal (2016). "Optical probing of mechanical loss of a Si3N membrane below 100 mK." In: *arXiv:1611.00878*.

Fong, K. Y., W. H. P. Pernice, and H. X. Tang (2012). "Frequency and phase noise of ultrahighQsilicon nitride nanomechanical resonators." In: *Physical Review B* 85.16. DOI: 10.1103/PhysRevB.85.161410.

Fowles, G. R. (1989). *Introduction to Modern Optics*. Dover Publications, Inc., New York.

Fox, M. (2006). *Quantum optics: an introduction*. Oxford University Press, USA.

Ghadimi, A. H., S. A. Fedorov, N. J. Engelsen, M. J. Bereyhi, R. Schilling, D. J. Wilson, and T. J. Kippenberg (2018). "Elastic strain engineering for ultralow mechanical dissipation." In: *Science* 360.6390, pp. 764–768. DOI: 10.1126/science.aar6939.

González, G. (2000). "Suspensions thermal noise in the LIGO gravitational wave detector." In: *Classical and Quanrum Gravity* 17.21, pp. 4409–4435. DOI: 10.1088/0264-9381/17/21/305.

Guo, J., R. Norte, and S. Gr´oblacher (2019). "Feedback Cooling of a Room Temperature Mechanical Oscillator close to its Motional Ground State." In: *Physical Review Letters* 123.22. DOI: 10.1103/PhysRevLett.123.223602.

Gusso, A. (2020). "Nonlinear damping in suspended beam micro- and nanoresonators due to surface loss." In: *Journal of Sound and Vibration* 467, p. 115067. DOI: 10.1016/j.jsv.2019.115067.

HF2 User Manual - LabOne Edition (n.d.).

Hälg, D., T. Gisler, E. C. Langman, S. Misra, O. Zilberberg, A. Schliesser, C. L. Degen, and A. Eichler (2021a). "Strong parametric coupling between two ultra-coherent membrane modes." In: *arXiv:2109.11943*.

Hälg, D. et al. (2021b). "Membrane-Based Scanning Force Microscopy." In: *Physical Review Applied* 15.2. DOI: 10.1103/PhysRevApplied.15.L021001.

Héritier, M., A. Eichler, Y. Pan, U. Grob, I. Shorubalko, M. D. Krass, Y. Tao, and C. L. Degen (2018). "Nanoladder Cantilevers Made from Diamond and Silicon." In: *Nano Letters* 18.3, pp. 1814–1818. DOI: 10.1021/acs.nanolett.7b05035.

Hocke, F., M. Pernpeintner, X. Zhou, A. Schliesser, T. J. Kippenberg, H. Huebl, and R. Gross (2014). "Determination of effective mechanical properties of a double-layer beam by means of a nano-electromechanical transducer." In: *Applied Physics Letters* 105.13, p. 133102. DOI: 10.1063/1.4896785.

Huang, Y. L. and P. R. Saulson (1998). "Dissipation mechanisms in pendulums and their implications for gravitational wave interferometers." In: *Review of Scientific Instruments* 69.2, pp. 544–553. DOI: 10.1063/1.1148692.

Imboden, M., O. A. Williams, and P. Mohanty (2013). "Observation of Nonlinear Dissipation in Piezoresistive Diamond Nanomechanical Resonators by Heterodyne Down-Mixing." In: *Nano Letters* 13.9, pp. 4014–4019. DOI: 10.1021/nl401978p.

Iso, S., H. Ohta, and T. Suyama (2018). "Secular terms in Dyson series to all orders of perturbation." In: *Progress of Theoretical and Experimental Physics* 2018.8. DOI: 10.1093/ptep/pty079.

Judge, J. A., D. M. Photiadis, J. F. Vignola, B. H. Houston, and J. Jarzynski (2007). "Attachment loss of micromechanical and nanomechanical resonators in the limits of thick and thin support structures." In: *Journ. Appl. Phys.* 101.1, p. 013521. DOI: 10.1063/1.2401271.

Karabalin, R. B., M. C. Cross, and M. L. Roukes (2009). "Nonlinear dynamics and chaos in two coupled nanomechanical resonators." In: *Physical Review B* 79.16. DOI: 10.1103/PhysRevB.79.165309.

Karg, T. M., B. Gouraud, C. T. Ngai, G.-L. Schmid, K. Hammerer, and P. Treutlein (2020). "Light-mediated strong coupling between a mechanical oscillator and atomic spins 1 meter apart." In: *Science* 369.6500, pp. 174–179. DOI: 10.1126/science.abb0328.

Kiselev, A. A. and G. J. Iafrate (2008). "Phonon dynamics and phonon assisted losses in Euler-Bernoulli nanobeams." In: *Phys. Rev. B* 77.20. DOI: 10.1103/PhysRevB.77.205436.

Kittel, C. and H. Kroemer (1980). *Thermal physics*. W. H. Freeman.

Košata, J., O. Zilberberg, C. L. Degen, R. Chitra, and A. Eichler (2020). "Spin Detection via Parametric Frequency Conversion in a Membrane Resonator." In: *Physical Review Applied* 14.1. DOI: 10.1103/PhysRevApplied.14.014042.

Kubo, R (1966). "The fluctuation-dissipation theorem." In: *Reports on Progress in Physics* 29.1, pp. 255–284. DOI: 10.1088/0034-4885/29/1/306.

Landau, L. D. and E. M. Lifshitz (1970). *Theory of elasticity*. Pergamon Press.

Lautrup, B. (2011). *Physics of Continuous Matter*. CRC Press.

Lin, J.-T., B. Lee, and B. Alphenaar (2010). "The magnetic coupling of a piezoelectric cantilever for enhanced energy harvesting efficiency." In: *Smart Materials and Structures* 19.4, p. 045012. DOI: 10.1088/0964-1726/19/4/045012.

MIlonni, P. W. and J. H. Eberly (2010). *Laser physiscs*. John Wiley & Sons, Inc.

Mahboob, I., H. Okamoto, K. Onomitsu, and H. Yamaguchi (2014). "Two-Mode Thermal-Noise Squeezing in an Electromechanical Resonator." In: *Physical Review Letters* 113.16. DOI: 10.1103/PhysRevLett.113.167203.

Mamin, H. J. and D. Rugar (2001). "Sub-attonewton force detection at millikelvin temperatures." In: *Applied Physics Letters* 79.20, pp. 3358–3360. DOI: 10.1063/1.1418256.

Mason, D., J. Chen, M. Rossi, Y. Tsaturyan, and A. Schliesser (2019). "Continuous force and displacement measurement below the standard quantum limit." In: *Nature Physics* 15.8, pp. 745–749. DOI: 10.1038/s41567-019-0533-5.

Midolo, L., A. Schliesser, and A. Fiore (2018). "Nano-opto-electro-mechanical systems." In: *Nature Nanotechnology* 13.1, pp. 11–18. DOI: 10.1038/s41565-017-0039-1.

Midtvedt, D., A. Isacsson, and A. Croy (2014). "Nonlinear phononics using atomically thin membranes." In: *Nature Communications* 5.1. DOI: 10.1038/ncomms5838.

Nayfeh, A. H. (1993). *Introduction to Perturbation Techniques*. Wiley-VCH.

Nayfeh, A. H. and D. T. Mook (1995). *Nonlinear oscillations*. Wiley-VCH.

Neuhaus, L., R. Metzdorff, S. Chua, T. Jacqmin, T. Briant, A. Heidmann, P.-F. Cohadon, and S. Deleglise (2017). "PyRPL (Python Red Pitaya Lockbox) — An open-source software package for FPGA-controlled quantum optics experiments." In: DOI: 10.1109/CLEOE-EQEC.2017.8087380.

O'Connell, A. D. et al. (2010). "Quantum ground state and single-phonon control of a mechanical resonator." In: *Nature* 464.7289, pp. 697–703. DOI: 10.1038/nature08967.

Page, M. et al. (2021). "Gravitational wave detectors with broadband high frequency sensitivity - data." In: *Communications Physics*. DOI: 10.6084/m9.figshare.13352669.

Patil, Y., S. Chakram, L. Chang, and M. Vengalattore (2015). "Thermomechanical Two-Mode Squeezing in an Ultrahigh-QMembrane Resonator." In: *Physical Review Letters* 115.1. DOI: 10.1103/PhysRevLett.115.017202.

Pham-Gia, T. and T. Hung (2001). "The mean and median absolute deviations." In: *Mathematical and Computer Modelling* 34.7-8, pp. 921–936. DOI: 10.1016/S0895-7177(01)00109-1.

Pickering, C., N. Halliwell, and T. Wilmshurst (1986). "The laser vibrometer: A portable instrument." In: *Journal of Sound and Vibration* 107.3, pp. 471–485. DOI: 10.1016/S0022-460X(86)80119-5.

Piller, M., J. Hiesberger, E. Wistrela, P. Martini, N. Luhmann, and S. Schmid (2021). "Thermal IR detection with nanoelectromechanical silicon nitride trampoline resonators." In: *arXiv:2105.03999*.

Pirkkalainen, J.-M., E. Damsk´agg, M. Brandt, F. Massel, and M. Sillanp´a´a (2015). "Squeezing of Quantum Noise of Motion in a Micromechanical Resonator." In: *Physical Review Letters* 115.24. DOI: 10.1103/PhysRevLett.115.243601.

Poggio, M., C. L. Degen, H. J. Mamin, and D. Rugar (2007). "Feedback Cooling of a Cantilever's Fundamental Mode below 5 mK." In: *Physical Review Letters* 99.1. DOI: 10.1103/PhysRevLett.99.017201.

Polunin, P. M., Y. Yang, M. I. Dykman, T. W. Kenny, and S. W. Shaw (2016). "Characterization of MEMS Resonator Nonlinearities Using the Ringdown Response." In: *Journal of Microelectromechanical Systems* 25.2, pp. 297–303. DOI: 10.1109/JMEMS.2016.2529296.

Poot, M, K. Y. Fong, and H. X. Tang (2015). "Deep feedback-stabilized parametric squeezing in an opto-electromechanical system." In: *New Journal of Physics* 17.4, p. 043056. DOI: 10.1088/1367-2630/17/4/043056.

Proakis, J. G. and D. Manolakis (2006). *Digital Signal Processing*. Prentice Hall.

Reetz, C., R. Fischer, G. Assumpção, D. McNally, P. Burns, J. Sankey, and C. Regal (2019). "Analysis of Membrane Phononic Crystals with Wide Band Gaps and Low-Mass Defects." In: *Physical Review Applied* 12.4. DOI: 10.1103/PhysRevApplied.12.044027.

Reinhardt, C., T. M'uller, A. Bourassa, and J. C. Sankey (2016). "Ultralow-Noise SiN Trampoline Resonators for Sensing and Optomechanics." In: *Physical Review X* 6.2. DOI: 10.1103/PhysRevX.6.021001.

Remus, L. G., M. P. Blencowe, and Y. Tanaka (2009). "Damping and decoherence of a nanomechanical resonator due to a few two-level systems." In: *Phys. Rev. B* 80.17. DOI: 10.1103/PhysRevB.80.174103.

Rosiek, C. A. (2019). "Enhancing the Formation of Wigner Negativity in a Kerr Oscillator via Quadrature Squeezing." MA thesis. University of Copenhagen.

Rossi, M. (2020). "Qunatum measurement and control of a mechanical resonator." PhD thesis. University of Copenhagen.

Rossi, M., D. Mason, J. Chen, and A. Schliesser (2019). "Observing and Verifying the Quantum Trajectory of a Mechanical Resonator." In: *Physical Review Letters* 123.16. DOI: 10.1103/PhysRevLett.123.163601.

Rossi, M., D. Mason, J. Chen, Y. Tsaturyan, and A. Schliesser (2018). "Measurement-based quantum control of mechanical motion." In: *Nature* 563.7729, pp. 53–58. DOI: 10.1038/s41586-018-0643-8.

Rugar, D. and P. Gr'utter (1991). "Mechanical parametric amplification and thermomechanical noise squeezing." In: *Physical Review Letters* 67.6, pp. 699–702. DOI: 10.1103/PhysRevLett.67.699.

Sadeghi, P., M. Tanzer, N. Luhmann, M. Piller, M.-H. Chien, and S. Schmid (2020). "Thermal Transport and Frequency Response of Localized Modes on Low-Stress Nanomechanical Silicon Nitride Drums Featuring a Phononic-Band-Gap Structure." In: *Physical Review Applied* 14.2. DOI: 10.1103/PhysRevApplied.14.024068.

Sahu, R., W. Hease, A. Rueda, G. Arnold, L. Qiu, and J. Fink (2021). "Quantum-enabled interface between microwave and telecom light." In: *arXiv:2107.08303*.

Schliesser, A. (2009). "Cavity Optomechanics and Optical Frequency Comb Generation with Silica Whispering-Gallery-Mode Microresonators." PhD thesis. University of Munich.

Schmid, S., K. D. Jensen, K. H. Nielsen, and A. Boisen (2011). "Damping mechanisms in high-Qmicro and nanomechanical string resonators." In: *Phys. Rev. B* 84.16. DOI: 10.1103/PhysRevB.84.165307.

Schmid, S., L. G. Villanueva, and M. L. Roukes (2016). *Fundamentals of Nanomechanical Resonators*. Springer International Publishing. DOI: 10.1007/978-3-319-28691-4.

Seis, Y. (2021). "Ultra-Coherent Electro-Mechanics in the Quantum Regime." PhD thesis. University of Copenhagen.

Seis, Y., T. Capelle, E. Langman, S. Saarinen, E. Planz, and A. Schliesser (2021). "Ground State Cooling of an Ultracoherent Electromechanical System." In: *arXiv:2107.05552*.

Szorkovszky, A., G. A. Brawley, A. C. Doherty, and W. P. Bowen (2013). "Strong Thermomechanical Squeezing via Weak Measurement." In: *Physical Review Letters* 110.18. DOI: 10.1103/PhysRevLett.110.184301.

Szorkovszky, A, A. A. Clerk, A. C. Doherty, and W. P. Bowen (2014). "Detuned mechanical parametric amplification as a quantum non-demolition measurement." In: *New Journal of Physics* 16.4, p. 043023. DOI: 10.1088/1367-2630/16/4/043023.

Tao, Y., J. M. Boss, B. A. Moores, and C. L. Degen (2014). "Single-crystal diamond nanomechanical resonators with quality factors exceeding one million." In: *Nature Communications* 5.1. DOI: 10.1038/ncomms4638.

Teufel, J. D., T. Donner, D. Li, J. W. Harlow, M. S. Allman, K. Cicak, A. J. Sirois, J. D. Whittaker, K. W. Lehnert, and R. W. Simmonds (2011). "Sideband cooling of micromechanical motion to the quantum ground state." In: *Nature* 475.7356, pp. 359–363. DOI: 10.1038/nature10261.

Thomas, R. A., M. Parniak, C. Østfeldt, C. B. Møller, C.Bærentsen, Y. Tsaturyan, A. Schliesser, J. Appel, E. Zeuthen, and E. S. Polzik (2020). "Entanglement between distant macroscopic mechanical and spin systems." In: *Nature Physics* 17.2, pp. 228–233. DOI: 10.1038/s41567-020-1031-5.

Timoshenko, S. and S. W. Krieger (1987). *Theory of plates and shells*. McGraw hill book company.

Tsaturyan, Y., A. Barg, E. S. Polzik, and A. Schliesser (2017). "Ultracoherent nanomechanical resonators via soft clamping and dissipation dilution." In: *Nature Nanotech.* 12.8, pp. 776–783. DOI: 10.1038/nnano.2017.101.

Tsaturyan, Y. (2019). "Ultracoherent soft-clamped mechanical resonators for quantum cavity optomechanics." PhD thesis. University of Copenhagen.

Unterreithmeier, Q. P., T. Faust, and J örg P. Kotthaus (2010). "Damping of Nanomechanical Resonators." In: *Phys. Rev. Lett.* 105.2. DOI: 10.1103/PhysRevLett.105.027205.

Verbridge, S. S., D. F. Shapiro, H. G. Craighead, and J. M. Parpia (2007). "Macroscopic Tuning of Nanomechanics: Substrate Bending for Reversible Control of Frequency and Quality Factor of Nanostring Resonators." In: *Nano Letters* 7.6, pp. 1728–1735. DOI: 10.1021/nl070716t.

Villanueva, L. G., R. B. Karabalin, M. H. Matheny, D. Chi, J. E. Sader, and M. L. Roukes (2013). "Nonlinearity in nanomechanical cantilevers." In: *Physical Review B* 87.2. DOI: 10.1103/PhysRevB.87.024304.

Villanueva, L. G. and S. Schmid (2014). "Evidence of Surface Loss as Ubiquitous Limiting Damping Mechanism in SiN Micro- and Nanomechanical Resonators." In: *Phys. Rev. Lett.* 113.22. DOI: 10.1103/PhysRevLett.113.227201.

Vinante, A. and P. Falferi (2013). "Feedback-Enhanced Parametric Squeezing of Mechanical Motion." In: *Physical Review Letters* 111.20. DOI: 10.1103/PhysRevLett.111.207203.

Wallucks, A., I. Marinković, B. Hensen, R. Stockill, and S. Gr´oblacher (2020). "A quantum memory at telecom wavelengths." In: *Nature Physics* 16.7, pp. 772–777. DOI: 10.1038/s41567-020-0891-z.

Wells, C. W., A. E. Potter, and T. H. Morgan (1980). "Near-Infrared Spectral Imaging Michelson Interferometer For Astronomical Applications." In: ed. by W. L. Wolfe and J. Zimmerman. DOI: 10.1117/12.958722.

Westra, H. J. R., M. Poot, H. S. J. van der Zant, and W. J. Venstra (2010). "Nonlinear Modal Interactions in Clamped-Clamped Mechanical Resonators." In: *Physical Review Letters* 105.11. DOI: 10.1103/PhysRevLett.105.117205.

Whittle, C. et al. (2021). "Approaching the motional ground state of a 10-kg object." In: *Science* 372.6548, pp. 1333–1336. DOI: 10.1126/science.abh2634.

Wilson-Rae, I., R. A. Barton, S. S. Verbridge, D. R. Southworth, B. Ilic, H. G. Craighead, and J. M. Parpia (2011). "High-QNanomechanics via Destructive Interference of Elastic Waves." In: *Physical Review Letters* 106.4. DOI: 10.1103/PhysRevLett.106.047205.

Wilson, D. J., V. Sudhir, N. Piro, R. Schilling, A. Ghadimi, and T. J. Kippenberg (2015). "Measurement-based control of a mechanical oscillator at its thermal decoherence rate." In: *Nature* 524.7565, pp. 325–329. DOI: 10.1038/nature14672.

Wollman, E. E., C. U. Lei, A. J. Weinstein, J. Suh, A. Kronwald, F. Marquardt, A. A. Clerk, and K. C. Schwab (2015). "Quantum squeezing of motion in a mechanical resonator." In: *Science* 349.6251, pp. 952–955. DOI: 10.1126/science.aac5138.

Wu, S., J. Sheng, X. Zhang, Y. Wu, and H. Wu (2018). "Parametric excitation of a SiN membrane via piezoelectricity." In: *AIP Advances* 8.1, p. 015209. DOI: 10.1063/1.5009952.

Yi, F., H. Zhu, J. C. Reed, and E. Cubukcu (2013). "Plasmonically Enhanced Thermomechanical Detection of Infrared Radiation." In: *Nano Letters* 13.4, pp. 1638–1643. DOI: 10.1021/nl400087b.

Younis, M. I. (2011). *MEMS Linear and Nonlinear Statics and Dynamics*. Springer US. DOI: 10.1007/978-1-4419-6020-7.

Yu, P.-L., T. P. Purdy, and C. A. Regal (2012). "Control of Material Damping in High-QMembrane Microresonators." In: *Physical Review Letters* 108.8. DOI: 10.1103/PhysRevLett.108.083603.

Yuan, M., M. A. Cohen, and G. A. Steele (2015). "Silicon nitride membrane resonators at millikelvin temperatures with quality factors exceeding 108." In: *Applied Physics Letters* 107.26, p. 263501. DOI: 10.1063/1.4938747.

Zaitsev, S., O. Shtempluck, E. Buks, and O. Gottlieb (2011). "Nonlinear damping in a micromechanical oscillator." In: *Nonlinear Dynamics* 67.1, pp. 859–883. DOI: 10.1007/s11071-011-0031-5.

COLOPHON

This document was typeset using the typographical look-and-feel `classicthesis` developed by André Miede and Ivo Pletikosić. The style was inspired by Robert Bringhurst's seminal book on typography "*The Elements of Typographic Style*". `classicthesis` is available for both LaTeX and LyX:

https://bitbucket.org/amiede/classicthesis/